IOT SENSORS FOR INDUSTRIAL AND AGRICULTURAL APPLICATIONS: DEVELOPMENT OF WIRELESS NETWORK AND PROCESS CONTROL

by

Xiaofan Jiang

A Dissertation

Submitted to the Faculty of Purdue University

In Partial Fulfillment of the Requirements for the degree of

Doctor of Philosophy

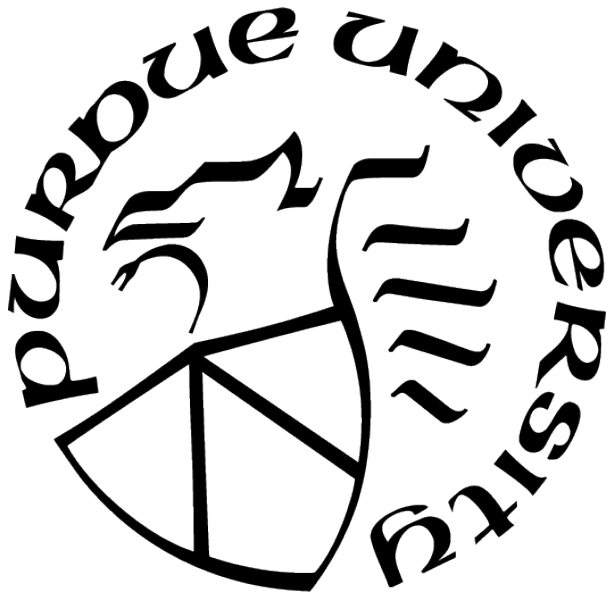

School of Electrical and Computer Engineering

West Lafayette, Indiana

December 2020

THE PURDUE UNIVERSITY GRADUATE SCHOOL
STATEMENT OF COMMITTEE APPROVAL

Dr. Dimitrios Peroulis, Chair

School of Electrical and Computer Engineering

Dr. Babak Ziaie

School of Electrical and Computer Engineering

Dr. Xiaozhu Lin

School of Electrical and Computer Engineering

Dr. Nithin Raghunathan

Birck Nanotechnology Center

Approved by:

Dr. Dimitrios Peroulis

ACKNOWLEDGMENTS

I wish to express my deepest appreciation and gratitude to my committee chair, Prof. Dimitrios Peroulis, thank you for your encouragement, wisdom, enthusiasm, and guidance over the years. To my committee members, Prof. Babak Ziaie, Prof. Xiaozhu Lin, and Dr. Nithin Raghunathan, thank you for your time, guidance, helpful thoughts, and ideas that shaped my work and helped me be a better researcher. I would like to thank Prof. Alina A. Alexeenko for her great expertise in lyophilization and delightful insights and advice during our update meetings throughout my doctoral study. I appreciate Dr. Petr Kazarin for his expertise in computational fluid dynamics and heat mass transfer modeling that helped the development of virtual thermocouple. To my family and friends, your constant support and overwhelming love helped me survive the stress and tough times, I'm truly grateful to all of you.

TABLE OF CONTENTS

LIST OF TABLES

LIST OF FIGURES

ABSTRACT

As the new paradigm of data collection enabled by the advancements in wireless technology and digital electronics, small sensing devices have started to be used in everyday life. These devices are capable of sensing, computing, communicating, and forming a wireless sensor network (WSN) which is necessary to provide sensing services and to monitor various conditions. In addition to WSNs, the idea of Internet of Things (IoT) has started to draw more attention. IoT is defined as an interconnection between identifiable devices within the internet for sensing and monitoring processes. This dissertation addresses the development of wireless network and process control for two challenging IoT applications, namely smart agriculture and industrial lyophilization.

Smart agriculture refers to the concept of using modern technology to increase the quantity and quality of agricultural products. This dissertation presents a novel hybrid large-area IoT network by combining the low-power wide-area network (LPWAN) as well as ultra-low-power wireless personal area networks (WPAN) that delivers wide-area coverage while maintaining low-power operation.

Lyophilization is the process of removing water content from a material with the objective of increasing its stability and, hence, its shelf life. Continuous inline process tracking is imperative to a successful lyophilization process in industrial pharmaceuticals. To address this need, this dissertation presents two wireless sensing systems that are capable of monitoring lyophilization process with detailed design and demonstration.

1. INTRODUCTION

1.1 Background

As the recent advancement of the Internet of Things (IoT) technology enables the possibility of data collection from diverse environments, the Fourth Industrial Revolution have given rise to IoT-enabled, mistake-proofing sensors that connect numerous devices and systems[1]. Industrial IoT sensors are widely used in different industries to monitor equipment, assets, systems, and overall performance. Real-time data is then analyzed and transmitted to a centralized system. The applications of IoT rely on the connectivity of physical smart devices, industrial devices, or other embedded devices. These devices must have some information sampling capabilities which could come from the sensors, cameras, actuators, etc. Then with the wireless communication ability, the sampled information can be collected into the data processing center for additional applications and analytics. Because of the powerful data collection and communication abilities, IoT system is a perfect match for many applications.

IoT provides the connectivity to physically distributed devices, home appliances, and even devices in more critical sectors, such as healthcare, public utilities (e.g., electric grids), environmental monitoring, and transportation. These IoT devices sense, compute, and communicate, often in resource-limited deployments, forming a Wireless Sensor Network (WSN). Low power communication technologies for wireless IoT communication can generally fall within two categories (Fig. 1.1), a more detailed discussion on the technologies can also be found in Chapter 1:

- Wireless Personal Area Networks (WPANs): typically communicate from 10 meters to a few hundred meters. This category includes Bluetooth, Bluetooth Low Energy (BLE), ANT, ZigBee, etc., which are applied directly in short-range personal area networks or if designed in a mesh topology and with higher transmit power, larger area coverage is possible.

- Low-Power Wide-Area Networks (LPWANs): have a communication range greater than one kilometer. Each gateway could communicate with thousands of end-devices.

This category includes LoRaWAN, Sigfox, NB-IoT, etc. A summary of these technologies is presented in Chapter 2 [2]–[4].

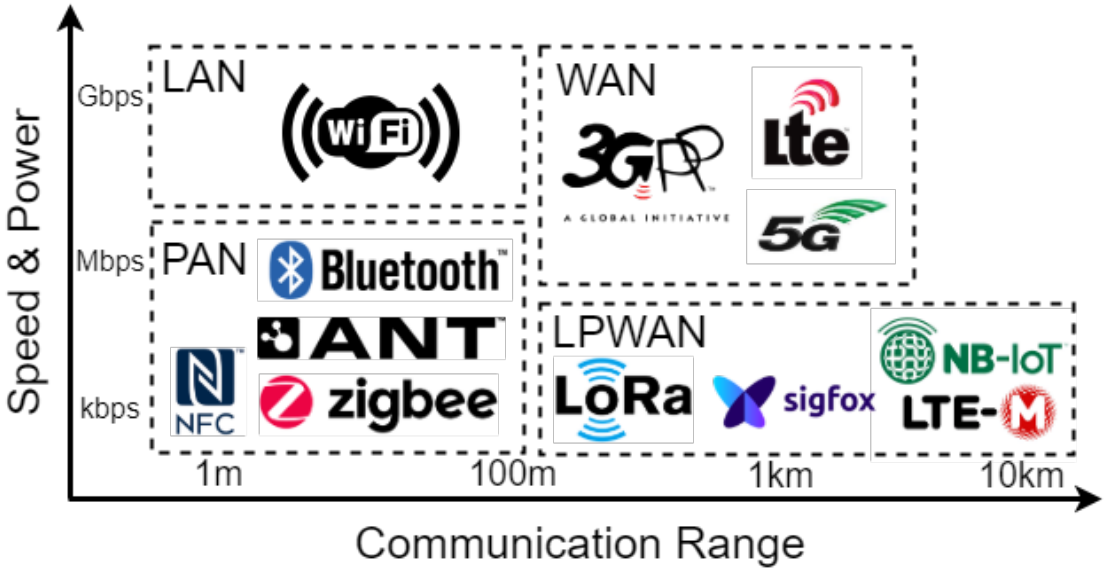

Figure 1.1. A summary of current wireless commutation technologies, where trades-off between communication range (x-axis) and power/speed (y-axis) are represented[5].

In the Industrial context, Industrial Internet of Things (IIoT) refers to interconnected sensors, instruments, and other devices networked together with computers' industrial applications, including manufacturing and energy management. In the digital agriculture context, these devices may monitor various environmental conditions, such as soil moisture, nutrient quality, or microbial activity [6]. The sensor data is collected and routed through the WSN and sent to the cloud for further analysis and possible closed-loop control. This dissertation addresses the development of IoT WSNs for two challenging areas, namely industrial lyophilization and smart agriculture. These works are based on real-world deployments and highlight the practical design challenges and insights that arise from the long-term unattended operation of those IoT systems. They highlight a distinct set of challenges in terms of wireless networking capabilities and hardware design.

Some analytics can also be run on the back-end cloud-computing resource and derive actionable knowledge from the raw data, such as, how to fertilize specific parts of the farm in a localized manner. Such kinds of decisions do not require real-time (or, near real-

time) decision making. As an example of where data must be received and analyzed in approximately real-time, consider the following scenario. When a combine is moving through the field, it has to decide whether to add a particular type of fertilizer and in what volume. For this, it would be useful if the sensors are queried, the sensor data is analyzed and the above decisions are made in real-time. When deciding on sequences of such field operations, knowledge of soil moisture, distances between fields, the likelihood of negative impacts on yield from delayed operations, etc. are important. Even the current location of machinery and workers would be important inputs to a model and can lead to improved efficiency and safety for time-sensitive tasks such as spraying, planting, harvest, and transport.

1.2 Motivation

One of the most challenging IoT applications is IoT enabled smart agriculture. Agriculture is one of the most important industries in human history. With the explosion of the human population, its importance is broadened and improving its production rate is essence to the fast-growing population. The agriculture industry has been adopting information and communication technologies (ICT). Incorporated with diverse sensors and actuators, automated farms can monitor the environment and make plans accordingly. Farmers can also use smart-phones to monitor the environments [7], [8]. A sensor network based automation system is built to monitor the agriculture environment [9]. The sensor requirements by farmlands are different according to the types of products the farms are planting. For example, a corn field may need temperature sensors, humidity sensors, nitrate sensors, and soil sensors. These sensors can give the basic condition of the environment so that farmers can prepare for the best season of planting.

Furthermore, accurate process condition monitoring is also becoming increasingly critical in a number of current industrial applications. These are especially required in a vacuum and cryogenic applications such as pharmaceutical manufacturing (e.g. lyophilization). In lyophilization which is known to be a slow and lengthy process, the product temperature has to be accurately maintained below the maximum allowable temperature to avoid product loss. Temperature sensors (i.e. wired thermocouples) are typically placed in the products in the processing chamber to monitor the temperature. This is however cumbersome as it leads to

complex cable management and is sub-optimal in a production environment. Consequently, wireless IoT sensor networks can play an important role in providing significant advantages in such environments.

This dissertation addresses the development of IoT WSNs for two challenging areas, namely smart agriculture and industrial lyophilization. For smart agriculture, a new LoRa-based hybrid low-power wide-area mesh network is proposed (Chapter 2). This hybrid network structure addresses the development of large-scale WSNs that are suitable for distinct application areas with real-world deployments. To enable the data collection with varying sensors as well as to support wide area coverage with low energy consumption, a novel IoT sensing platform was designed and manufactured integrating a micro-controller, wireless communication interfaces, and a hybrid network with short (2.4 GHz) and long-range (915 MHz) communication links. On the industrial lyophilization side, two novel low-power temperature sensing systems were proposed for tracking the lyophilization process. A fully wireless, multi-point temperature sensor system as a Process Analytical Technology (PAT) for lyophilization is proposed (chapter 3). In addition, a new non-invasive approach for measuring product temperature, namely virtual thermocouple, that enables non-invasive measurement of the product temperature by combining flexible multi-point temperature sensing probe, as well as multi-physics simulation is proposed in chapter 4.

1.3 Dissertation Organization

This dissertation is structured as follows:

Chapter 2 proposes and demonstrates the design and implementation of the based hybrid low-power wide-area mesh network [5]. An overview of current IoT technologies for large area wireless sensing networks for agriculture applications is provided. Some of the “real-world” challenges in developing such networks, namely the range in urban and rural environment, deployment cost, as well as power consumption from the deployment perspective were discussed. A general problem statement was proposed to address the ”real-world” challenges for developing such large-area wireless sensing network. In the end, the methodology and design for the novel network topology to overcome this problem was provided. Lastly, the performance of the hybrid network were demonstrated with two real-world deployments at

the Purdue University campus and at the university-owned farm. The results suggest that both networks have superior advantages in terms of cost, coverage, and power consumption comparing with other existing long-range IoT solutions, like LoRaWAN.

Chapter 3 proposes a fully wireless, multi-point temperature sensing system for monitoring the lyophilization process citejiang2018multi. An introduction to the lyophilization process and its importance was discussed. Some of the main challenges, which includes the continuous process monitoring for the primary drying process at pilot scale was also discussed. Then the methodology followed to overcome this problem was stated. A full design flow for both hardware and software for the multi-point temperature sensor is provided. Furthermore, to test the performance of the system, freeze dying tests were run with the wireless sensor system in a lab-scale freeze dryer with practically-important solutions based on sucrose and d-Mannitol. Moreover, the abilities of the wireless multi-point sensing system were expanded to track the sublimation process and to simultaneously determine the sublimation rate and the vial heat trans-fer coefficient. In the end, the possibilities of using the wireless multi-point temperature sensor system for real-time monitoring, process verification, and cycle optimization for pharmaceutical lyophilization in laboratory process development and GMP production were discussed.

Chapter 4 presents the design and implementation of the Virtual Thermocouple, a non-Invasive temperature measurement approach for controlled lyophilization. Three parts of this new technology were presented: 1) The flexible non-invasive multi-point sensing probe that is attached to the vials externally, 2) The low-power wireless electronics that read and transmits the data wirelessly. 3) The numerical model that translate the temperature profile measured from the vial wall to the product temperature. In addition, experimental results are provided to show that the proposed methods can effectively be used for monitoring the drying dynamics and product temperature during freeze-drying process in real-time and non-invasively.

Chapter 5 summarizes the contributions of this dissertation and discusses future opportunities.

2. HYBRID LOW-POWER WIDE-AREA MESH NETWORK FOR IOT APPLICATIONS

2.1 Introduction

Developing a large area wireless sensor network (WSN) comes with many challenges, such as harsh environmental conditions, communication range, quality of service (QoS), deployment cost and energy consumption (battery life). These technical challenges are further discussed in a technical report by Heng et al [10].

To handle the above challenges, a new custom wireless IoT hardware platform that is connected to temperature, humidity, and nitrate soil sensors and additional I/O pins for enabling the connections to other sensors were designed and fabricated in this work[5]. LoRa [11] was chosen as the communication protocol because of its long-range and low power consumption (Section 2.2.3). LoRa utilizes chirp spread spectrum (CSS) modulation and operates in the sub-GHz ISM band to void penetration capability and heavy in-band interference.

Furthermore, a lightweight, hybrid network was proposed, combining the advantages of wide-area coverage of LoRa and the ultra-low power consumption of ANT by integrating them into a mesh network with following design goals:

- Must be low-cost in system level, meaning not only hardware of the node is low-cost, the receiver (gateway) must be low-cost as well.
- Should be able to cover a large geographic area. For example, in the farming deployment, the network covers 2.2 km^2 of a farm and the campus deployment covers around 1.2 km^2 of Purdue campus.
- Has to be robust enough to survive the harsh environmental conditions and the network should able to handle node failures and recover from it.
- The deployment procedure for the IoT devices should not require any specific domain knowledge. Regular users should be able to simply install batteries to the IoT device.

- In addition to LoRa, the proposed network should also incorporate ultra-low power radio such as ANT to improve the performance and efficiency of the network in dense deployments.
- The proposed IoT device must be able to adopt to additional sensors.

To evaluate the performance of the proposed hybrid network, a series of experiments were conducted. First, several in-lab tests were conducted to show the power efficiency, deployment feasibility as well as the reliability of the network over time. Next, two large-scale real-world test were deployed in both rural (Throckmorton-Purdue Agricultural Center–TPAC) and urban areas (West Lafayette campus at Purdue University) .

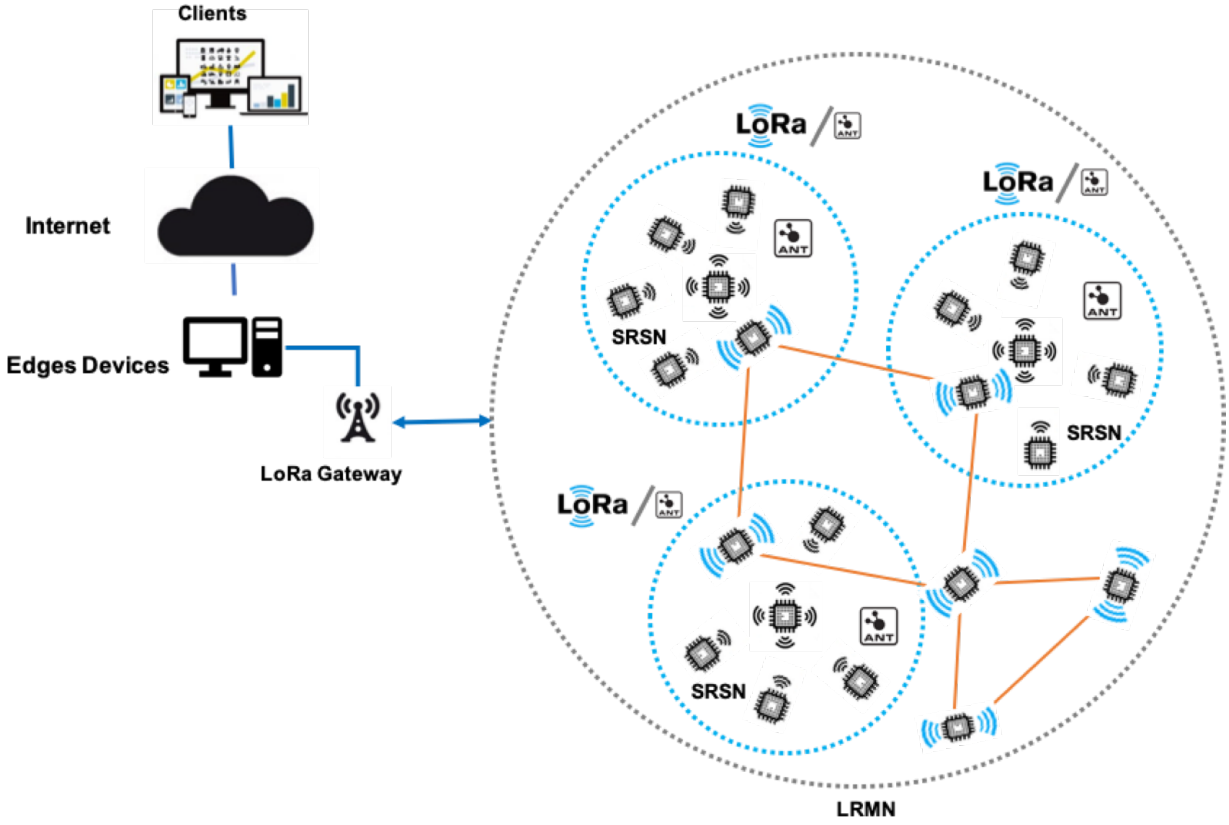

Figure 2.1. Hybrid Network Architecture. long-range Mesh Network (LRMN) consists of several Short Range Star Network (SRSN) and a few LoRa nodes.

2.2 Background and Related Works

2.2.1 Wireless Personal Area Networks (WPANs)

This section gives a brief overview of three popular WPAN protocols: Bluetooth/LE, ANT, and Zigbee.

Bluetooth/LE

Bluetooth is a wireless technology standard for exchanging data between devices in proximity over a short distance using short-wavelength UHF radio waves in the industrial, scientific and medical (ISM) bands, from 2.400 to 2.485 GHz. BLE stands for Bluetooth Low Energy, a low power version of Bluetooth. It provides rapid link establishment functions (simpler pairing) and 1 Mbit/s over-the-air bit-rate (with an option of 2 Mbit/s mode in Bluetooth 5). In addition, the maximum transmit power is 10 mW (100 mW in Bluetooth 5) for lower energy consumption with reduced range (<100 m). It supports a wireless sensor to run for at least one year with a single coin cell (approximately 200 milliampere hour (mAh)).

ANT

A new legacy protocol ANT [12] is popular because of its robustness and optimum energy consumption in developing WPAN applications, such as body parameter monitoring, smart homes, fitness sport services and gathering of the medical data within the range of 20 meters. It has similar performance in terms of power consumption and range with BLE and ZigBee [13]. This ultra-low power wireless technology supports different kinds of low data rate network topologies, such as peer-to-peer, star, and mesh. It communicates at 2.4 GHz frequency.

Zigbee

The ZigBee Alliance [14] is an association of companies working together to develop standards (and products) for reliable, cost-effective, low-power wireless networks. ZigBee builds upon the IEEE 802.15.4 standard [14] which defines the physical and Medium access

control (MAC) layers for low cost, low rate personal area networks. Zigbee operates in the ISM radio bands: 2.4 GHz in most jurisdictions worldwide; though some devices also use 784 MHz, 868 or 915 MHz depending on the regions. ZigBee defines the network layer specifications for star, tree and peer-to-peer network typologies.

2.2.2 Low-Power Wide-Area Network (LPWAN)

This section gives a brief overview and discusses the tradeoffs of the popular LPWANs technologies to provides perspective on why this work chooses LoRa.

LoRaWAN

LoRaWAN [15] is one of the most promising LPWAN solutions and is currently gaining traction to support IoT applications and services based on the LoRa radio modulation technology. LoRa modulation adpots the M-ary frequency shift keying (FSK) and Chirp Spread Spectrum (CSS) operating at 868 MHz (Europe) and 915MHz (North America) ISM band promising ranges up-to 20-25 km[16]. LoRa also supports an Adaptive Data Rate (ADR) from 300 bps to 50 kbps for a 125 kHz bandwidth and supports configurable chirp duration (spreading factor) to maximize both the battery life of each device and the overall capacity available through the system. LoRaWAN defines the MAC communication protocol and the system architecture for the WSN network that is being standardized by the LoRa Alliance [15]. The protocol uses a star-of stars type network topology, in which every Lora node can communicate directly with the Gateway module.

Sigfox

Sigfox is a proprietary Ultra Narrow Band (UNB) LPWAN solution that operates in the 869 MHz (Europe) and 915 MHz (North America) bands with an extremely narrow bandwidth (100 Hz). It is based on Random Frequency and Time Division Multiple Access (RFTDMA) and achieves a data rate around 100 bps in the uplink, with a maximum packet payload of 12 Bytes. However, Sigfox limits per amount of data per any device in the network to 14 packets/day. These limitations, together with a business model where SigFox owns

the network, have shifted the interest to LoRaWAN, which is considered more flexible and open[5].

NB-IoT

The 3rd Generation Partnership Project (3GPP) is a joint initiative of European, U.S., Japanese, and Korean telecommunications standardization organizations to produce global specifications for the Universal Mobile Telecommunication System (UMTS) [17]. 3GPP standardized a set of low cost and low complexity devices targeting Machine-Type-Communications (MTC) in Release 13. In particular, 3GPP addresses the IoT market from a threefold approach by standardizing the enhanced Machine Type Communications (eMTC), the Narrow Band IoT (NB-IoT) and the EC-GSM-IoT[4]. The Narrow Band IoT (NB-IoT) is one of the three IoT approaches standardized by the 3rd Generation Partnership Project (3GPP). The other two approaches are the enhanced Machine Type Communications (eMTC) and the EC-GSM-IoT[4]. Although these approaches reduce the energy consumption and the cost of the devices, they have not caught up their non-3GPP counterparts. For instance, the module cost for LoRaWAN and SigFox are both around $2-5 and eMTC is still around $8-12[18].

In conclusion, LoRa was used in this work because of the following advantages: i) the number of LoRa-enabled deployments is increasing continuously while, on the other hand, few initial NB-IoT deployments have been already performed; ii) LoRa operates in the ISM band whereas cellular IoT operates in licensed bands; this fact favors the private LoRa networks without the involvement of mobile operators; iii) LoRaWAN, a cloud-based medium access control (MAC) layer protocol based on LoRa, has growing backing from industry, e.g., LoRa Alliance, CISCO, IBM, and HP, among others.

2.2.3 Related Studies in LoRaWAN

The LoRaWAN network relies on the hub-and-spoke topology in which LoRaWAN gateways relay messages between end-devices and a central network server. This approach introduces two main problems: cost and power consumption. Deploying multiple gateways

for a large LoRaWAN network is expensive, since LoRaWAN gateways normally cost from hundreds to thousands of dollars. In addition, LoRaWAN gateways require internet access to communicate with the server, which for many applications, like smart agriculture, might not be available. In such cases, one needs to rely on cellular connection which increases the network development cost.

The second issue is the power consumption. To achieve optimal transmission, LoRa utilises the following configuration parameters: the carrier frequency, the spreading factor, the bandwidth and the coding rate [19]. The combination of these parameters affects energy consumption and transmission ranges. Taoufik et al.[20] calculated the theoretical maximum range that can be achieved at a given output power (P_{Tx}) level with different spreading factors (SF). In addition, they also proposed an energy consumption model based on these parameters as following:

$$E_{tx} = \frac{P_{cons}(P_{Tx}) \cdot (N_{Payload} + N_p + 4.25) \cdot 2^{SF}}{8 \cdot PL \cdot BW} \tag{2.1}$$

where E_{tx} is the energy consumed per bit, $P_{cons}(P_{Tx})$ is the total consumed power which depends on transmission power (P_{Tx}), PL is the payload size and BW is the bandwidth.

To achieve long communication ranges with LoRaWAN ($>$ 10 km), high spreading factors (SF) are required with a transmit power greater than 20 dBm (assuming a path-loss exponent equal to 3). However, a similar range can be achieved with 3 continuous hops using 3 different nodes with SF = 7. Lowering the spreading factor consumes significantly less energy. Total energy consumption for these two scenarios can be calculated based on Equation 2.1 for SX1262 LoRa transceivers at 20 dBm (P_{cons}(20dBm) = 389.4 mW [21]) with 8 bytes payload. Figure 2.2 shows the E_{tx} for all spreading factors (6 to 12).

Furthermore, because of the multi-hopping, the energy consumption for RX has to be considered as well and can be calculated as follows (P_{rx} = 15.2 mW [21]):

$$SF = 7, E_{rx} = \frac{P_{rx} \cdot T_{onair}}{8} = \frac{15.2 \cdot 36.096}{8 * 8} = 8.57\text{uJ/bit} \tag{2.2}$$

Hence, the total energy consumption for 3 hops is:

$$E_{Total} = 3 \cdot E_{tx} + 2 \cdot E_{rx} = 0.67\text{mJ} \tag{2.3}$$

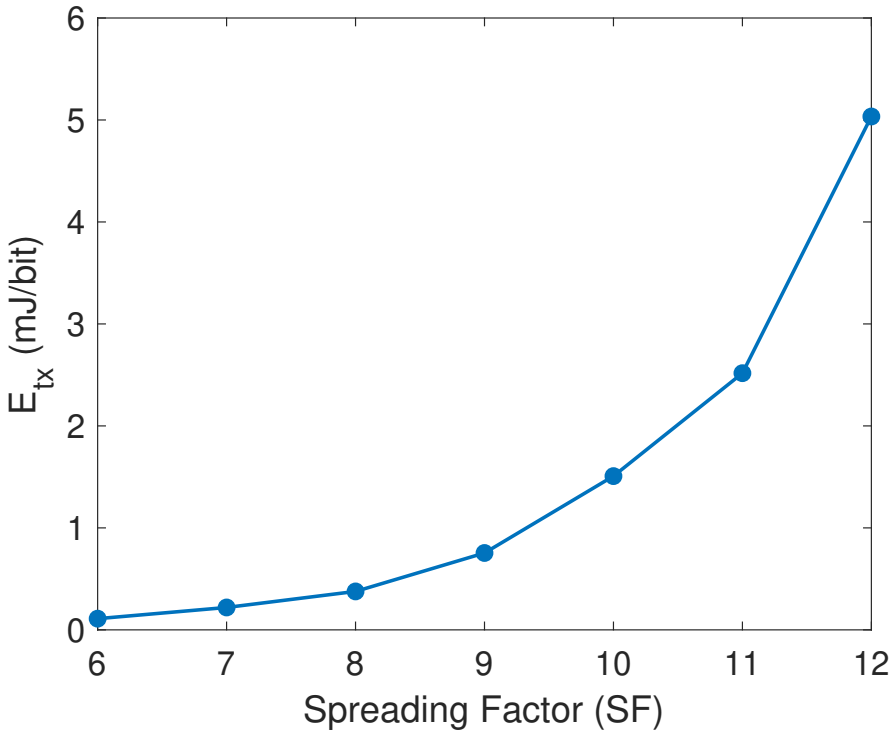

Figure 2.2. LoRa Time-on-Air vs different SF with 8 bytes payload (CR = 4/5, BW = 125kHz and 8 preamble symbols).

Similar observations could be found for SF9, SF10, SF11 and SF12. As a conclusion, for a battery operated LoRa network covering a large range ($> 10km$), a dynamic multi-hop mesh network could be much more efficient than LoRaWAN.

The power consumption is also distributed across multiple nodes, resulting in overall better life span for "battery driven" WSN compared with LoRaWAN.

In addition, LoRaWAN's asynchronous, ALOHA-based protocol limits its scalability and reliability[22]. Capacities of LoRaWAN networks are simulated and discussed in [23], which indicates that LoRaWAN network has very limited capacity due to desiccation and duty-cycle restrictions. Varsier and Schwoerer [24] found that PDR reduced to 25% due to packet collisions for a virtual large-scale application with high node densities. To overcome the limitations of LoRaWAN, more recent studies describe time-slot-based medium access mechanisms.

While Piyare et al.[25] describe an asynchronous time division multiple access (TDMA) with a separate wake-up radio channel (range of wake-up radio tested in lab environment, not multi-hop within sub-net), Reynders et al. [26] suggest using lightweight scheduling that needs an adoption of the LoRaWAN network.

2.2.4 Concurrent Transmission (CT) with LoRa

Chun-Hao Liao et al. [27] developed a concurrent transmission (CT) flooding-based multi-hop LoRa network with low collision rate by introducing random delay. They demonstrated a successful deployment of 18 sensors between multiple buildings across 290 m x 195 m area. However, their approach falls short in the following two design rules of WSN.

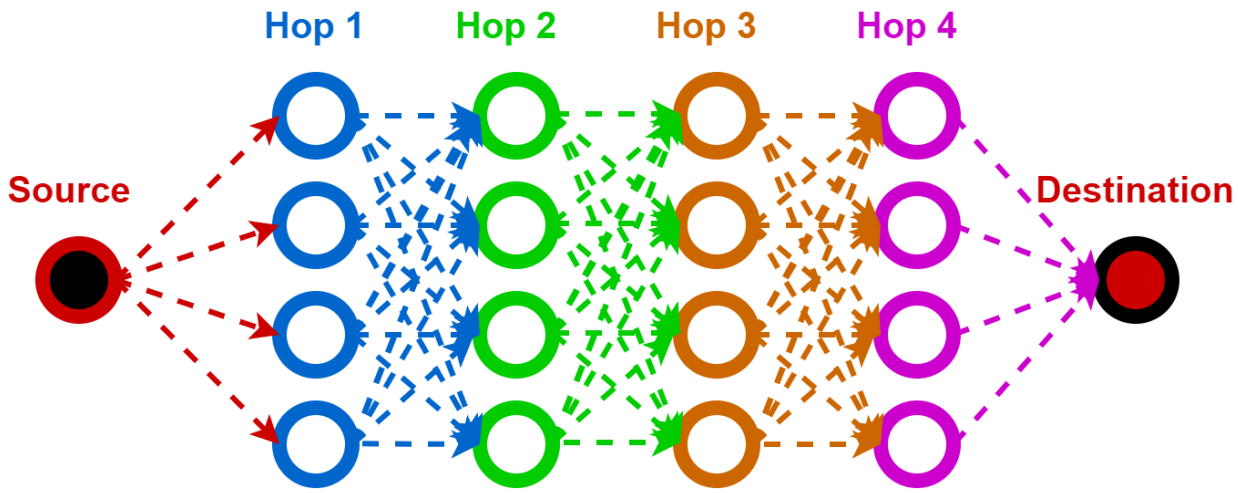

Figure 2.3. Demonstration of the LoRa concurrent transmission problem [27].

First, the CT-flooding approach is not applicable for WSN due to high-power consumption. Figure 2.3 shows a basic relay map of a CT-LoRa network with 18 sensors. For the sthece node to transmit one data package to the destination node, this CT-LoRa will have a total of 17 transmission and 17 receiving windows across the network, while in a very optimized network only 5 transmission and receiving windows are required for transmitting the same package. This is especially true for any "battery driven" LoRa based network since LoRa transmission is extremely expensive in terms of power when operating at high SF and transmission power.

Second, collision still exists with a high density of end devices. The authors studied the packet reception rate (PRR) with different numbers of relays for each node. The results show that the PRR degrades significantly as the number of relays increases. These drawbacks limit the general scalability of their work in WSN.

2.2.5 Synchronous LoRa Mesh Network

Recently, Ebi et al.[28] proposed a mesh network approach to extend the capability of LoRaWAN by integration with a linear mesh network with multi-hopping to monitor underground infrastructure. The key feature of their network is the use of intermediate repeater nodes (RN) that allow the formation of individual linear multi-hop network with clusters of sensor nodes (SN). RNs are designed to be placed above ground and have LoRaWAN connectivity to a gateway and act as a root for child (sensor) nodes, which are remotely placed beyond LoRaWAN coverage (underground). The RNs used two different LoRa transceivers to handle both LoRaWAN network as well as a linear LoRa mesh network. This concept was successfully tested and thoroughly evaluated in two full-scale field test with a total of 17 prototype devices. Although this network works for monitoring underground infrastructure, their implementation comes with some limitations. The bare-bone underlying structure is still LoRaWAN. As discussed in Section 2.2.3, the limitations of LoRaWAN still remain unsolved. In addition, the maximum number of the child-nodes is limited to 5 SNs due to the inherent payload restriction of the LoRaWAN standard. The authors also observed that the RNs consume about twice as much energy as SNs because of the additional LoRaWAN communication with the gateway. This means the RNs will drain faster than SNs in battery life, resulting in a disproportionate failure rate. When RNs fail, all connected SNs will lose the network connection. Thus these limitations could result in higher failure rates in certain nodes and non-optimal power consumption.

2.3 Methods

To enable the data collection with varying sensors as well as to support wide-area coverage with low energy consumption, a hybrid network was proposed with short and long-range

communication links and designed the own sensor node by integrating low-power microcontroller with dual wireless communication interfaces (915MHz and 2.4GHz) to support the proposed network.

2.3.1 Hybrid Network Architecture

The hybrid network architecture is shown in Figure 2.1. The proposed network topology is a mesh of multiple smaller star-topology sub-networks. LoRa was used to build a LRMN and ANT to build a SRSN for each individual sub-network. SRSN can cover a circular area of a radius of about 30 meters. SRSN works in the hub-and-spoke mode with a single hub node receiving data from multiple spoke nodes.

There are two reasons behind the hybrid architecture. First, the IoT network should enable data collection in a wide-area. Though LoRaWAN is capable of providing end-to-end communication of several miles, it suffers from high energy cost and the inadaptability of dynamic environments in applications like agriculture. Therefore, the long communication ability of LoRa was utilized to design the LRMN while the much more energy efficient SRSN was used for near-neighbor communication.

Second, for certain applications, there may be some areas with dense deployments of sensor nodes, in which LoRa is an overkill and will cause network contention. Therefore, SRSN was designed to collect data in such subareas for energy conservation.

2.3.2 The LoRa Mesh Network

TDMA Scheduling Algorithm

One important requirement for the mesh network is to ensure the data is successfully uploaded to the cloud, no matter how far the sensor node is from the LoRa gateway. Since the sensor node that is out of the communication range of a LoRa gateway needs to find a intermediate node for routing its data, the intermediate nodes and the sensor node need to coordinate the time window so that the intermediate node is in reception mode while the sensor node is sending its data. A trivial solution to this coordination problem is to always open the reception channel of the intermediate node. However, an always-on reception

channel is energy inefficient (approximately 10 mA current for the device in LoRa reception mode vs 2 μA in sleep mode, 5000 times increase in power).

Therefore, the TDMA scheduling algorithm [29] was adopted and customized it to the system. The pseudo-code is shown in Algorithm 1. The input, *nodelist* is the list of nodes in the network sorted in the descending hops to the LoRa gateway. Therefore, the algorithm starts with the node which is the furthest from the gateway (line 7 in Algorithm 1) and ends with the node which is closest to the gateway. There are three operating modes (Receive / Send / Sleep) of LoRa. The scheduling algorithm coordinates the sending and receiving actions for all nodes in the mesh network so that the data is transmitted without collisions with any other neighboring nodes that are also sending data at the same time. Additionally, customization puts the nodes mostly in Sleep mode. The difference between the original algorithm [29] and Algorithm 1 is that the original algorithm assumes a node can send all the data, including its own sensor data as well as the data received from other nodes, in the same packet in one timeslot. However, each node can only send data with fixed size. Therefore, if the data to be sent is too large, it has to be fragmented into multiple packets and sent at multiple timeslots. This customization is due to the packet size limitation in a single LoRa transmission. SX1262 LoRa transceiver [21], which was used in the deployment, has only 256 bytes of the transmission buffer. Thus, assuming the size of a single fragmented data packet is 256 bytes, if a node has received 3 packets from 3 neighbors plus 1 packet of its own sensor data, it will need to send 4 packets with 1 KB size of data. The 1 KB data cannot be fulfilled in one timeslot due to the SX1262 buffer limitation. Line 22 of Algorithm 1 checks the remaining packets (including those received from other nodes as well as the packets generated by itself) of a node and only after all of its packets have been scheduled, it will be removed from the node list so that the algorithm will not schedule it for the future timeslots. Section 2.3.3 gives a concrete example to explain how the mesh network is built up using Algorithms 1 and 2.

The Mesh Protocol

The LoRa node in the mesh network has three phases as shown in Figure 2.4, namely *Setup, Data Passing,* and *Sleep*. The first phase (line 2 to 6 in Algorithm 2) is the setup phase

Algorithm 1 LoRa Communication Mode Scheduling.

```
1: procedure BUILD SCHEDULE ON THE HUB NODE
   Input: nodelist
   Output: schedule
2:     do
3:         slot = new Slot();
4:         send_coll_list = [];
5:         recv_coll_list = [];
6:         while nodelist.length > 0 do
7:             node = nodelist[0];
8:             if (node.recv == 0
9:                 and
10:                node.packet > 0
11:                and
12:                !send_coll_list.contains(node)
13:                and
14:                !receive_coll_list.contains(node)) then
15:                slot[node] = SEND;
16:                slot[node.dest] = RECV;
17:                send_coll_list.insert(node.dest.nbrs)
18:                send_coll_list.insert(node.dest)
19:                recv_coll_list.insert(node.nbrs)
20:                node.dest.recv − −;
21:                node.packet − −;
22:                if (node.packet == 0) then
23:                    nodelist.remove(node);
24:        schedule.insert(slot)
25:    while slot.length > 0
26:    return schedule
```

where the nodes build up a routing table and the LoRa hub node builds a communication schedule that indicates the time window for which nodes to send data (Algorithm 1). The second phase (line 7 in Algorithm 2) is the data passing phase where each node follows the schedule to send or receive data. In the third phase (line 8 in Algorithm 2), the node sleeps to save energy since it knows no one will send data to it.

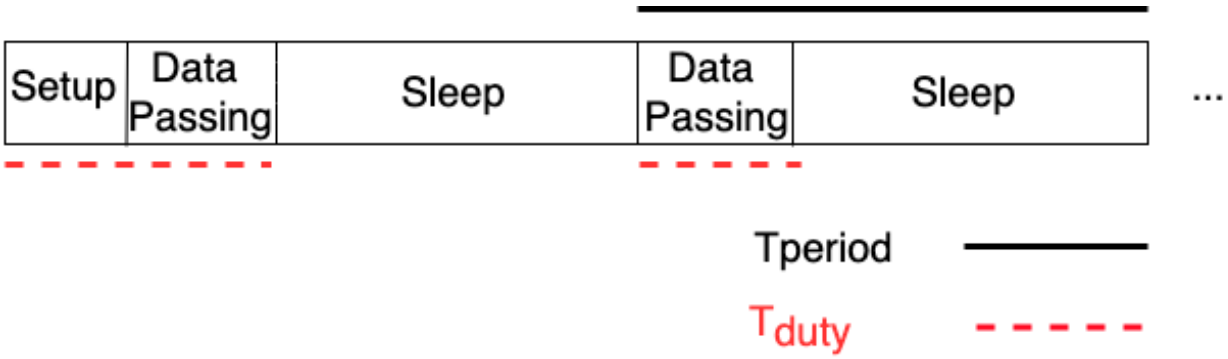

Figure 2.4. Three phases of the nodes in LoRa mesh. Duty cycle consists of the Initial Setup phase and any Data Passing phases. One period cycle consists of one Data Passing and the followed sleep phase.

Algorithm 2 LoRa Mesh Network Protocol.

1: **procedure** Operations of Each Node
Setup Phase
2: Each node builds local routing table using distance vector routing protocol.
3: Each node broadcasts its own routing table and forwards others' routing tables, for the purpose of gathering all routing tables at the Hub node.
4: Hub node builds the connectivity table for the whole network after collecting all routing tables from other nodes.
5: Hub node executes Algorithm 1 to build the communication schedule of each node and floods the schedule out; all the other nodes forward the schedule after receiving it.
Data Passing Phase
6: Each node sends / receives / sleeps based on the schedule.
Sleep Phase
7: All nodes sleep until the next Data Passing Phase.

2.3.3 Centralized Mesh Protocol

The communication in the mesh network must guarantee there is no collision where two nodes send data to a third node at the same time. Therefore, when creating the schedule for each node to communicate data, one needs to understand the whole network structure so as to avoid such communication collisions. Therefore, a centralized approach was designed where the hub node in the LoRa mesh is in charge of collecting information from other nodes to understand the whole network structure as well as creates the schedule according to the network structure. It first collects the routing table from each LRMN node so that, based on the neighborhood information of each node, it can construct the whole network structure,

namely the connectivity table referred in line 5 of Algorithm 2. Therefore, the scheduling algorithm is centralized and the node closest to the LoRa gateway was empirically chosen as the *LoRa hub* to do those jobs.

Build individual routing table

A simple version of routing information protocol [30] was used to create the routing table. Figure 2.5 shows how the routing table is built. The LoRa hub node broadcasts a hello message and whoever receives the hello message will rebroadcast it. The hello message includes the information of who the sender is and the shortest distance from the sender to the hub node. Eventually, all nodes will hear the hello message from their neighbors and build an individual routing table.

Collect individual routing table

The individual routing tables are sent to the hub to create the connectivity table, which is then referred by the TDMA algorithm to create routing schedules. Every node will broadcast its routing table to its neighbors. Additionally, when a node receives a routing table that it has not received yet, it will rebroadcast it. Eventually, after all the routing tables are collected at the hub node, the hub node will build a connectivity table that reflects the whole network structure. Figure 2.5 also shows the connectivity table for that mesh network.

Create schedules for all the nodes

The hub node will refer to the connectivity table as well as the customized TDMA scheduling algorithm in Section 2.3.2 to build the schedule of each node as shown in Table 2.1. The schedule is used by each node in the Data Passing phase to either send or receive data.

Recover from node failure

In case of a node failure, the associated nodes that normally receive data from the failed node will immediately discover the failure (no downlink communication from the failed node) during the next TDMA cycle, and will switch to reception mode for further instructions. Eventually, all nodes will not transmit anything, and the hub node detects that there is a failure. The hub node will issue a reset beacon message and floods it to all node with similar techniques discussed in Section 2.3.4. After receiving the beacon, the network will repeat the setup phase and recovers from the node failure.

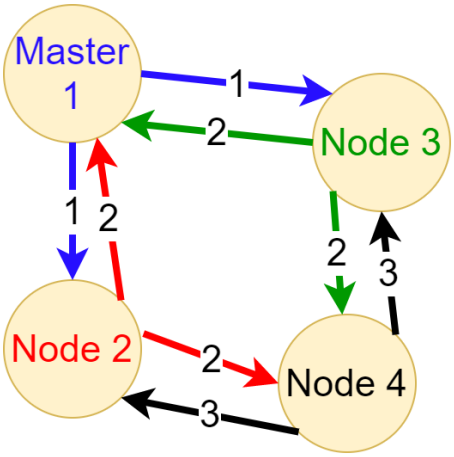

Hello Message Flooding

Node	Neighbors	Next	Hops
1	2, 3	Gateway	0
2	1, 4	1	1
3	1, 4	1	1
4	2, 3	2	2

Connectivity Table at Master node 1

Figure 2.5. Flood hello message to build routing table in each sensor node. After routing tables are built and collected by Node 1, a connectivity table is created to reflect the connectivity of the whole network.

Table 2.1. The schedule built for the network in Figure 2.5. After timeslot 6, all nodes switch to the sleep mode.

Node / Timeslot	**1**	**2**	**3**	**4**	**5**	**6**
1	Rx	Rx	Rx	Tx	Tx	Tx
2	Rx	Tx	Tx	Sleep	Sleep	Sleep
3	Tx	Sleep	Sleep	Sleep	Sleep	Sleep
4	Tx	Sleep	Sleep	Sleep	Sleep	Sleep

2.3.4 Time Synchronization

Time accuracy is crucial for any TDMA based collision-free network. Unsynchronized time across the network will result in data loss and network failure. In addition, without an external time source, the micro-controller often relies on crystal oscillator to record time. However, the crystal oscillator drifts over time. Therefore, periodic time synchronization over the network is required for stable operation. Ebi et al [28]. employ an external time sthece module (GPS) in their network to acquire the coordinated universal time (UTC) at RNs [28]. This time will transmit to the connected SNs by a ”beacon flooding” with TDMA scheduling. However, using TDMA in a LoRa mesh network for down-link communication will significantly increase the overhead of the network. On the other hand, concurrent flooding addressed the need of the smaller overhead at a cost of higher chances of package

collision [27]. Figure 2.6 demonstrates the possible collision that could happen in such approach. To overcome this issue, a random delay was inserted between the flooding messages to minimize the possibility of package collision similar to Liao et al.'s work [27].

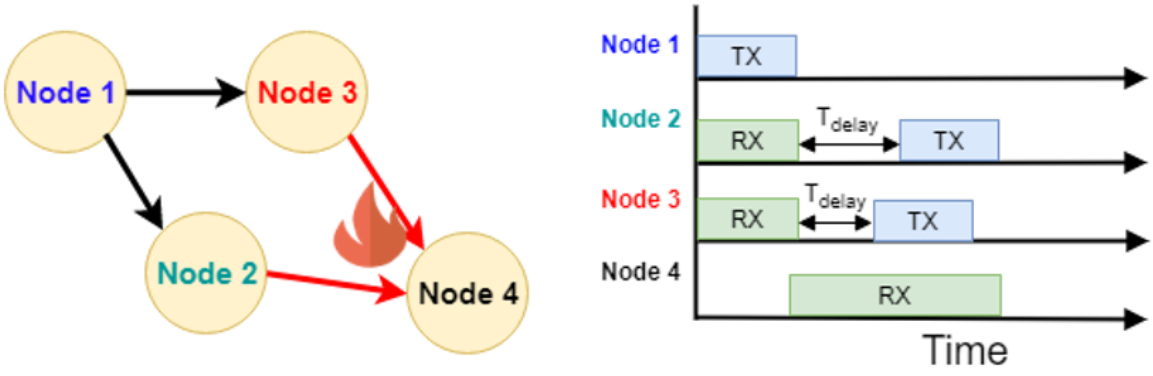

Figure 2.6. Left figure represents the possible package collision caused by time sync with concurrent flooding. Right figure shows the solution of the time synchronization process with a random delay.

Figure 2.6 shows the detailed time synchronization process, for each synchronization cycle, the center node (Node 1 in Figure 2.6) will initiate a 5 bytes beacon package containing sthece of this beacon (N_{sthece}), number of hops (N_{hops}) from the center node and the random delay (T_{delay}) before transmitting this beacon from the center node. Any node that receives this beacon will wait for T_{delay} that is smaller than the LoRa symbol time T_{symbol} and then immediately re-transmit this beacon. This approach minimizes the package collision as well as the down-link overhead since the flooding beacon is only 5 bytes. After the beacon has been received by the nodes, the relative time elapsed T_{past} since the previous node's transmission can be calculated as follows:

$$T_{past} = T_{beacon} + T_{node} + T_{delay} \tag{2.4}$$

where T_{node} is the time that is needed for node to process and re-transmit the beacon, T_{beacon} is the time on air of the package.

However, because of the variability of the T_{node} due to the SPI communication between the micro-controller and LoRa transceiver and the imperfect time synchronization, the receiving windows was manually expanded by 5 ms to compensate for the inconsistency. This process will synchronize the timing across all the nodes in the network to avoid the time drifts over a long period of time.

2.3.5 Adaptive LoRa Link (ALL)

One of the benefits of adapting the LoRa technology is the "degrees of freedom" at the physical layer. Ochoa et al. study suggested that the potential of an adaptive LoRa solution (i.e., in terms of spreading factor, bandwidth, transmission power, and topology) could greatly optimize energy consumption without sacrificing the communication range[31]. In the proposed LoRa mesh network, the proof of such concept by adopting the Adaptive LoRa Link (ALL) was provided to further improve the energy performance of the network. Although there are many physical parameters that can affect the energy of the LoRa link, SF and transmission power have the most impact in terms of the energy consumption. In this work, as a proof of concept, ALL is designed to only focusing on adjusting the transmission power of the network. However, similar methodologies will apply for adjusting the SF.

During the setup phase, in addition to building a routing table, each node will note the Received Signal Strength Indicator (RSSI) which is a estimated measure of the signal power level from each of the LoRa packages it received. Once the network is stabilized, during the first TDMA cycle, each node will be aware of the RSSI from its previous transmission. Then each node will adjust its P_{TX} based on collected RSSI value. After the adjustment, a new RSSI will be updated to verify the quality of each LoRa link (RSSI -120dBm). This process will increase the energy efficiency of each LoRa link without degrading link quality.

2.3.6 ANT Hub-and-Spoke Network

ANT was used to build the Short-Range Network (SRSN). ANT auto shared channel (ASC) is a communication channel specified by ANT [12], and it is used to build reliable bi-directional communication in a hub-and-spoke topology. The ASC communication structure

is shown in Figure 2.7. An ANT hub node receives data from other spoke nodes. All spoke nodes share a single channel to communicate with the hub. ASC supports up to 66K spoke nodes. By default, ASC requires a user specified channel master node to establish the network, a layer was added on top of that called Adaptive Mode Switching (AMS) to dynamically select the hub node. AMS is based on a round robin (based-on battery level) campaign to select the hub node. During the setup phase, each node will broadcast its ID and battery level and actively listens for other near-by ANT broadcast, node with the highest battery level will become the hub node. If multiple nodes have the same battery level, the node with the lowest ID will become the hub node. Once the hub node was selected, the ASC uses an ANT proprietary shared channel topology to establish the network, with the hub node being channel master and the rest of the nodes become shared slaves [12].

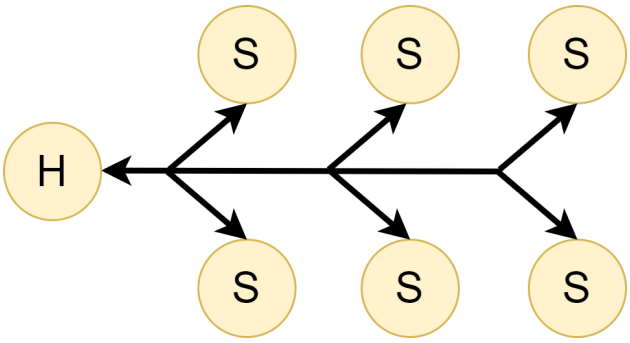

Figure 2.7. ANT shared channel hub-and-spoke network structure. H represents the hub node (Channel Master) and S represents the spoke node (shared slave).

In each SRSN, all the spoke nodes send data to a hub node via ANT and the hub node is in charge of uploading the aggregated data to the cloud. The hub node has two methods to upload the aggregated data. First, if the SRSN is a standalone network and associated with an ANT gateway, it does not need to enable the AMS functionality but directly sends data to the ANT gateway. Second, if the SRSN is part of a LRMN (the SRSN clusters in Figure 2.1), the hub node will switch to LoRa mode to route the aggregated data to the LoRa gateway. Clearly, the hub node consumes more energy than the spoke nodes. Therefore, AMS is used for balancing the energy consumption. Figure 2.8 demonstrates this idea. When a hub node drains to a lower-than-threshold battery level, it will issue a AMS message and the spoke

node with highest battery and within the same SRSN will be selected as the new hub. The original hub node then works as a spoke. This AMS feature guarantees no single node in SRSN is significantly drained and ensures the SRSN cluster still remains in the same LRMN network.

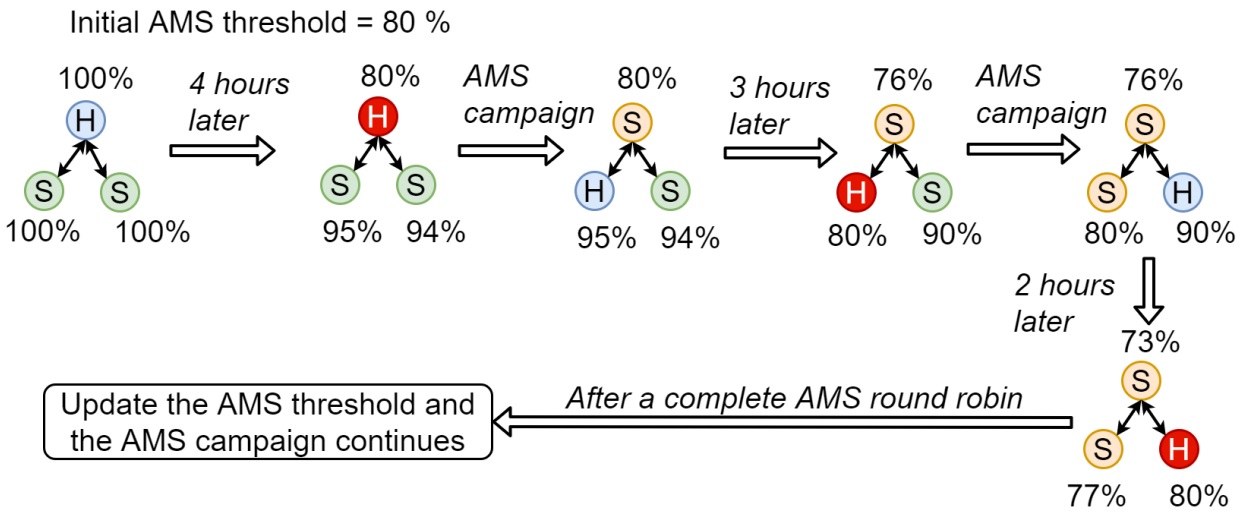

Figure 2.8. Adaptive Mode Switching (AMS) flowchart.

To address the potential failures of the hub node, a heuristic method was used: a timer (Failure Detection Timer in Figure 2.9) to detect the failure of the hub node. As shown in the left part of Figure 2.9, during normal operation, the hub node periodically sends an update request to each spoke node to request for new sensor and battery data. When a spoke node finishes data upload, the spoke node will reset the failure detection timer. This timer is set to be much longer than the data upload periodicity (e.g. 5 $\times$ periodicity) to count for any possible data loss. In the scenario of hub node failure (the right part of Figure 2.9, the timers on the hub nodes will expire and all the spoke nodes will reset themselves, resulting in the entire SRSN to be re-initialized. The remaining nodes will form a new SRSN without the failed node. After the new SRSN is initialized, the new hub node will switch on LoRa reception mode and wait for the next TDMA cycle to join back to the LoRa mesh network.

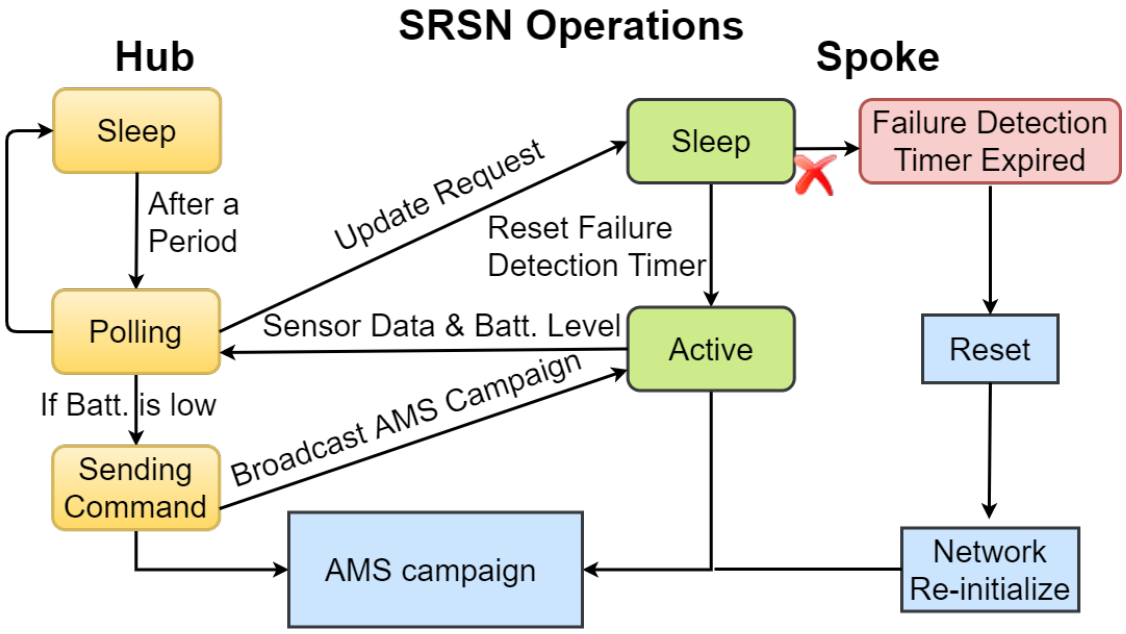

Figure 2.9. SRSN Normal Operations and Failure Tolerance.

2.3.7 Hardware Sensing Platform for the Deployment

There are three main challenges when designing the platform for deployment: building a sufficiently low weight, low cost and energy efficient hardware capable of mass production, incorporating numerous subsystems to facilitate various applications (e.g.smart agriculture and smart city), and protecting the electronics from harsh environmental conditions.

The hardware platform used in this study builds on the hardware platform that was reported in the earlier work[32] as shown in Figure 2.10 and Figure 2.11(a). It utilizes the HMAA-1220 wireless transceiver module (Figure 2.11(b)) from HuWoMobility[33]. The HMAA-1220 wireless transceiver was powered by nRF52832 chip from Nordic Semiconductor[34] and SX1262 LoRa transceiver from Semtech[35]. nRF52832 features a low power 32-bit ARM Cortex-M4F processor with a built-in-radio that operates in the 2.4 GHz ISM band and supports ANT, BLE and Bluetooth 5 wireless protocols with up-to +4 dBm transmit power. It is also equipped with 64 kB RAM and 512 kB of flash storage which can be used for storing data for in-node data analysis.

SX1262 from Semtech [21] is the new sub-GHz radio transceivers which is ideal for long-range wireless applications. It supports both LoRa modulation for LPWAN applications and

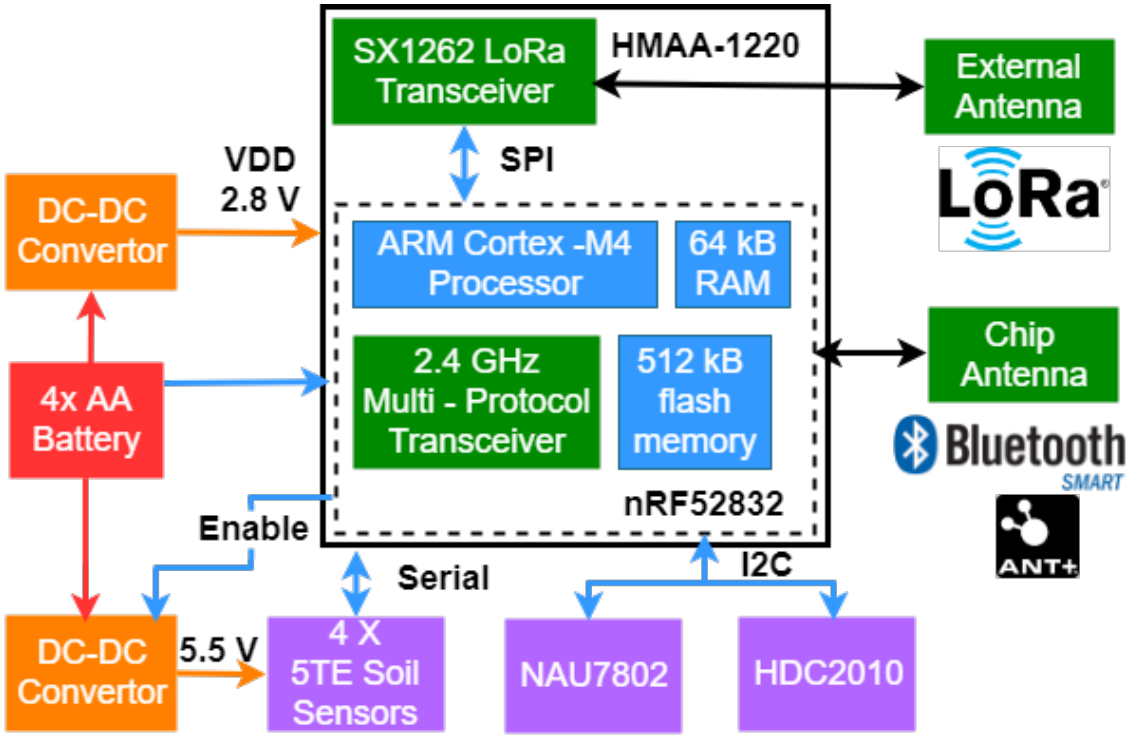

Figure 2.10. System block diagram of the hardware platform. Adopted from[32].

FSK modulation for legacy use cases. In addition, SX1262 also complies with the physical layer requirements of the LoRaWAN specification released by the LoRa Alliance[36] and the continuous frequency coverage of SX1262 from 150 MHz to 960 MHz allows the support of all major sub-GHz ISM bands. SX1262 was designed for long battery life with current consumption of 4.6 mA in active receive mode and 600 nA in sleep mode. With the highly efficient integrated power amplifiers, SX1262 can transmit up-to +22 dBm while having a high sensitivity down to -148 dBm. Along with the co-channel rejection of 19 dB in LoRa mode and 88 dB blocking immunity at 1 MHz offset, SX1262 provides a maximum of 170 dB link budget which is ideal for long distance communication.

Figure 2.11(a) shows the printed circuit board (PCB) with its packaging. The HMAA-1220 (Figure 2.11(b)) module was mounted on a "motherboard" with 4 LEDs and some pinouts for connecting different "daughter board" (Figure 2.11(c)). This design choice allow us to extend the flexibility of the hardware platform to facilitate different applications. The entire PCB was enclosed in an IP67 packaging for protection against environmental factors.

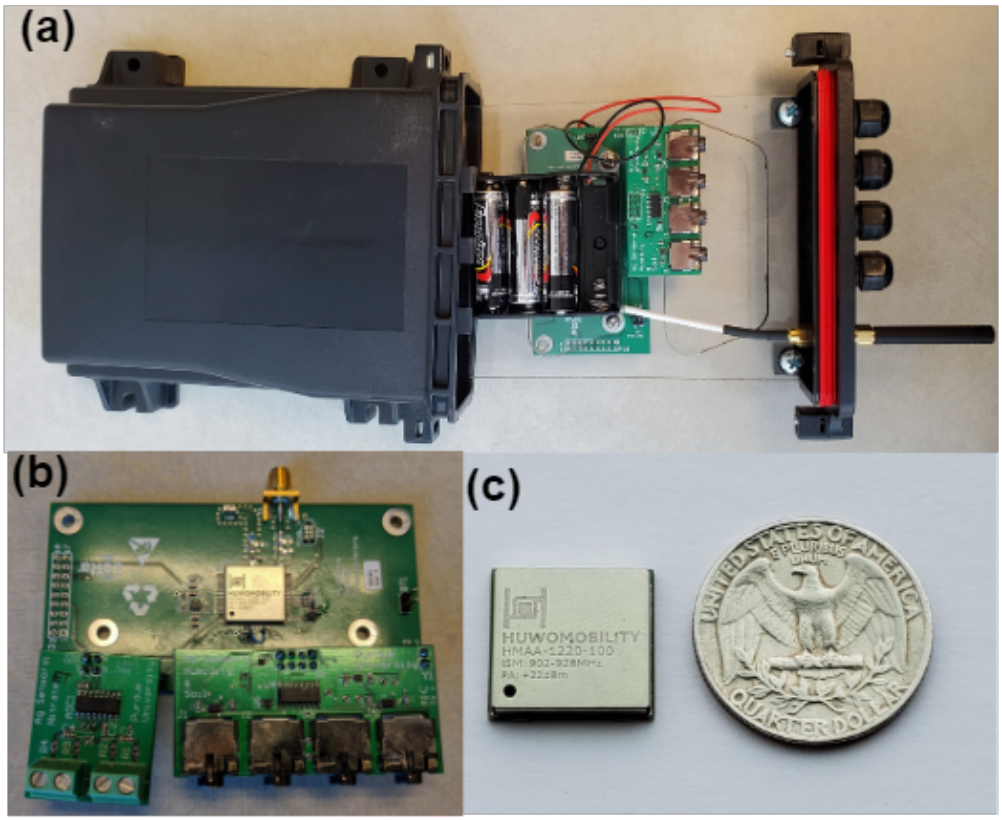

Figure 2.11. The hardware platform: (a) Motherboard PCB and battery holder with its packaging, (b) Motherboard PCB with two daughter boards, (c) The HMAA-1220 module.

2.4 Results

2.4.1 In-lab Evaluation

To verify the functionality and stability of the network, a series of both in-lab tests as well as real-world deployments was conducted.

Laboratory experiments was preformed with 9 sensor nodes with 1 node acting purely as standalone receiver monitoring the entire network to check the stability of the network.

Figure 2.12 shows the configuration of the network structure. All 8 nodes are placed together on a lab bench along with the receiver. Node 1 is the center node for this test. Testing the network structure in this condition is nontrivial since all sensors are in close proximity, the long-range capability of LoRa will not able to form the desired structure since all node are in range with each others no matter how the LoRa parameters were configured.

Table 2.2. LoRa configuration for the in-lab test and field deployment.

Parameter		In-lab test	Field Deployment
Spreading Factor	SF	7	7
Bandwidth	BW	125kHz	125kHz
Preamble length		8	8
Transmission Power	P_{Tx}	+0dBm	Variable
Coding Rate	CR	4/5	4/5
CRC checking		Head & Payload	Head & Payload

To resolve this issue, a filter was created in the low-level firmware (LoRa driver) to block connections from unwanted sensor nodes. For example, in the structure shown in Figure 2.12, Node 4 should only receive data from Node 3 and Node 5 in the desired structure. However, in reality, node 4 is able to receive data from all nodes because of the close proximity between sensors. The firmware filter will filter any data from nodes other than node 3 and node 5. All other data will be ignored to simulate the desired network structure. The biggest benefit of the approach is that the mesh-layer of the network is completely untouched, meaning from a network stack point of view, this lab test will be able to simulate the real-world conditions.

Table 2.2 shows the LoRa configuration of the lab experiment. To fully review the performance as well as the stability of the network, the network was kept running with each node programmed to transmit one 64 Bytes data package per minute (1.8 kBps) for an entire week. As the performance indicator, the receiver records all of the network traffic from all nodes. RSSI are not evaluated in this test since the TX power of all LoRa nodes was intentionally lowered. The reliability and stability of data packet delivery was evaluated for each individual node using the packet deliver rate (PDR), i.e. the ratio between the number at the center node (# RECEIVED) and the number of packets that should have been received (# EXPECTED). With the help of the traffic monitoring receiver, two sets of PDRs can be calculated, PDR_{i} and $Total\_PDR_d$:

$$PDR_{\text{i}} = \frac{\sum \#RECEIVED_{\text{i}}}{\sum \#EXPECTED_{\text{i}}} \tag{2.5}$$

where PDR_{i} is the packet delivery rate of node i during the entire week.

$$Total\_PDR_d = \frac{\sum_d \#RECEIVED}{\sum_d \#EXPECTED} \tag{2.6}$$

where $Total\_PDR_d$ is the total packet deliver rate of all the node during the #dth day.

The estimation of the number of expected packets is based on each specific node with constant transmission interval (1 min). Because of the nature of the multi-hop network, counting the number of packets arriving at the receiver will count for both node-specific performance as well as the multi-hop route from that specific node to the center node. In contrast, $Total\_PDR_d$ provides an overview of the network stability over time. Instead evaluating node-specific parameters, $Total\_PDR_d$ provides an overview of the system stability of time synchronization as well as the TDMA routing.

Figure 2.13(a) shows the results of the PDR_{i} of the one-week test, all nodes show more than 99% PDR except for node 4. Figure 2.13(b) shows the results of the $Total\_PDR_d$ for the same test, it suggests the network stability is very strong and is not time dependent.

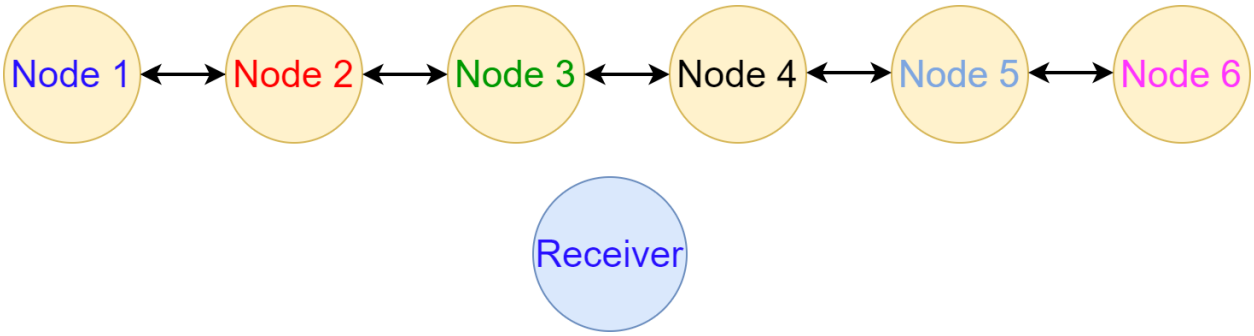

Figure 2.12. Network structure for the in-lab system stability test.

The power consumption was measured for one node under real-life conditions for a network structured with the nodes as shown in Fig 2.14. In addition, each sensor is connected with HDC2010 temperature and humidity sensor. For each cycle, each node will transmit a package of 64 bytes including one temperature and humidity reading. Due to the nature of the mesh network, energy consumption within the network varies depending on i) the position of the participating node in the hierarchy of the mesh network, and ii) the topology type of the network. As shown in Figure 2.14, node 1, 2, and 3 are connected with the

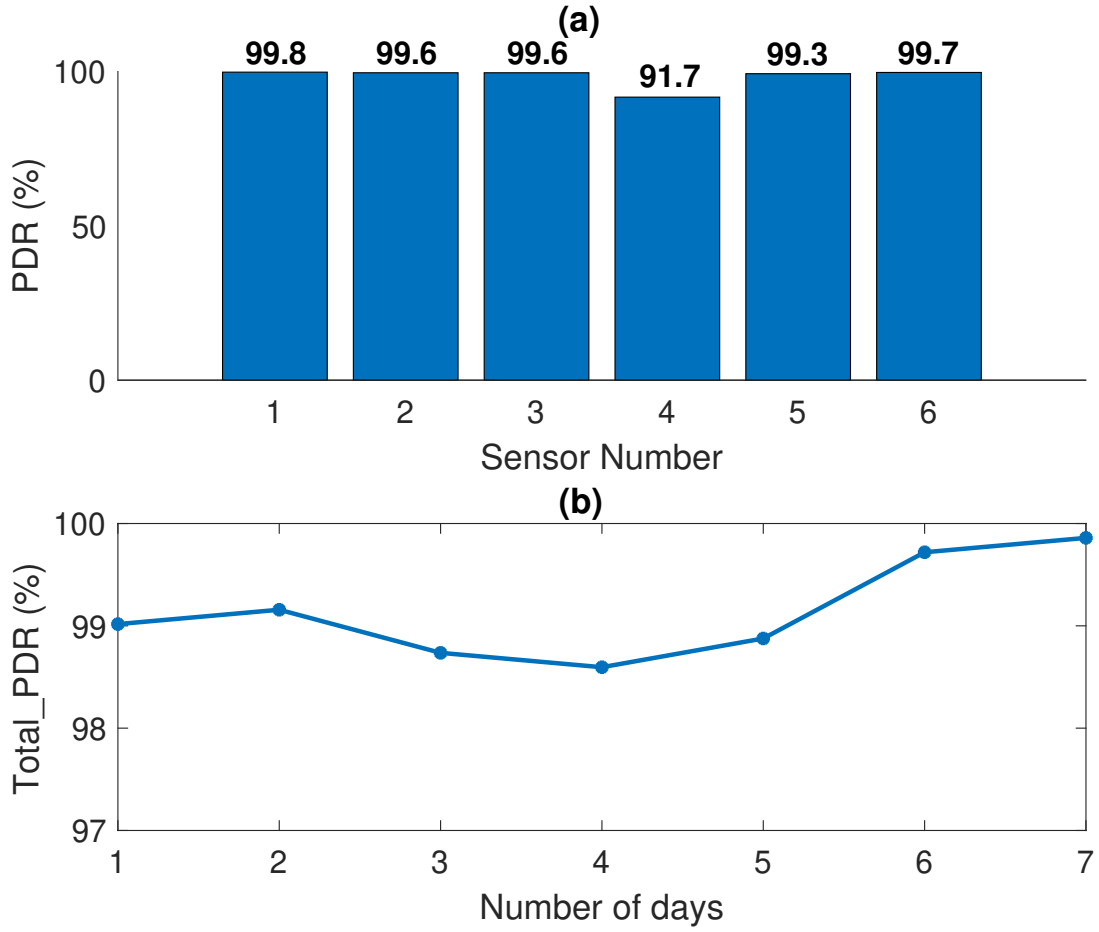

Figure 2.13. Results (PDR and $Total\_PDR$) for the in-lab system stability test.

proposed LoRa mesh protocol. Node 3 also communicates with node 4 via ANT. The goal of this configuration is to route the data from node 4 (ANT), node 3 (ANT + LoRa), and node 2 (LoRa) to node 1 (LoRa). For each TDMA scheduling cycle, node 4 will transmit one package via ANT to node 3 and node 3 will forward this package plus its own package to node 2 via the LoRa. Then, node 2 will transmit 3 packages (2 received + 1 own) to Node 1. The LoRa configuration for this test is identical to the field deployments with +18 dBm transmission power.

Power consumption was measured using a N6705B DC power analyzer from Agilent Technology[37]. Each sensor node is powered with 3.3 V DC by the DC power analyzer. Figure 2.15 shows part of the current profile of Node 3 where each state of operation is clearly marked. The hardware consumes around 25 μA during sleep, 10 mA during ANT

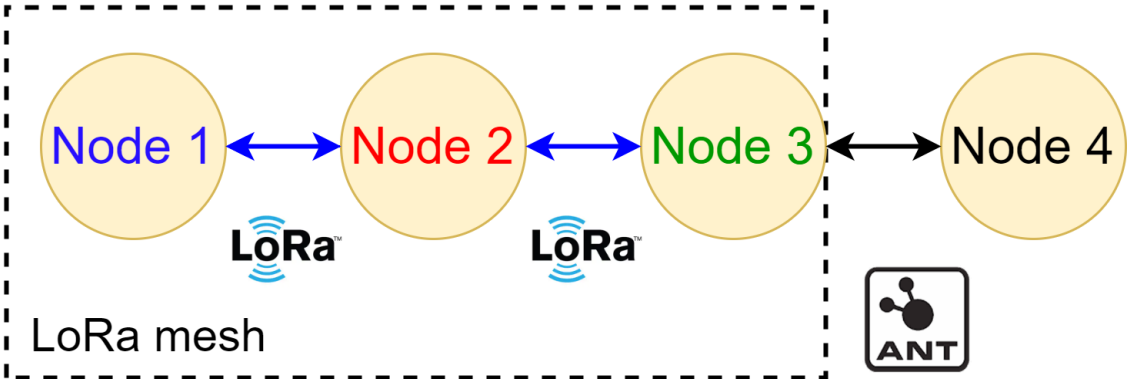

Figure 2.14. Network setup for the energy consumption test.

TX, 12.5 mA during LoRa RX and 72.5 mA during LoRa TX. Therefore, the average current consumption with 10 minutes TDMA cycle delay for Node 3 is 56 μA which can be translate to 5.2 years of expected battery life with standard AA alkaline batteries (2500 mAh). Table 2.3 shows the average current consumption and the expected battery life (with 2 AA alkaline batteries) of each node. Comparing between nodes 1, 2, and 3, the energy consumption of different nodes is determined by the number of receive/transmits windows. Note that Node 4 consumes significantly lower power. This shows that ANT radio is superior in terms of energy efficiency compared with LoRa. In conclusion, even though energy consumption is highly dependent on the network structure and while some nodes do consume high power, the network still has a very acceptable expected battery life across all nodes.

Table 2.3. Measured Power profile and Expected Battery Life with 2xAA Battery.

	Average Current Draw (I_{avg})	Expected Battery Life
Node 1	33 μA	9 years
Node 2	74 μA	4 years
Node 3	56 μA	5 years
Node 4	25 μA	11 years

To fully test the performance and durability of the hardware platform against harsh environments, 4 units equipped with the smart agriculture interface was deployed at Throckmorton-Purdue Agricultural Center (TPAC) at Purdue University. All units were equipped with temperature and humidity sensors to monitor the environmental conditions at the farm and were placed 1 meter above the ground. The deployment locations are shown in Figure 2.17. Two

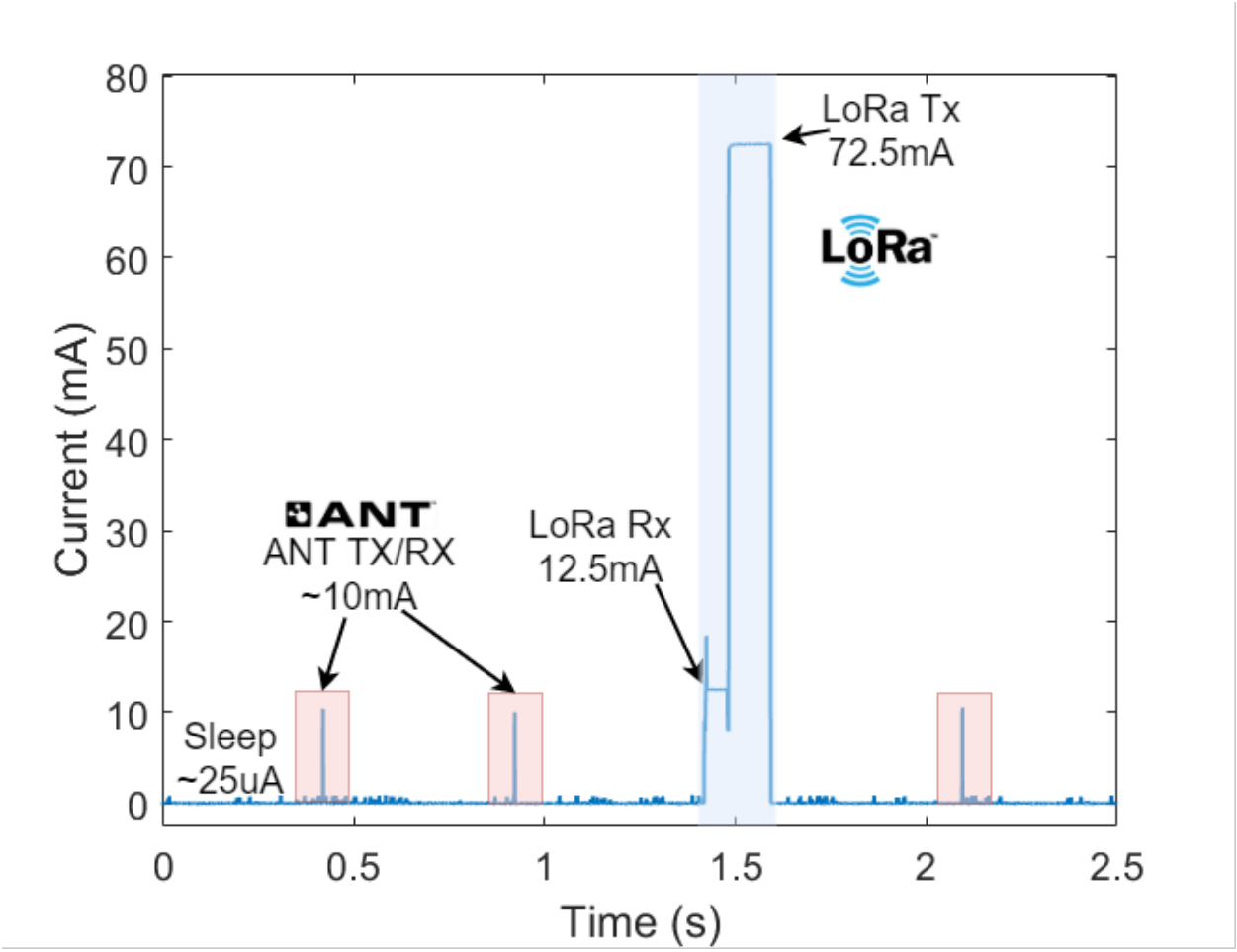

Figure 2.15. Measured current profile for Node 3 during one transmission cycle where blue region represents LoRa's Tx and Rx windows and red region represents the ANT transmission window.

of the units with printed thin-film nitrate sensors were installed in the stream to measure the nitrate pollutants from fertilizer runoffs in the stream. The other two units were interfaced with the independent ECH2O 5TE Soil sensors to monitor the soil temperature, conductivity, moisture, and dielectric at the different depths[38]. All the units were programmed to send data every 10 minutes and the data received at the receiver is uploaded to the data server and displayed on the web. As of January 2020, these units have been continuously operating for more than a year without major failure. The highest temperature recorded is above 110 ^oF and the lowest temperature is -40 ^oF. This proves the hardware is capable of

withstanding harsh environmental conditions while being in situ in an unmonitored outdoor environment.

2.4.2 Large-scale Deployment

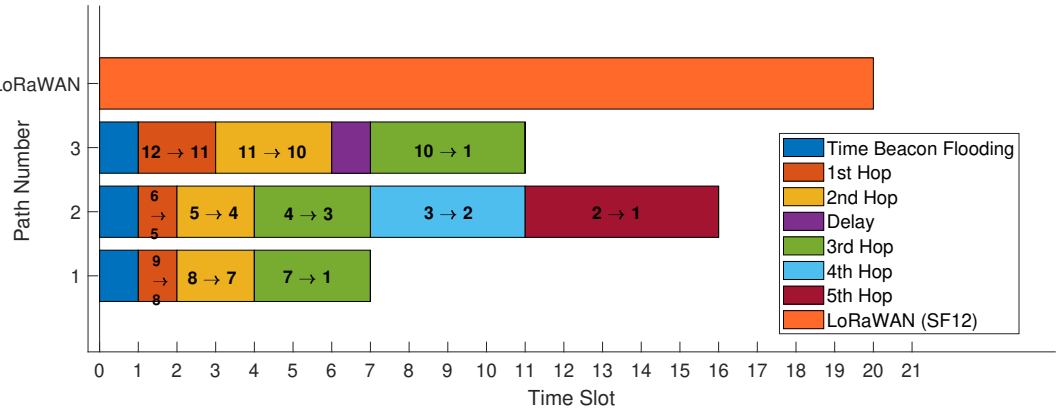

Figure 2.16. TDMA schedule of the campus deployed network, each Hop is clearly marked. Path 1 to 3 corresponds to the path from Figure 2.19. The total length represents the total overhead of the corresponding path.

The proposed network was first tested in TPAC to evaluate the multi-hop performance of the mesh network for covering long-ranges. Five mesh nodes were deployed in linear hop formation in addition to the existing 4 sensing nodes equipped with soil moisture sensors and flexible nitrate sensors. The newly deployed mesh nodes were equipped with temperature and humidity sensors as well as nitrate sensors and powered with 4 AA batteries. Figure 2.17 shows the map of the farm deployment: The green dot represents the receiving computer; the red dot represents the center node of the mesh network; the blue dots represents the 5 mesh nodes; the yellow dots represent the the previously deployed sensor nodes that were not part of the mesh network. The LoRa configuration of each node is shown in Table 2.2 with SF7 and TX power = 15 dBm. Each node was programmed to send one 64-byte packet every 10 minutes. Once each cycle is complete, the center node will forward the packages to the receiver for upload. With 4 linear hops, the proposed mesh network is able to cover 3 km in farmland with more than 98% PDR across all nodes with SF7. This experiment

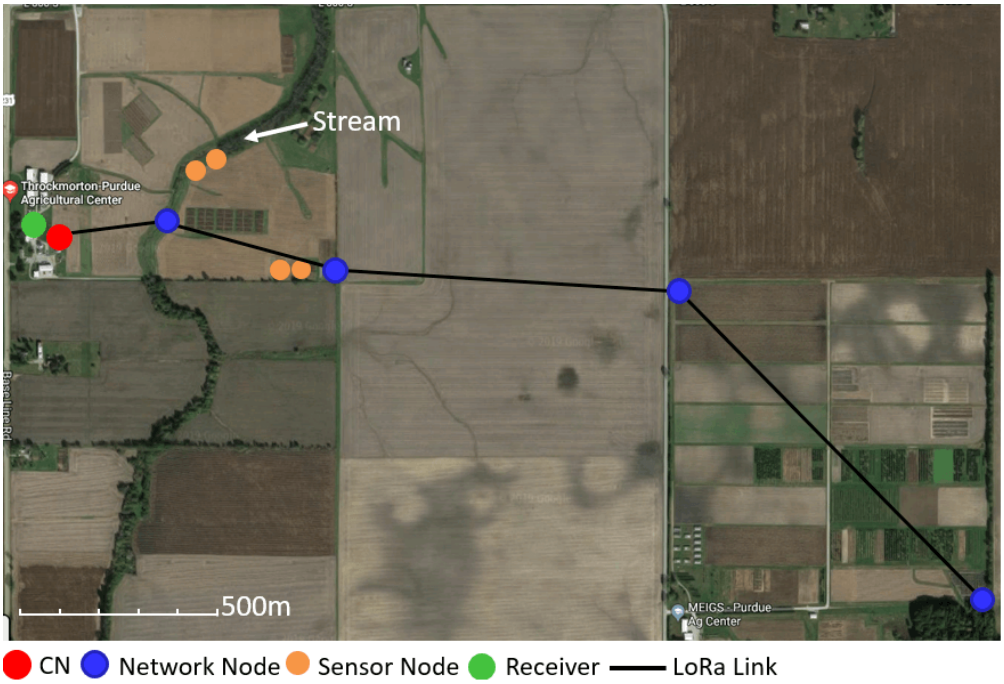

Figure 2.17. Deployment of the proposed mesh network at TPAC. Each blue dot represents a LoRa mesh node and the black line represent a stable LoRa link.

confirmed that the mesh network is able to cover long distances with low spreading factor (SF7).

In the campus-scale deployment, 13 LoRa nodes were placed, distributed in a 1.1 km by 1.8 km area of Purdue University campus. All 13 nodes were deployed and continuously operated for a period of two weeks. Figure 2.19 shows the complete map of the campus-scale experiment where a complete mesh network is established. Each blue dot represents a network node which is randomly and evenly distributed across the entire Purdue campus (Figure 2.18(a)). The red node represents the location of the center node. The green dot represents the receiver, a laptop connected with $SX1272DVK1CAS$ (LoRa development kit) from Semtech[39]. Each solid line represents the actual LoRa link for the deployed network and the dotted line represents available LoRa links that were not being used. The node junction represents two nodes (node 12 and node 13) that were deployed on purpose at close range and were communicating via ANT instead of LoRa (Figure 2.18(b)). In addition, three paths that are highlighted in Figure 2.19 represent three distinguished data flows that

Figure 2.18. Deployment at Purdue campus. (a) node 7 installed on a street lamp post, (b) node junction consisting node 12 and 13 next to a campus building.

are formed by the mesh network. For instance, path number 1 represents the path 9 → 8 → 7 → 1. All nodes (including the center node) are located 1 meter above ground level as shown in Figure 2.18 and the receiver is placed on the 3rd floor inside of an office building facing south-east. The furthest node is placed 1.5 km away from the receiver and across more than 18 buildings in between.

Each node was programmed to transmit 64 Byte package at a fixed time interval (2 minute) with the LoRa configuration shown in Table 2.2. In addition, two furthest nodes 6 and 9 will send an additional package with SF12 outside of the TDMA cycle as comparison with transitional ALOHA based network such as LoRaWAN. Furthermore, since the LoRa radio of node 13 in the node junction was not active (it only communicates to node 12 via ANT), it was enabled to broadcast (in parallel with the mesh network, acting like a LoRaWAN node) with SF12 directly to the receiver used as the comparison for evaluation. After each transmission cycle, the center node will forward all incoming packages to the receiver which will upload all data to the cloud for future analysis. All data packages are checked with 16-bit Cyclic Redundancy Check (CRC) to verify their integrity, corrupted data package will be marked and stored. Figure 2.16 shows the TDMA schedule of the deployed

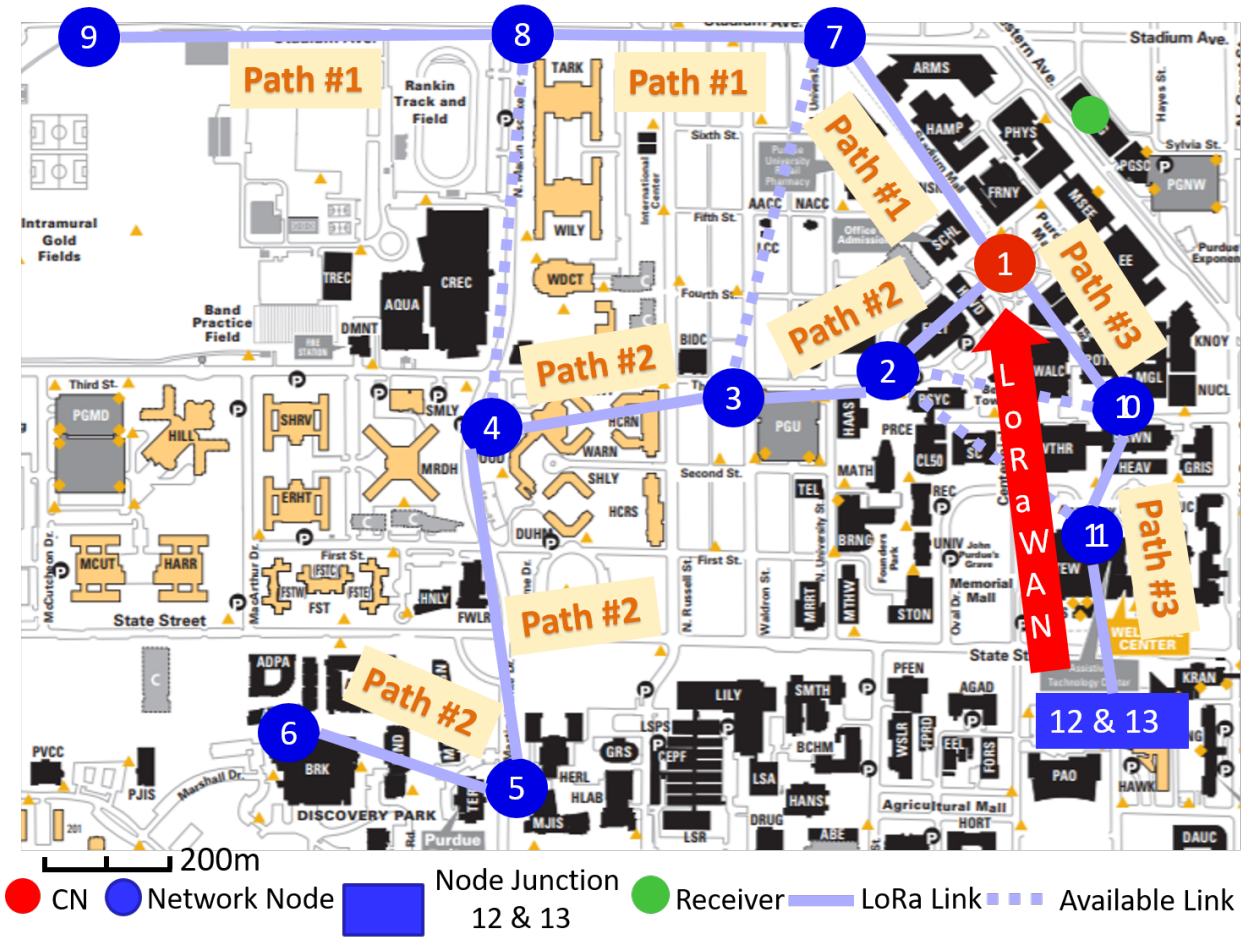

Figure 2.19. Map of the network deployment on Purdue campus with 13 nodes. The red dot represents the center node (CN), the network nodes are represented as blue dots, the blue square represents the node junction (Node 12 and 13) and the green dots represent the receiver.

network with each slot set to 125 ms for transmitting a 64 Byte package. The three paths represent the three continuous LoRa links as shown in Figure 2.19. Each section represents one different LoRa hop and are color coded for clarity. The delay inserted after the 3rd hop is required to avoid package collision with node 7 from path 1. SF12 reference represents the time it took for one 64 Bytes transmission with SF12 as comparison. It is clear that even for the longest path (Path #2) with 5 hops in between, the overhead of the furthest mesh node (Node 6) is smaller than the single-hop LoRaWAN node. However, it is worth noticing that the overheads are greater for the nodes that were closer to the center node (node 7, 10, and 2) and it is a necessary trade-off between power efficiency and network robustness.

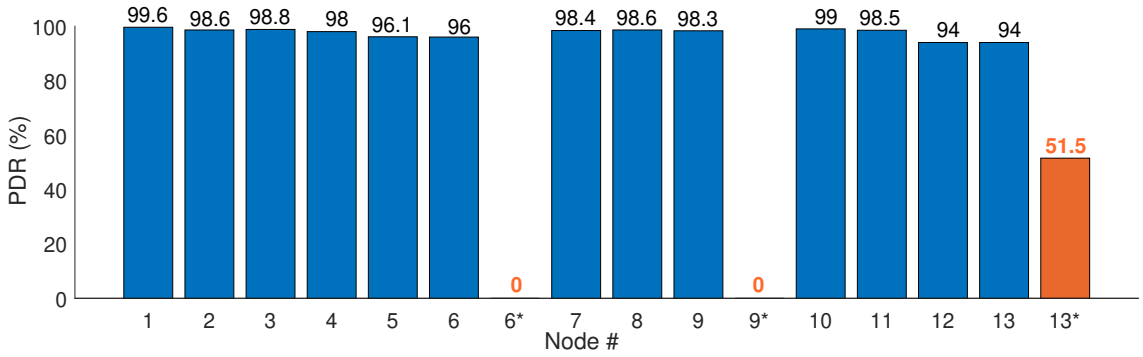

Figure 2.20. Packet Delivery Rate (PDR). Blue bars represent nodes 1 to 13 across the network. Orange bar represents the SF12 LoRaWAN reference from node 6, 9, and 13 respectively.

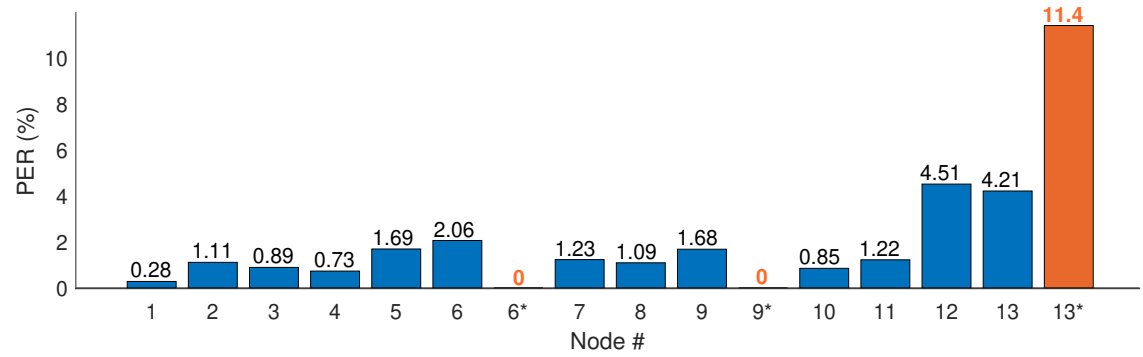

Figure 2.21. Package Error Rate (PER). Blue bars represent nodes 1 to 13 across the network. Orange bar represents the SF12 LoRaWAN reference from node 6, 9, and 13 respectively.

Over the entire evaluation period of two weeks, each node transmitted one 64 Byte package every two minutes, which means a total of 9360 packages were expected from each node (13 days of operation were considered, network was taken down by one day for evaluation). As in the previous section, the network integrity is evaluated by analyzing PDR of all nodes. In addition, the Package Miss Rate (PMR) and Package Error Rate (PER) are analyzed as well. Similar to PDR, PER is calculated based on the number of the package that were marked as corrupted and PMR are calculated based on number of missed packages:

$$[ht]PER_{\mathrm{i}} = \frac{\sum \#ERROR_{\mathrm{i}}}{\sum \#EXPECTED_{\mathrm{i}}} \tag{2.7}$$

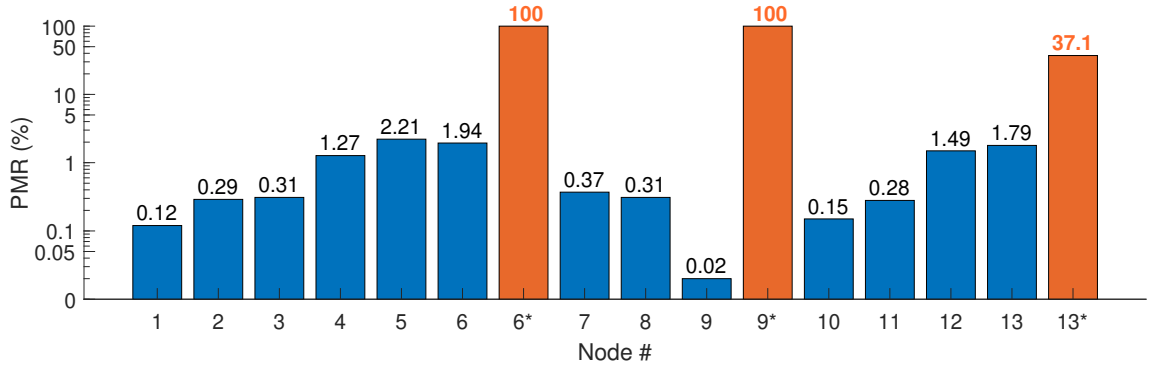

Figure 2.22. Package Miss Rate (PMR). Blue bars represent nodes 1 to 13 across the network. Orange bar represents the SF12 LoRaWAN reference from node 6, 9, and 13 respectively.

$$[ht]PMR_{\text{i}} = \frac{\sum \#EXPECTED_{\text{i}} - \sum \#RECEIVED_{\text{i}}}{\sum \#EXPECTED_{\text{i}}} \tag{2.8}$$

Figure 2.20, 2.21, and 2.22 show the end-to-end PDR, PMR and PER based on the total expected number of packages and received packages for all 13 nodes including the SF12 reference, where the blue bars represent all nodes in the mesh network, and the orange bar represents the SF12 reference. Over the entire deployment period of two weeks, the proposed mesh network achieves more than 96% PDR except for node 12 and node 13 comparing to 51.5% of the SF12 reference node. In addition, from Figure 2.21 and 2.22, both the PMR and PER for all nodes are significantly lower than the SF12 reference node. This confirms that the proposed network provides much better quality of service particularly for large area networks. Where higher spreading factors are necessary for transitional star network to cover such as in the ALOHA protocol in LoRaWAN's approach, it is worth noticing that the PMR increases as the number of hops increases. This is expected since the time flooding will degrade as the number of hops increases. Imperfect time synchronization will cause time slot mismatch and therefore results in either missed packages (TX/RX window mismatch) or package collision (TXs windows miss match). However, from the observation based on the results from Figure 2.20, 2.21, and 2.22, although both of the PMR and PER did trend to increase as number of hops increased, these effects are minimal comparing with the PDR. Furthermore, node 12 and 13 showed much higher PER ($> 4\%$); This might be due to higher

interference in the sub-GHz ISM band since both of those two nodes were located in one of the most populated areas on campus. On the other hand, the LoRaWAN reference node 13* shows a very low PDR (51.5%) and very high PER and PMR, when compared to the mesh node deployed at the same location (node 12). This confirms that the mesh is able to provide better quality of service which further supports the proposed network structure.

2.5 Limitations

As Ochoa et al. [31] point out, the energy consumption of LoRa mesh nodes can be further optimized by exploiting different radio configurations and the *network topology* (e.g., the number of hops, the network density, the cell coverage). For sparse networks, higher SF is necessary along with higher transmitted power. The Adaptive LoRa Link in the implementation did not include the functionality to change the spreading factor as the network topology in the deployment did not change over time. One aspect of the future work is to include such adaptivity in the implementation.

Another important limitation of the network occurs during the flooding for the TDMA scheduling. In the current configuration, one TDMA schedule table for the entire network is flooded to each node for the simplicity of the design. However, there are two inherent problems with this approach. First, flooding the entire table requires transmitting multiple LoRa packages throughout the entire network. Not only is this approach inefficient, but it also increases the overhead for the setup phase. Second, due to the limitation of the maximum data package (255 bytes at SF7) of LoRa, the maximum number of nodes in the network will be limited. Although, this limitation can be patched with flooding multiple schedule tables throughout the network, this approach will still be inefficient and will significantly impact the overhead during the setup phase. For the future work, instead of flooding a entire network table to every node, the table will be divided, based on the routing path. Only the necessary TDMA schedule will be flooded to each multi-hop path in the network. This approach will significantly reduce the overhead time during the setup phase without sacrificing the network performance.

While LoRaWAN allows for AES 128-bit encryption, in the current phase of the work, no encryption mechanisms have been deployed. While the plan is to deploy AES-128 encryption

in future LoRaWAN deployments, a caveat of introducing secure network channels will be the reduction of the available payload size, which may further limit the number of supportable nodes in a sub-network. Thus, future work will include look into deploying lightweight encryption mechanisms for IoT devices, such as ACES [40], [41].

As for the sensor data management, there are several other challenges about network latency and data analytics, which are discussed in more details in [10].

2.6 Conclusion

The recent advancement of the Internet of Things (IoT) enables the possibility of data collection from diverse environments using IoT/mobile devices. However, despite the rapid advancement of low-power communication technologies, the deployment of IoT network still faces many challenges. In particular, large-scale WSN such as digital agriculture and smart and connected cities remains a major challenge in terms of communication range, quality of service and power consumption.

This chapter presents the design of a hybrid LPWAN mesh network for IoT application that delivers data across several-kilometers with only low-power nodes while provides excellent QoS. the work addresses the development of large-scale WSN that is suitable for distinct application areas with real world deployments. To enable the data collection with varying sensors as well as to support wide-area coverage with low energy consumption, a sensor node was designed and manufactured integrating a micro-controller, wireless communication interfaces, and a hybrid network with short (2.4 GHz) and long-range (915 MHz) communication links.

With the hybrid mesh network, a significant improvement was shown in both power consumption as well as communication range while comparing with traditional single hop network like LoRaWAN. In addition, full-scale real-world experiments on both Purdue Campus and agricultural farms with more than 20 nodes further suggested that the proposed network significantly improves the quality of service while maintain long-term stability. Several areas of future work motivated by the design and experiments on these large scale IoT testbeds was provided, including sophisticated anomaly detection, on-device computation, and network synchronization. Therefore, the proposed hybrid network makes a valuable con-

tribution in WSN related research and enables the possibility of data collection from diverse environments using IoT devices.

3. WIRELESS MULTI-POINT TEMPERATURE SENSOR FOR PHARMACEUTICAL LYOPHILIZATION

3.1 Introduction

Accurate process condition monitoring is also becoming increasingly critical in a number of current industrial applications. These are especially required in a vacuum and cryogenic applications such as pharmaceutical manufacturing (e.g.lyophilization). Lyophilization, or freeze-drying, is a commonly used and well-established process to preserve the original structure of a heat sensitive biological and/or pharmaceutical product (e.g. Anti-body, peptides, vaccines, etc.) during drying and, moreover, during long-term storage (extending the shelf life of pharmaceutical formulations. Freeze-drying involves ice removal from a frozen product at low pressure through a sublimation process. It was reported by the Food and Drug Administration (FDA) that about 50% of over 300 FDA and EMA approved biopharmaceutical products are freeze-dried[42].

A typical freeze-drying cycle consists of three steps. First, the solution is completely solidified during the freezing step. In the following step, denoted as primary drying, the pressure in the drying chamber is reduced and the shelf temperature is elevated to allow sustaining ice sublimation. After the initial ramping phase to the desired shelf set-point, the heat supplied by the shelves and the removal of heat by sublimation is balanced and the system is in steady state. In this initial drying phase, the majority of the water in the material is sublimated. The last step, denoted as secondary drying, aims to remove unfrozen water molecules, since the ice was removed in the primary drying phase. In this phase, the shelf temperature is raised higher than in the primary drying phase to break any physico-chemical interactions that have formed between the water molecules and the frozen material. During the primary drying phase, as the ice sublimation is a process that requires energy, heat has to be supplied to the product, and its temperature increases with respect to the value achieved at the end of the freezing stage. This drying process is particularly suitable for pharmaceutical products, in particular when it is required to process a liquid formulation containing the active pharmaceutical ingredient (and the excipients), and water removal is required to increase the shelf life of the product[43], [44].

3.1.1 Main Challenges

Aiming to preserve product quality it is necessary that product temperature does not trespass a threshold value throughout the process and, in particular, during the primary drying stage. This threshold value is a characteristic of the product being freeze-dried, and for amorphous products, it is usually related to the glass transition temperature of the dried product. This aims to avoid the collapse of the dried product, that could result in a higher moisture content in the final product, in a longer reconstitution time, and in an unacceptable appearance of the product[45]–[47].

In addition to the temperature, sublimation rate is also an important indicator for optimizing shelf temperature and chamber pressure during primary drying. In addition, the vial heat transfer coefficient (Kv) is also critical particularly for understanding differences between laboratory and commercial production-level freeze dryers. It is also useful when studying heat transfer rates derived from glass vials. Conventional techniques for evaluating the sublimation rate and the vial heat transfer coefficient in lyophilization runs employ the gravimetric method which measures the solution weight before and after freeze drying (Hottot et al., 2005). However, the gravimetric method is a complicated operation and needs extra-batches for measuring these quantities. Furthermore, to perform the gravimetric analysis, the primary drying process must be stopped before the end of the primary drying process. Such partial runs do not allow us to evaluate the endpoint of primary drying time, cake appearance, and water content in the same batch.

Therefore, the first step for a careful monitoring of the process is thus to check if product temperature has remained below the threshold value, thus discarding those products whose final quality could have been jeopardized. Besides, the monitoring system has to be able to properly identify the ending point of the primary drying stage, thus avoiding prolonging unnecessarily this stage. The second step is to monitoring the sublimation rate and the vial heat transfer coefficient for better characterize the process. Finally, as process optimization, using a mathematical model of the process, is required to minimize the duration of the drying stages, the monitoring system should be able to provide estimates of model parameters, either in-line or off-line, depending on the type of approach selected [9], [10].

3.1.2 Current Solutions

Various systems were proposed in the past to achieve the previously listed goals: an extensive review of them can be found in [9]. A first group of systems is based on measuring the temperature of the product of individual vials during freeze drying cycle. The next group based on measuring the chamber conditions such as chamber pressure and Tunable Diode Laser Absorption Spectroscopy (TDLAS) which will be discussed below [16]-[18].

Temperature Monitoring Solutions

Product temperature monitoring during a freeze-drying cycle is traditionally performed using a single-point sensor such as thin wire thermocouples and resistance thermal detectors (RTD, PT-1000) in a lab environment. Variations across freeze dryers as well as the spatial distribution of vials inside a given freeze dryer often result in substantial differences in the vialsâ€™ heat transfer coefficients and temperature profiles. While such differences may be tolerable in laboratory-scale experiments, they can cause considerable complications in production-level machines. Therefore, accurate process condition monitoring is becoming increasingly critical in the freeze drying industry. However, the product temperature monitoring of thermocouples is limited because the wired thermocouples operation for temperature mapping (particularity in center position) on shelves is complicated at a production scale freeze dryer. In 2008, an innovative wireless sensor was reported [48] which has great potential PAT tool in a large scale freeze dryer.

A number of commercial temperature solutions are available and are summarized with their features and operating technologies in Table 3.1. Tempris [49], [50] and WTMplus [51] sensors are battery-free but can support up to to 8-16 sensors and only a single temperature measurement per sensor. Ellabs[52] and Madgetech[53] sensors are capable of multipoint measurements but are battery-operated.

Other Solutions

A number of other systems that didn't rely on measuring product temperature are also available. The first kind of such system is based on the pressure rise test: the chamber

Table 3.1. Comparison of Industrial Temperature monitoring systems.

Company	Frequency	Operation	Capabilities
Tempris [49], [50]	2.4 GHz	Quartz shift	8-16 sensors & single point
WTMplus [51]	2.4 GHz	Quartz shift	8-16 sensors & single point
Ellabs [52]	NA	Thermocouples	Logger
MadgeTech [53]	2.4 GHz	RTD	Battery operated
T and D [54]	902-928 MHz	RTD Thermocouple	Battery operated
This work[55]	2.4 GHz	Capacitive	2^{16} sensors

where the product is located is isolated from the vacuum system for a short time interval, and the pressure increases due to water vapor accumulation. A mathematical model is used to calculate the pressure rise, and variables like product temperature, the residual moisture, and the parameters of the model used to simulate the process are retrieved looking for the best fit between the calculated and the measured values of chamber pressure [11]-[15]. The pressure rise test can be used in every freeze-dryer, provided that a fast system for chamber isolation is available. A less invasive system (with respect to product dynamics) is based on TDLAS [16]-[18]. Unfortunately, the use of TDLAS requires an expensive hardware, with a tricky calibration procedure.

Another relevant drawback of TDLAS and of the pressure rise test based systems is that they provide "mean" values of the desired variables, but it is well known that product temperature, as well as the residual amount of water and model parameters, may vary according to the position of the product on the shelf as a consequence of the different heat transfer mechanisms (e.g., the product at the edges of the shelf may be heated also by radiation from chamber walls, "edge vial effects") [19].

3.1.3 Problem Statement

Currently in lyophilization, temperature monitoring is conducted using the systems above have two major drawbacks. First, most of the sensor in those systems only employ one temperature sensing element at the bottom of the product(vial) and are not efficient for

tracking the freezing drying process (freezing and primary drying). Second, most of the system requires an expensive hardware and can only operate a limit number of sensors. Therefore, it is required for efficient temperature monitoring to be wireless and multi-point. In addition, the systems has to be completely battery-free with low power consumption operation and with a small footprint to fit in any vials. Thus, it is required to design a multi-point wireless temperature sensing system that has the following properties:

- The ability to monitor/estimate product temperature,thus evidencing if the threshold value is trespassed.
- The ability to track nucleation and primary drying phase.
- The ability to monitor/estimate the residual amount of ice,thus identifying the ending point of the main drying stage.
- The ability to quickly estimate the sublimation rate and Vial Heat Transfer Coefficient.

3.1.4 Methods

To develop an wireless multi-point temperature sensor with all of the capabilities mentioned above, a noval multi-point temperature sensor system was developed and tested. Furthermore, the performance of the wireless sensor system was evaluated with practically-important solutions based on sucrose and d-Mannitol. These are representative bulking agents constituting different characteristic cakes[56]. Moreover, the abilities of the wireless multi-point sensors was expanded to track the sublimation process and to simultaneously determine the sublimation rate and the vial heat transfer coefficient by utilizing the Multi-point temperature sensing system . In addition, the potential of the wireless multi-point sensors for real-time monitoring, process verification and cycle optimization for pharmaceutical lyophilization in laboratory process development as well as when scaling to pilot or production scale is studied and discussed.

3.2 Sensor Operation Principle

The wireless multi-point temperature sensor system used in this [55] was similar to the system designed by [57], [58] with some functionality upgrades including both sensor hardware design changes as well as software improvements. The tested system consisted of 8 sensors, a PC base station, and an Radio frequency (RF) signal generator (Mini-Circuits®, USA). Figure 3.1 shows the block diagram of the multi-point wireless sensor system.

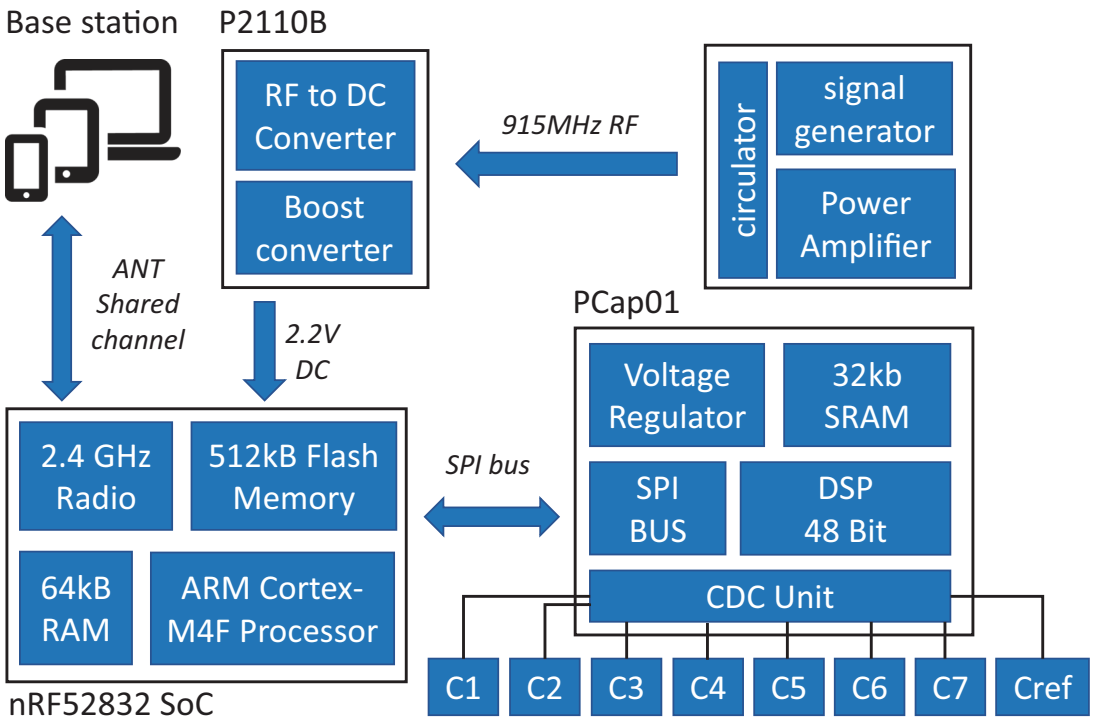

Figure 3.1. Block diagram of the multi-point wireless sensor system.

Each sensor was comprised of three printed circuit boards (PCBs): 1) Capacitive Temperature Sensing probe 2) Micro-controller and Wireless Transceiver Module 3) RF energy harvester module for wireless powering. The sensing probe and PCB with microcontroller was connected by a board-to-board connector and the RF energy harvester was connected via a ribbon cable. This modular design increases the sensor's compatibility with different

sensor probes. The whole sensor assembly occupies a footprint of 10.30 mm x 28.75 mm and the footprint of the RF harvester module was 21.84 mm x 21.72 mm.

3.2.1 Capacitive Temperature Sensing Probe

In order to effectively monitor the product temperature during lyophilization process, a probe with seven temperature sensing elements was designed to capture the temperature profiles at different levels of the product (Figure 3.4A). The sensing elements were the GRM series ceramic chip capacitors with a base capacitance of 1200 pF with U2J dielectric that exhibits a linear temperature coefficient characteristic of -750 ± 120 ppm/K in free space [59]. The capacitive sensors were read using the PCap01 capacitance measurement circuit [60]. PCap01 utilizes an RC discharge measurement circuit (TDC) to measure seven temperature sensing capacitors and one reference capacitor with attofarad (aF) resolution. The measured values were recorded as a ratio of the discharge times of the sense capacitors and a known reference capacitor. For this application, the reference capacitor was chosen to be a 1200 pF, NP0-dielectric-based capacitor, which has a temperature coefficient of $\pm$ 30ppm/K. The recorded values were read via a serial interface to the micro-controller.

Each of the sensing probes was encapsulated with 15 micrometer parylene-C coating to electrically insulate and protect it from cryogenic shocks (Figure 3.4). A layer of sliver Radio-frequency interference (RFI) shield coating [61] was also applied to the sensor probe to protect the sensor from RF interference . The sensors were the individually calibrated using thin wire thermocouples (36-gauge, Omega, Newport, CT, USA) in an environmental chamber from 20^oC to -55^oC. Figure 3.2 shows the measured capacitance versus temperature for each of the sensing elements in air indicating each of the elements has a predictable monotonic response. The general temperature-capacitance relationship is given by:

$$T = A \times {C_x}^2 - B \times C_x + D \tag{3.1}$$

where C_x is the capacitance of each of the sensing elements in picoFarad (pF), and T represents temperature in Celsius (^oC). The coefficients (A,B and D) of sensing elements #1 are shown in Figure 3.2 and the other elements can be extracted in a similar fashion.

The calibration equations were stored in the micro-controller for direct transmission of the temperature to the base station.

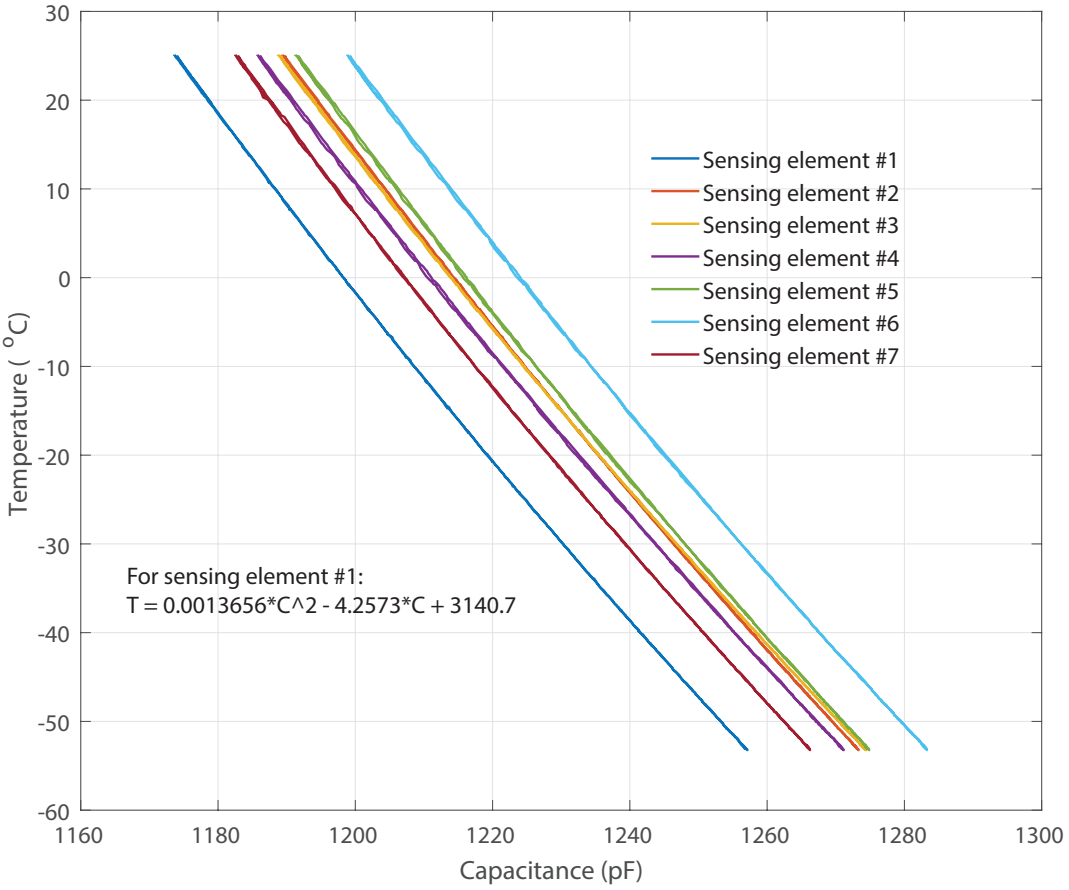

Figure 3.2. Measured capacitance versus temperature for each of the sensing elements where sensing elements 1-7 represent the capacitive sensing elements shown in Figure 3.4A.

3.2.2 Micro-controller and Wireless Transceiver Module

Similar to previous work, the nRF52832 system on chip [62] was employed to process and transmit the measurements from PCap01. It features a very low power 32-bit ARM Cortex-M4F processor with a built-in-radio that operates in the 2.4 GHz ISM band which can output up to +4dBm power and 512kB flash storage for data-logging when the sensor is disconnected from the network. The ANT wireless communication protocol was used

for communication between sensors and the base station. ANT is an ultra low power RF protocol implementing short range (20-30 feet in free space) and low data rate (up to 1 Mb/s). For this application, the bi-directional ANT shared channel topology was used with the capability to connect 60 leaf-nodes (sensors) with one tree- node (base station).

3.2.3 RF Energy Harvester

An RF to DC to energy harvester was used to ensure a battery free operation. The energy harvester device used is the P2110B [63] interfaced with a 915 MHz surface-mount technology (SMT) antenna. The device harvests 915 MHz RF energy and stores it in a external capacitor. In this system, an 85-mF super-capacitor with low discharge current and low equivalent series resistance (ESR) of 80 Ω was used [64]. The capacitor's compact size ($20 \times 18 \times 1$ mm^3) also made it an ideal selection for this application. The harvester outputs a user-defined voltage on the output pin once the capacitor charging threshold has been reached. The output voltage is maintained until the voltage falls below the internally set low-voltage threshold for the capacitor. The system operates down to -15 dBm of input power with an output current of 50 mA with 55% RF to DC conversion efficiency.

3.2.4 Base Station

For this application, a custom PC application (Figure 3.3) was developed in C# with .NET framework which works with an external ANT radio USB stick. The application automatically adds available devices to the channels and outputs the received data to local storage. It also features the real-time graphing of the received data. Since ANT is not natively supported by PC, a custom USB stick with an 8-channel ANT Connectivity integrated circuit (IC) (nRF24AP2-USB) was used to enable the ANT communication.

3.3 Experimental Setup & Post Processing

3.3.1 Freeze Drying Experiment Setup

Freeze-drying was performed in a laboratory-scale freeze-dryer (REVO, Millrock Technology, Kingston, NY [65]) equipped with a vacuum capacitance manometer and pirani gauge

pressure sensor located at Purdue university. A 915 MHz monopole antenna was mounted on the side of the chamber for wirelessly powering the sensor. In addition, to prevent leaks and protect the coaxial cable from vacuum during freeze drying, a custom vacuum feed-through SMA connector was used to pass the RF coaxial cable inside the chamber to power the antenna. The computer with 2.4 GHz ANT connectivity USB stick for sensor operation and data collection was placed next to the freeze-dryer.

Five freeze drying runs were performed to evaluate the sensors' measurement accuracy, sublimation tracking ability, determination of sublimation rate and the heat transfer coefficient(K_v) (Table 3.2). Pre-defined freeze drying recipes were used in all of the five runs based on each product's properties in 6R SCHOTT® pharmaceutical vials with 4ml fill volume loaded on one entire shelf (360 vials). D-mannitol and sucrose were purchased from Sigma (Sigma Chemical Company, Germany) and used as received with ultra pure water. One of the runs (cycle 1) in partial completion was performed with ultra pure water for measuring the vial heat transfer coefficient (K_v) of the REVO lyophilizer. Two of the runs (cycle 2 and 3) were performed using 5% w/v sucrose solution and two additional runs (cycle 4 and 5) were performed using 3% w/v mannitol solution. In each experiments, 8 wireless sensors were placed across the entire shelf for a complete shelf mapping. In addition, eight 36-gauge wire thermocouples were placed in the vials adjacent to vials containing wireless multi-points sensor for comparison. Each wireless multi-point sensor was placed in the center position touching the bottom of the vial. Similarly, the thin wire thermocouples were in the "center bottom" position to ensure adequate comparison of the temperature profiles between sensing elements of the wireless sensor and the thermocouple. Furthermore, during the freezing step of all four experiments, controlled nucleation (performed with Millrock FreezeBooster® at -5^oC) was applied to reduce batch to batch as well as vial to vial variabilities.

3.3.2 Sublimation Tracking and End-point Detection

Previous studies suggest that for most vials, the primary drying during the freezing process is a top-down process with a well-defined sublimation front moving through the product as it dries and to a lower degree, from the side to the center of the vial [66]. Above the ice surface interface is dried product (commonly known as "cake"), below the interface

Table 3.2. List of all freeze-drying experiments.

Cycle ID	Description	Goal	Recipe	K_v (cal/s/K/cm^2)
1	pure water run	to estimate k_v	Table 3.3	3.4±0.68E^{-4}
2	5% w/v sucrose (100% dried run)	the main run for studying the wireless sensor's ID capability	Table 3.5	3.3 E^{-4}
3	5% w/v sucrose (50% dried run)	to estimate the sublimation rate gravimetrically	Table 3.5*	N/A
4	3% w/v mannitol (100% dried run)	complementary study for the sublimation tracking	Table 3.4	3.7 E^{-4}
5	3% w/v mannitol (50% dried run)	to estimate the sublimation rate gravimetrically	Table 3.4**	N/A

*:with 9 hours primary drying time
**:with 5 hours primary drying time

Table 3.3. Freeze drying recipe used for pure water.

	1	2	3	4	5	6	7	8
Freezing step								
Shelf setpoint [^{o}C]	20	20	5	5	-5	-5	-45	-45
Time [min]	0	10	0	90	30	90	180	120
Primary drying								
Shelf setpoint [^{o}C]	-45	-10	-50	-50				
Time [min]	15	180	0	9999				
Vaccum setpoint [mTorr]	60	60	60	60				

is frozen product with ice crystals still remaining to be sublimed [67]. As the primary drying process progresses, the different sensing elements on the sensing probe will start to lose contact with ice as the sublimation front moves from top to bottom, resulting in a sharp increases in slope in the temperature profile [68], [69]. End-point of the primary drying can be detected when the temperature at every sensing points converges together and the rate of temperature change was below 0.5^{o}C/h.

Table 3.4. Freeze drying recipe used for 3% w/v mannitol solution.

	1	2	3	4	5	6	7	8
Freezing step								
Shelf setpoint [^{o}C]	20	20	5	5	-5	-5	-45	-45
Time [min]	0	10	0	90	30	90	180	120
Primary drying								
Shelf setpoint [^{o}C]	-45	20	20					
Time [min]	5	60	1800					
Vaccum setpoint [mTorr]	60	60	60					

Table 3.5. Freeze drying recipe used for 5% w/v sucrose solution.

	1	2	3	4	5	6	7	8
Freezing step								
Shelf setpoint [^{o}C]	20	20	5	5	-5	-5	-45	-45
Time [min]	0	10	0	90	30	90	180	120
Primary/ Secondary drying								
Shelf setpoint [^{o}C]	-45	-10	-10	45	10			
Time [min]	15	60	2400	720				
Vaccum setpoint [mTorr]	60	60	60	75				

3.3.3 Rapid Determination of Sublimation Rate

The sublimation rate is the most important factor for understanding the drying process and the quality of the freeze drying product. Since the major driving force for ice sublimation is the difference in ice vapor pressure between the product and the condenser, the ice sublimation rate can be influenced by product temperature and chamber pressure[70]. Traditionally the sublimation rate was measured gravimetrically [71], [72] by repeatedly weighting vials before and after the freeze drying process or using tunable diode laser absorption spectroscopy (TDLAS) in the laboratory scale [73]. This is an added cost to the production run since additional batch for gravimetric testing is required. However, since the wireless multi-point sensor is capable of tracking the sublimation front and measuring drying time up to each sensing element location in the product, the entire primary process can be decomposed into the consecutive drying of each "layer of frozen product (of 3.26 mm in thickness, Figure 3.4A)" between different sensing elements. Then the sublimation rate could be calculated based on the drying time and theoretical weight loss of ice in each layer

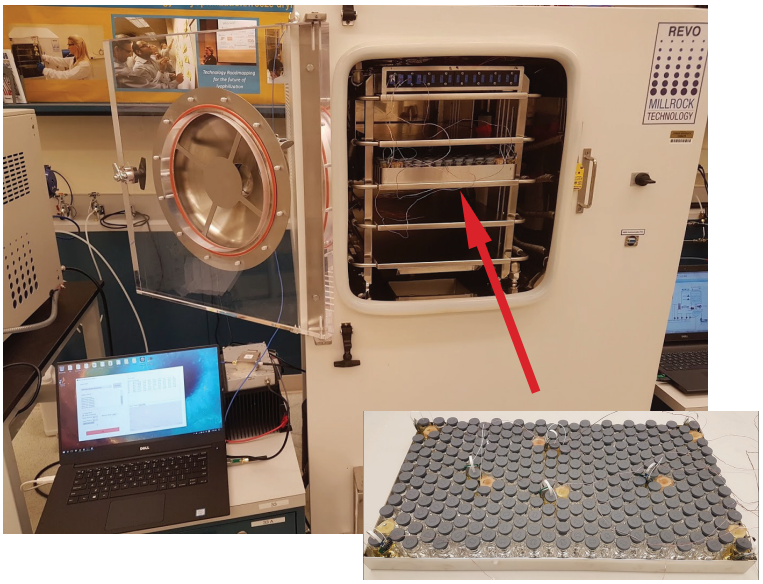

Figure 3.3. Typical arrangement of the vials with sensors and thermocouples in the tray and into the freeze dryer.

of the product. The theoretical weight loss can be calculated based on the inner area of the vial and distance between the sensing elements as described in equation 3.2:

$$\frac{dm}{dt} = \frac{A_p \cdot \Delta h_{sensor} \cdot \rho_{\text{ice}} \cdot \varepsilon}{t_{drying}} \tag{3.2}$$

where A_p is the cross sectional area of the product, Δh_{sensor} is the distance between sensing elements and t_{drying} is the drying time between sensing elements and $\varepsilon = (1 - C_{solid\%})$ is the porosity of the cake. Table 3.6 shows the calculated sublimation rate for each drying layer between the sensing elements of the product during the sucrose experiment.

Table 3.6. Comparison between sublimation rate measured by multi-point wireless sensor (sen) and gravimetric method (grav) for the center and edge vials (g/h).

	Center (Sucrose)		Edge (Sucrose)		Center (Mannitol)	
Location	sen	grav	sen	grav	sen	grav
Top-Mid to Middle	0.17	0.16	0.21	0.22	0.33	0.39
Middle to Cross	0.18	*N/A*	0.19	*N/A*	0.40	*N/A*
Cross to Bottom	0.14	*N/A*	0.20	*N/A*	0.30	*N/A*

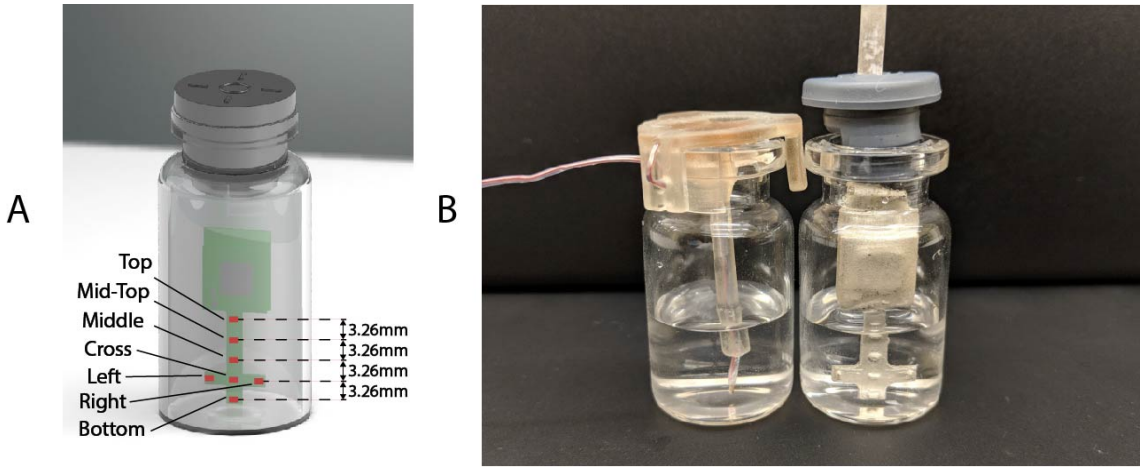

Figure 3.4. (A) Representation of the wireless multi-point sensor. Seven sensing elements are labeled. (B) Placement of Wireless multi-point sensor and thermocouple in the vial.

3.3.4 Rapid Determination of Vial Heat Transfer Coefficient

Vial heat transfer coefficient (K_v) describes the relationship between heat flow and temperature difference during primary drying and needs experimental measurements [71]. There are three major contributions to K_v: direct conduction from the shelf to the vial bottom, conduction through the vapor between the vial bottom and the shelf, and radiative heat transfer. Consequently, heat transfer coefficient will vary from vial to vial for a same batch and it is a crucial parameter to monitor for successful freeze drying. Traditionally, a separate trial run is required to evaluate the K_v for commercial production. However, with the ability to measure the sublimation rate during primary drying, the multi-point wireless sensor is also capable of estimating the heat transfer coefficient (K_v) using the following equation:

$$K_v = \frac{dm}{dt} \cdot \frac{\Delta H_{sub}}{< T_{shelf} - T_b > \cdot A_v} \tag{3.3}$$

where $\frac{dm}{dt}$ is the calculated sublimation rate between two sensing points, "<...>" denotes an average over the primary drying phase, ΔH_{sub} is the latent heat of sublimation for water and A_v is the the cross-sectional vial area.

3.4 Results and Conclusion

3.4.1 Compatibility Study of the Multi-point Wireless Sensor and Thermocouple

Figure 3.5 illustrates the temperature histories during an entire freeze drying process for a 5% w/v sucrose solution, monitored by one wireless multi-point sensor placed in a representative center vial and one 36-gauge thermocouple placed in an adjacent vial. The shelf temperature was measured by using a built-in thermocouple that was previously installed into the freeze dryer. Five out of seven temperature profiles measured by wireless multi-point sensor are color coded from red to blue lines shown in Figure 3.5 representing sensing elements from top to bottom. All seven sensing elements showed good agreements with the adjacent thermocouple during the freezing step with a maximum temperature difference observed before nucleation (right before 4h) of 1 ^{o}C. After the freezing step, at around 10 hours, primary drying started with the ramp up of the shelf temperature to -10 ^{o}C. At the end of the primary drying step, the temperature profiles measured by the wireless multi-point sensor and the thermocouple are in good agreement and reach a steady state temperature at the same time at around 45 hours. In addition, it is worth mentioning that the temperature reading from the bottom sensing elements of the multi-point wireless sensor showed the best agreement with the thermocouple placed in the bottom center in the adjacent vial during steady state for the entire process since they were both placed in the bottom center of the neighboring vials (assuming identical product resistance, R_p, due to controlled nucleation). Similarly, a more aggressive freeze drying experiment with 3% w/v mannitol solution was conducted as well, and the results supported the same conclusions. This result suggests that the multi-point wireless sensor is capable of measuring reliable and accurate temperature.

3.4.2 Sublimation Tracking and End-point Detection

Figure 3.5 and 3.8 show respectively the complete temperature profile of the experiment with 5% w/v sucrose solution (cycle 2) for center and edge vials containing multi-point wireless sensors. It can be seen that drying proceeded from top to bottom as each sensing element's temperature profile "departed" from the "bottom temperature" in the same order.

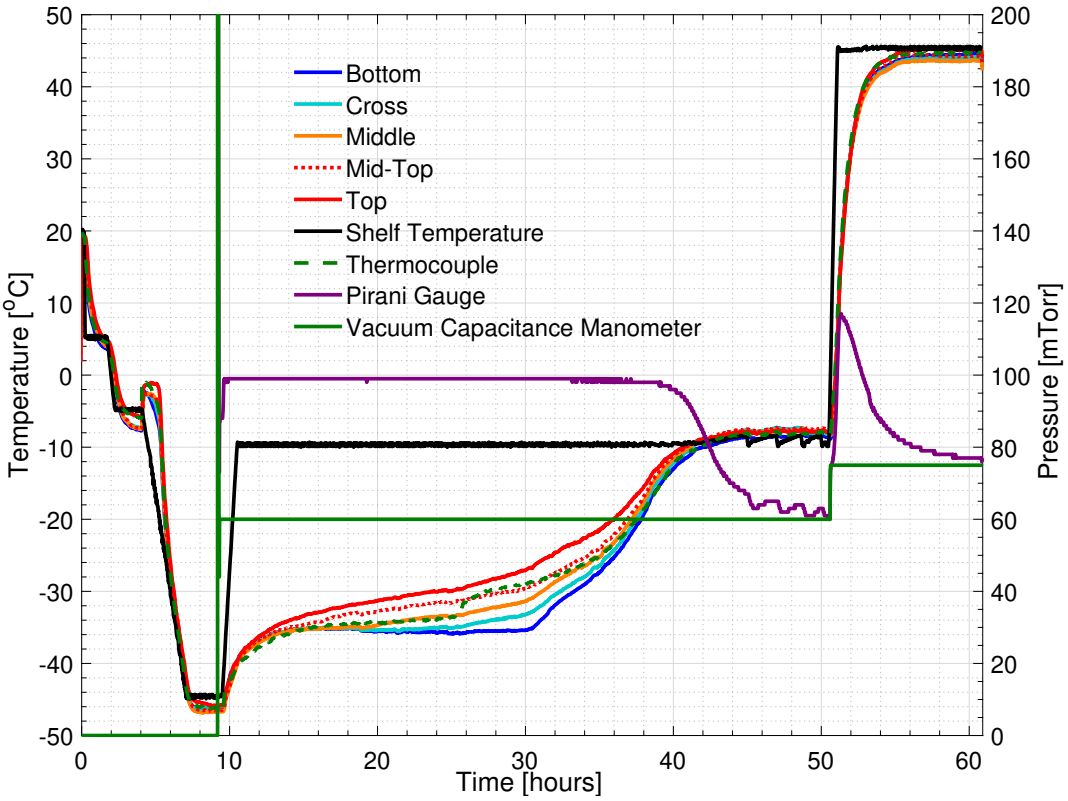

Figure 3.5. Measured temperature and pressure over time profile of 5% w/v sucrose solution for a center vial.

As seen from Figure 3.6, a zoom-in figure showing the primary drying step of the center vial during the experiment mentioned above, the sublimation front was clearly tracked as each sensing elements lost contact with ice crystals. Therefore, the drying time at the mid-top, middle, cross and bottom positions in the vial during primary drying could be determined by the wireless sensor based on the temperature profile measured at different positions. Specifically, a change in temperature rising rate is identified with the slope of tangent dashed line for each sensor location as shown in the figure. The "anchor point (colored circles)" of a tangent line on the bottom location temperature profile is identified as the end of partial drying for each layer. For the center vial shown in Figure 3.6, the drying time from the start of primary drying to each layer were shown in Table 3.7. Similarly, the measured drying time for the sensor placed in the edge vial during the same run were also shown in Table 3.7. In addition, the end-point of the primary drying were detected at 43

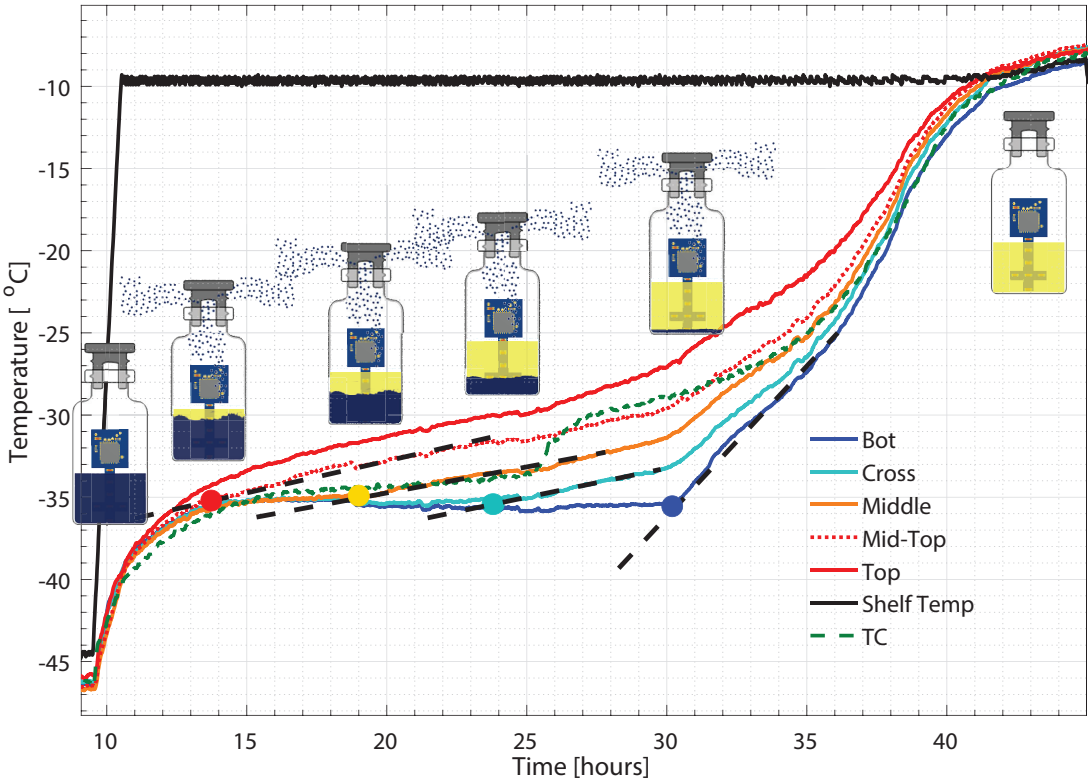

Figure 3.6. Zoomed-in figure for primary drying phase of Figure 3.5, where each colored circle indicates the crossing point for the sublimation front with corresponding sensing point and the dashed line represents the change of slope.

and 34 hours for center and edge vials respectively, also in excellent agreement with the adjacent thermocouples. Furthermore, the end-point of primary drying for the center vial agrees well with the onset of convergence of the capacitance manometer and Pirani gauge pressure sensors indicating that the center vial was the last to finish the primary drying. In addition, a heat and mass transfer simulation of the primary drying in a vial with the same experimental parameters was conducted [74]. Specifically, K_v was obtained from the gravimetric study of cycle 1. The product resistance, R_p as a function of the cake length is computed from temperature history of the bottom sensing element in cycle 2 .This is then fitting to the standard empirical form [75] of:

$$Rp(L_{ck}) = R_0 + \frac{A_1 \cdot L_{ck}}{1 + A_2 \cdot L_{ck}} (\text{cm}^2\text{-Torr-hr/g}) \tag{3.4}$$

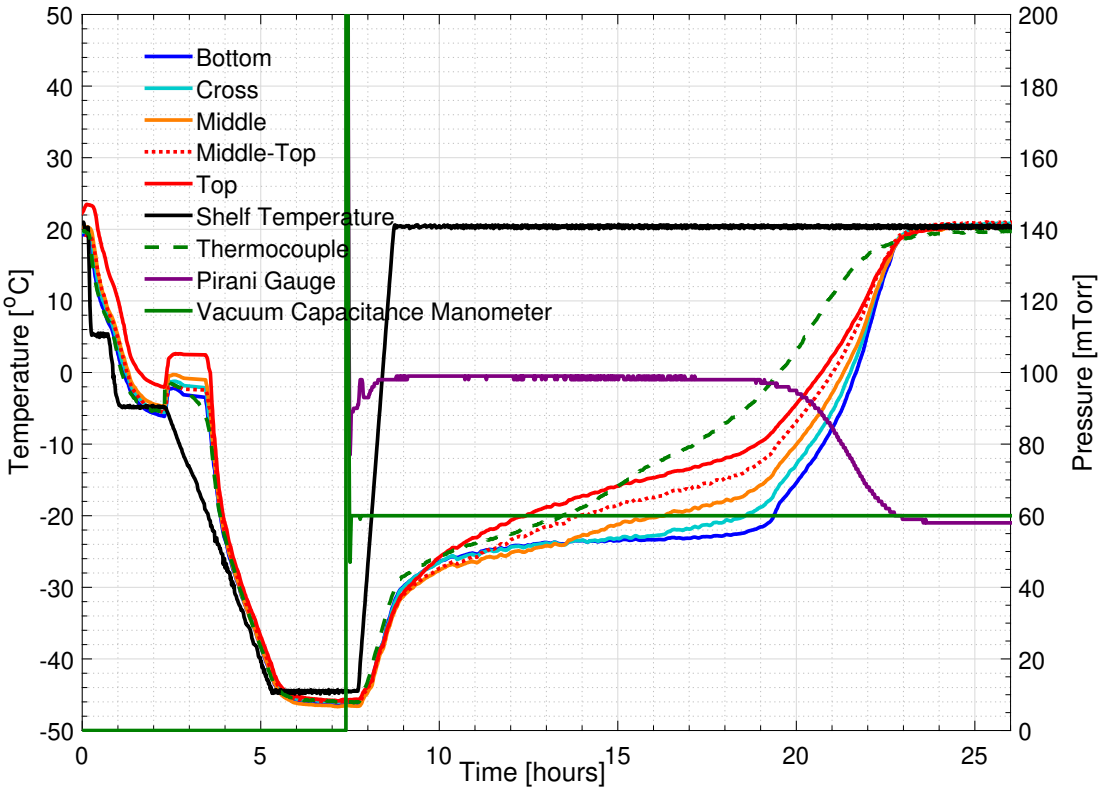

Figure 3.7. Measured temperature and pressure over time profile of 3% w/v mannitol solution.

where $R_0 = 0$, $A_1 = 71.55$ (cm-Torr-hr/g), $A_2 = 34.1$ (cm^{-1}) are fitting coefficients found for the best curve fit. L_{ck} (cm) is the cake length. Finally, these parameters are used to model the temperature at all the locations of the sensing elements for cycle 2. Table 3.8 shows the comparison between experimental and simulated results for the drying time between each layer of the center vial. The results showed excellent agreement between the experimental and simulated results.

3.4.3 Rapid Determination of Sublimation Rate

As previously discussed in Section 2.4, the sublimation rate can be determined based on the drying time between each layer. The multi-point wireless sensor is capable of measuring in real-time the sublimation rate at various positions during the freeze-drying cycle. For

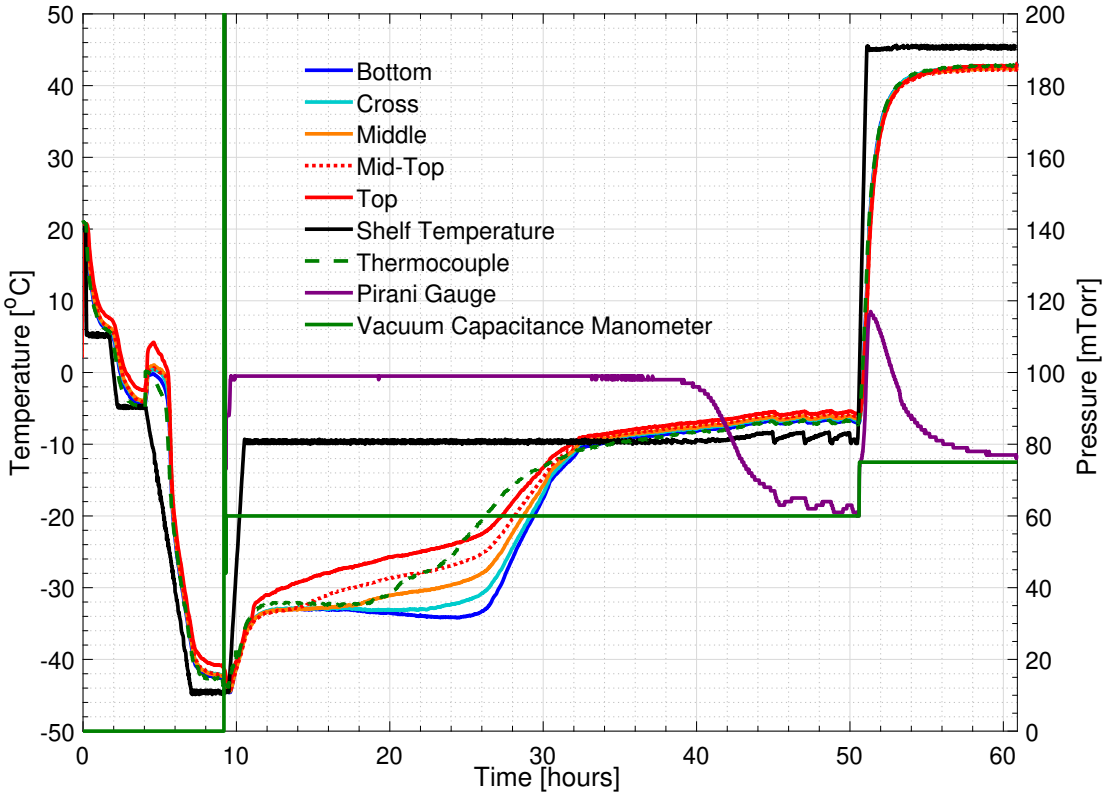

Figure 3.8. Measured temperature and pressure over time profile of 5% w/v sucrose solution for an edge vial.

example, the sublimation rates for the center vial between mid-top to middle sensing point in cycle 2 can be calculated as follows:

$$\frac{dm}{dt} = \frac{3.14\,\text{cm}^2 \cdot 0.326\,\text{cm} \cdot 0.918\,\text{g/cm}^3 \cdot 95\%}{5.4\,\text{h}} = 0.17\,\text{g/h} \tag{3.5}$$

Similarly, the sublimation rates at the same location in cycle 4 (3%w/v mannitol) can be calculated as follow:

$$\frac{dm}{dt} = \frac{3.14\,\text{cm}^2 \cdot 0.326\,\text{cm} \cdot 0.918\,\text{g/cm}^3 \cdot 97\%}{2.8\,\text{h}} = 0.33\,\text{g/h} \tag{3.6}$$

Table 3.6 shows the complete measured sublimation rates for cycle 2 and 4 using the multi-point wireless sensor. In order to verify this approach of rapid determination of the sublimation rate, two additional experiments with identical process and product setting (only

Table 3.7. Primary drying time measured by multi-point wireless sensor.

Location	Center (cycle 2)		Edge (cycle 2)		Center (cycle 4)	
	Drying time (h)	between layers (h)	Drying time (h)	between layers (h)	Drying time (h)	between layers (h)
Middle-Top	3.9	N/A	3.5	N/A	3.3	N/A
Middle	9.3	5.4	7.7	4.2	6.1	2.8
Cross	14.2	4.9	12.5	4.8	8.4	2.3
Bottom	21	6.8	17	4.5	11.4	3.0

Table 3.8. Comparison between experimental and simulation primary drying time for cycle 2.

Sensor Location	Experimental results (h)	Simulation results (h)	Difference (%)
Middle-Top	0	0	N/A
Middle	5.4	5.1	4.8
Cross	10.3	10.3	-0.1
Bottom	17.1	15.2	11.1

the primary drying time is 50% shorter for valid gravimetric study) were performed (cycle 3 and 5) using the gravimetric method. Each vial with the muli-point wireless sensor was weighted before and after the drying. Table 3.6 shows the comparison between sublimation rates ($\frac{dm}{dt}$) calculated using the muli-point wireless sensor and gravimetric method. Comparing the initial stages of the primary drying with the prior completed drying run shows close agreement in the average sublimation rate for both typical formulation excipients (crystalline mannitol and amorphous sucrose), which suggests that the multi-point wireless sensor has great potential for rapidly determinating the sublimation rate. It is noted that the sublimation rate from the sensor is an average quantity over the drying time in each layer. However, it is sufficiently accurate since heat and mass transfer modeling results suggest that the sublimation rate changes relatively slowly during primary drying (with the only exception in the initial fast ramping stage). This additional real-time process monitoring technique may become instrumental in optimizing the freeze drying process on both laboratory- and production-scale machines.

3.4.4 Rapid Determination of Vial Heat Transfer Coefficient

With the demonstrated capability to determine the sublimation rate using the sensor in the previous section, this work proceed further by combining it with the temperature data to estimate the vial heat transfer coefficient without the need of any gravimetric study. The following wireless sensor measurements over the course of drying from the "Mid-top" to "Middle" sensing element locations from (cycle 2) can be used to estimate the heat transfer coefficient at the center position as follows:

$$\frac{dm}{dt} = 0.17\ \text{g/h} \tag{3.7}$$

$$< T_{sh} - T_{T_b} >= \ ((-10\,^o\text{C}) - (-35.1\,^o\text{C})) = 25.1\,^o\text{C} \tag{3.8}$$

$$K_v = \frac{0.165\ \text{g/h}}{3600\ \text{s}} \cdot \frac{676\ \text{cal/g}}{25.1\ \text{K} \cdot 3.8\ \text{cm}^2} = 3.3 \cdot\ 10^{-4}\text{cal/s/K/cm}^2 \tag{3.9}$$

Similarly, for the heat transfer coefficient at the center position from the full shelf 3% w/v mannitol solution run (cycle 4):

$$\frac{dm}{dt} = 0.33\ \text{g/h} \tag{3.10}$$

$$< T_{sh} - T_b >= \ ((20\,^o\text{C}) - (-24\,^o\text{C})) = 44\,^o\text{C} \tag{3.11}$$

$$K_v = \frac{0.33\ \text{g/h}}{3600\ \text{s}} \cdot \frac{676\ \text{cal/g}}{44\ \text{K} \cdot 3.8\ \text{cm}^2} = 3.7\ \cdot 10^{-4}\text{cal/s/K/cm}^2 \tag{3.12}$$

Compared to the actual K_v = (3.4±0.68) E^{-4} cal/s/K/cm^2 previously measured from the center of the freeze drying experiment with ultra pure water. These estimations fall in the range of the actual K_v considering the cycle to cycle variation. A higher K_v measured in cycle 4 might have been caused by the higher shelf temperature during primary drying with a non-linear increase of the radiative heat transfer component. Table 3.2 shows the comparison between the estimated K_v by the wireless sensor (cycle 2 and 4) and the actual K_v at the center position of the batch. Combined with the results from the determination of the sublimation rate, the wireless multi-point sensor has great potential for continuous process verification, with the ability to optimize the process parameters for every batch. This is crucial especially in production scale, since additional batchs for gravimetric analysis

are often required, increasing production cost. In some GMP facilities, gravimetric study of the heat transfer coefficient is unfeasible mostly due to the operational cost and the current sensor opens up an opportunity to have an estimation of k_v along with a normal product run.

3.5 Conclusion

The measured profile of product temperatures using the new multi-point wireless sensor during freeze-drying of manntiol and sucrose solutions showed excellent agreement with thermocouple as well as the simulated data. The sublimation progress during primary drying was clearly tracked by the multi-point wireless sensor. The sublimation rate extracted from the wireless multi-point sensors' measurement also showed good match with the actual grametric measurements. Furthermore, the vial heat transfer coefficient (K_v) calculated from the measured sublimation rate by the multi-point wireless sensor was in excellent agreement with the actual gravimetrically measured vial heat transfer coefficient. In addition, the ability of multi-point sensing endows the wireless sensor with a more elaborate characterization of the freeze drying profile as demonstrated through the $end-point\ detection$ and the $sublimation\ front\ tracking$. These results suggested the wireless multi-point temperature sensor system has a potential for real-time monitoring, process verification and cycle optimization for pharmaceutical lyophilization in laboratory process development and GMP production.

4. VIRTUAL THERMOCOUPLE: A NON-INVASIVE TEMPERATURE MEASUREMENT APPROACH FOR CONTROLLED LYOPHILIZATION

4.1 Introduction

As discussed in chapter 3, a careful monitoring of the product temperature is required to check if product temperature has violates the threshold value, thus discarding those products whose final quality could have been jeopardized. Moreover, variations across freeze dryers as well as the spatial distribution of vials inside a given freeze dryer often result in substantial differences in the vials heat transfer coefficients and temperature profiles. While such differences may be tolerable in laboratory-scale experiments, they can cause considerable complications in production-level machines. Therefore, accurate process condition monitoring is becoming increasingly critical in the freeze drying industry.

Traditionally, the best practice to measure product temperature in freeze-drying is by inserting miniature fine-gauge thermocouples (TCs) inside the solution to be freeze-dried[76]. However, this technique presents several problems. First of all, TCs inserted inside the vial may modify the behavior of the monitored vial during drying, since the thermal distribution inside the product is altered by the high thermal conductivity of the metallic wires with respect to glass; secondly, TCs in direct contact with the drying material act as a nucleation site, thus altering the

Besides thermocouples, other techniques have been proposed in the literature or the market, for monitoring the product temperature of individual vials during the freeze drying process. For example, a non-invasive temperature monitoring with thin-film thermocouples (TFTCs) approach was proposed by Oddone et al. [77], that measures vial temperature with TFTCs printed on the outside of the vials. However, their approach didn't address two crucial problems: first of all, the measured temperature of their approach is the vial wall temperature on the outside, with does not represent the actual temperature of the product. Second, TFTCs still replies on the wired thermocouples to operates, which still oppose potential heating to the vial wall, which may alter the drying process. Another fully wireless solution was proposed by Jiang et al.[55] that unitizes low-power sensing electron-

ics to measure the product temperature, solves the problem of TCs heating, and measures product temperature directly still poses a potential risk that the invasive sensor that may modify the freeze-drying behavior. Another approach to understanding the freeze-drying is thought numerical modeling. Ravnik et al. proposed a numerical model for the simulation of a lyophilization process in a vial[78] and show a good matching with lyophilization dynamic with experimental results. However, such modeling is highly dependents on pre-calibration/tuning of parameters(e.g. heat transfer coefficient(k_v)) that are different from vials to vials with multiple experimental runs. Thus, while such an approach might work with lab-scale-sized experiments with only a few vials, it's not suitable for larger-scale experiments with hundreds or even thousands of vials.

This chapter presents a new technology that provides non-invasive and fully wireless methods of measuring the vial and product temperature during the freeze drying process, overcoming some of the limiting factors of the methods previously described. This technology consists of three parts: 1)the flexible non-invasive multi-point sensing probe that is attached to the vials externally, the low-power wireless electronics that read and transmits the data wirelessly, and the numerical model that translate the temperature profile measured from the vial wall to the product temperature. In addition, experimental results are provided to show that the proposedmethods can effectively be used for monitoring the drying dynamics and product temperature during freeze-drying process in real-time and non-invasively.

4.2 Methods

The non-invasive wireless process tracking system was designed to monitor a freeze-drying process across the entire chamber with minimum invasion to the actual product by monitoring the product temperature at various locations, therefore tracking the sublimation front of the Lyophilization process. The non-invasive monitoring is enabled by attaching the flexible temperature sensing probe to the side of the vial.

4.2.1 Flexible Sensing Probe Design

In order to extract information concerning the temperature of product during the lyophilization process, a flexible multi-point sensing probe was designed and fabricated using photosensitive lithography patterning and chemical etching.

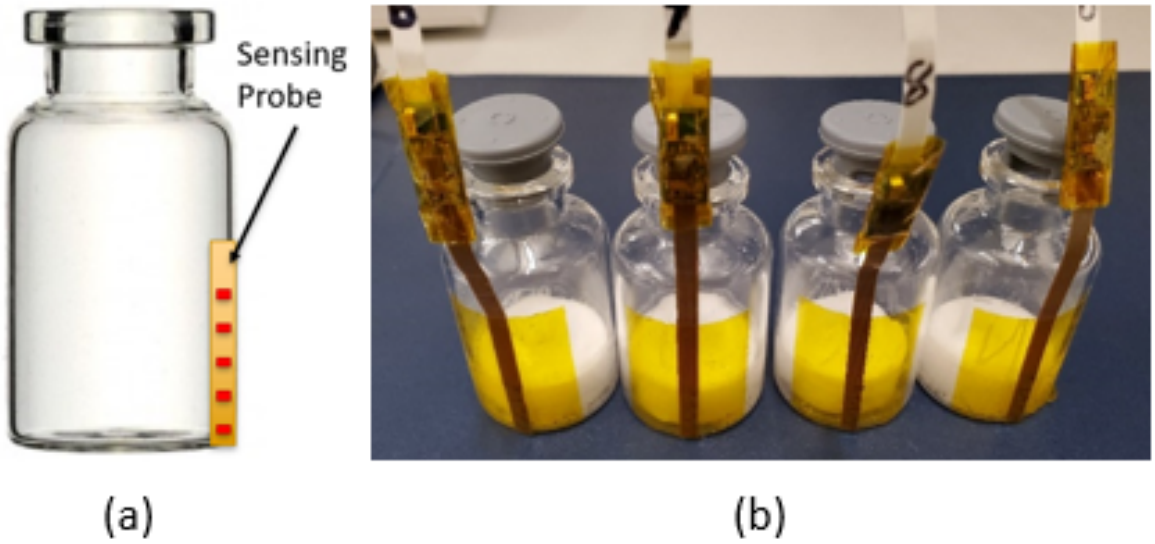

Figure 4.1. Prototype of the flexible temperature multi-point sensor

Figure 4.1 shows the concept of the proposed sensor and the manufactured sensor mounted on the test vial respectively. While sputtered thermocouples on vial walls have been explored by Parvis et al. [79], they require modifications of the vial structure through a fairly complex manufacturing method. The proposed flexible sensor is produced using established large-scale manufacturing methods for common electronic components. Furthermore, it will not require any vial modifications providing the ability of multiple time use and also it can be fitted to different vial size. In addition, multiple NTC (Negative temperature coefficient) thermistor were mounted to the flexible substrate allows measuring temperature at different heights of the cake within the vial. Taking into consideration the end use of the sensor in relation to the vial dimensions one can revision the design accordingly.

Figures 4.2 show the proposed fabrication process of creating the flexible temperature sensor. Sensors are fabricated on copper Kapton laminate Pyralux AP8555R by DuPont us-

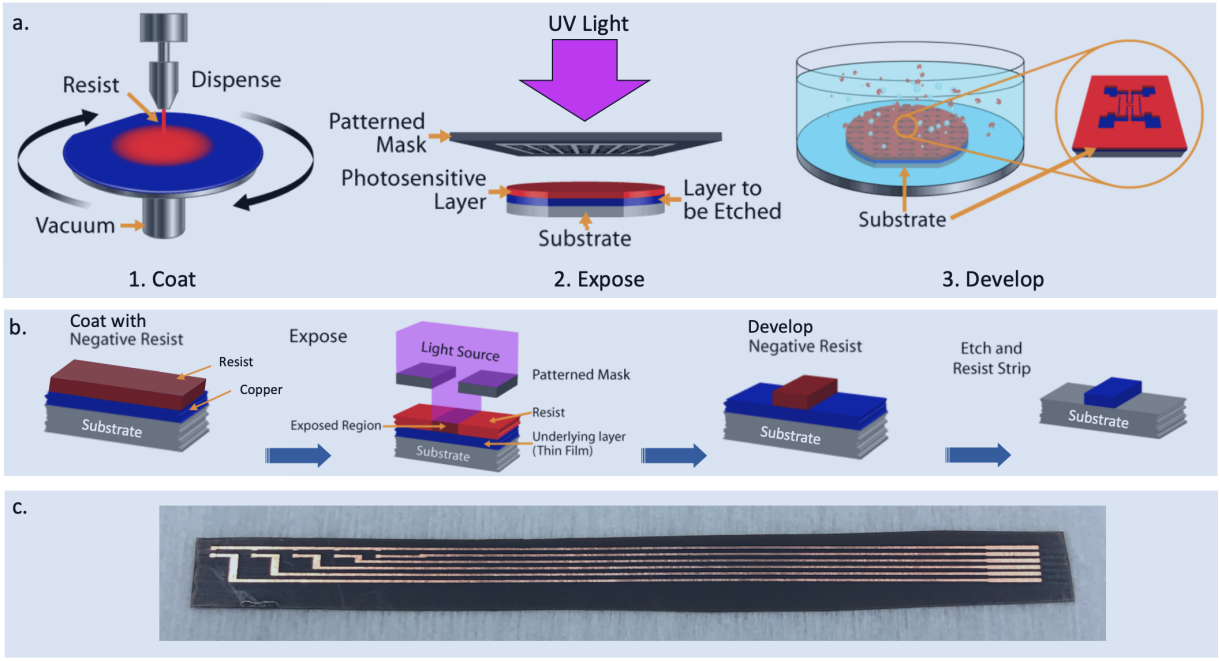

Figure 4.2. Fabrication process of the flexible Kapton sensing probe.

ing photosensitive lithography patterning microfabrication processes. The flexible dielectric substrate has a thickness of 0.127 mm with a copper thickness of 0.018 mm. The manufactured assembly could be transferred on the outside or inside of the vial depending on the application as shown in Figure 4.1.

Photosensitive lithography is a process used in the micro-fabrication of silicon semiconductor components to transfer desired patterns on a thin film or the bulk of a substrate (also called a wafer). It uses UV light source to transfer a geometric pattern from a photomask (also called an optical mask) to a photosensitive material (that is, light-sensitive) photoresist on the substrate. Negative dry film photoresist TentMaster TM200i Series by DuPont hot rolled was used on the flexible substrate and exposed it to 14 mW/cm2 of UV light through a photomask using MA6 Karl Suss equipment. Chemical etching refers to the process of chemically removing excess copper exposed (not masked with photoresist) to the liquid chemical bath. Copper etchant CE-100 by Transene was used to form the desired copper traces at the end of the manufacturing step shown in Figure 4.2(b).

4.2.2 Temperature Sensing Element

NTC thermistors are used to determine the temperature with small footprint (0.4 x 0.2mm). It is made of the combination of metal oxides which passed through the sintering process which gives inverse electrical resistance versus temperature (R/T) relationship to it. Due to the large inverse relationship a small temperature change can causes a huge change in electrical resistance which is excellent fit for measuring lyophilization since the majority of the process is in the lower temperature range.

Thermistors have the advantage of very high sensitivity to temperature changes, but the disadvantage of an aggressively nonlinear characteristic. Each thermistor has to be calibrated to ensure measurement accuracy. Steinhart-Hart(S-H) Equation the most commonly used model to describe the nonlinear characteristic of the thermistor:

$$\frac{1}{T} = A + B * ln(R) + C * (ln(R))^3 \tag{4.1}$$

where T is the temperature in degrees Kelvin, Ln(R) is the Natural Log of the measured resistance of the thermistor, A, B, and C are constants.

To obtain the value of A, B, and C, each thermistor is measured at 20^oC, 0^oC, -40^oC separately. Then, fit the coefficients of a third-order polynomial in the log-resistance values to best match the inverse-temperature values.

4.2.3 Low-power Wireless Sensing Electronics

Similar to previous work[55], [80], [81], the nRF52832 system on chip from Nordic semiconductor[62] was employed to process and transmit the measurement via 2.4 GHz radio**ant**. The sensing electronics were powered by P2110B RF harvester from Powercast[82] which stores the harvested RF energy into a super capacitor. The sensing functionality was achieved by utilizing the built-in 12-bit successive approximation analog-to-digital converter(SAADC). Figure 4.4 shows the block diagram of the low power wireless sensing electronics. Temperature sensing thermistors were connected with a 97k Ω load resistor. Each voltage dividing circuits are independent for each thermistor and are independently powered by General-purpose input/output (GPIOs) pins from micro-controller to save power. The

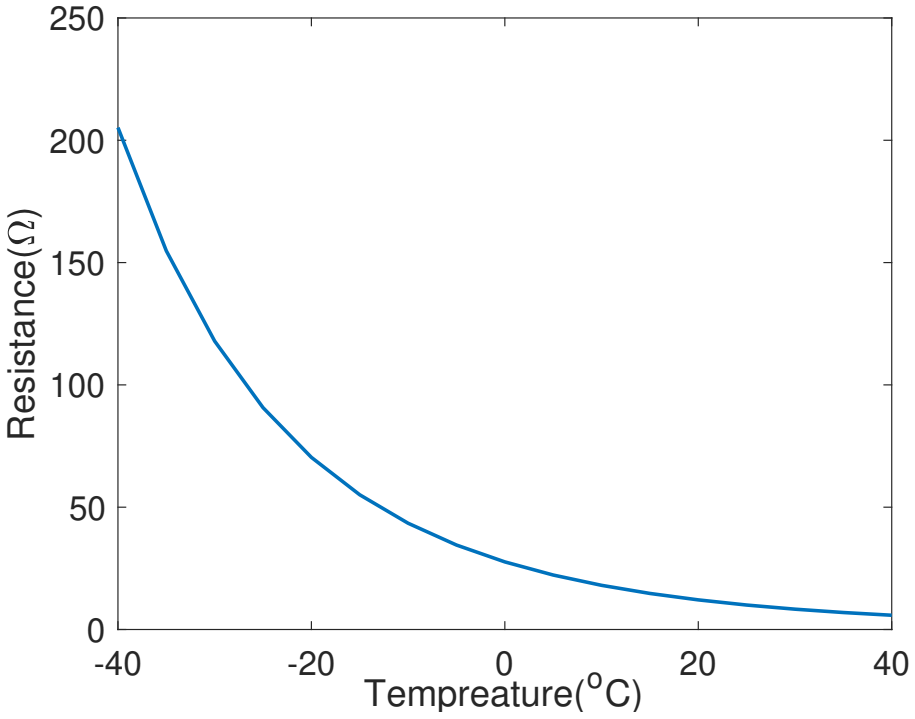

Figure 4.3. Resistance response vs temperature of 10K NTC thermocouple.

bridge voltage from each voltage dividing circuits then connected to an 8-to-1 multiplexer, a pre-gain amplifier, and then measured by the built-in 12-bits ADC (0.6 V reference voltage). During operation, the micro-controller dynamically adjusting the pre-gain amplifier for each temperature sensor to counter the aggressively nonlinear characteristic of the thermistor, so the voltage input won't overflow and achieve the optimal sensing resolution.

4.2.4 Modeling and Physical Simulation

In order to understand the temperature profile measured by the multi-point temperature sensor, the numerical model was created for the primary drying stage of the solution in a vial using COMSOL multiphysics[83]. The model allows to obtain temperature distribution on the vial surface as well as inside the vial (product temperature). The simulation results were compared with the actual measurement for more insights into the process.

The transient heat and mass transfer during primary drying of the product in a glass vial is performed and numerically investigated. The variation of product and vial temperature as

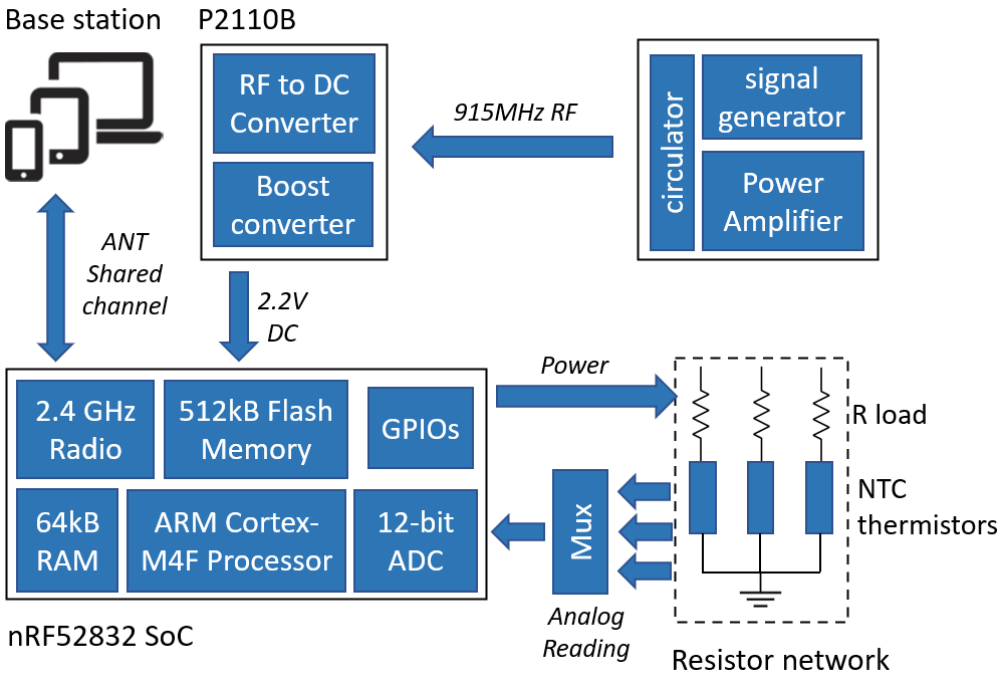

Figure 4.4. Block diagram of the Wireless Sensing electronics.

well as the position of the sublimation front is predicted. The geometry and the boundary conditions are axisymmetric and the model is solved in 2D. For numerical purposes, the product in a vial filled with frozen mannitol 5% solution is split into frozen zone (96% of total volume) and the dried zone (4% of total volume).

Several heat transfer mechanisms are involved in the simulation: convective heat fluxes from ambient, heat exchange between vial, dried/frozen product, and shelf. The system of equation encompasses the heat transfer equations for porous and media in dried and frozen domains. The vapor convection is also taken into account in the dried region. The temperature at the sublimation interface is given by the saturation vapor pressure (Clausius-Clapeyron equation):

$$T_S = \frac{2.19 \times 10^{-3}}{28.89 - ln(p)} \tag{4.2}$$

The Stefan condition is applied to get interface velocity:

$$v_S = \frac{Q_S}{\epsilon \rho_{\text{ice}} L_S} \tag{4.3}$$

Where Q_S is the normal heat flux jump at the interface. It is evaluated using Lagrange multiplier with enabled weak constraints.

Darcy's law is used to calculate the vapor pressure and velocity in the porous domain. Material properties for vapor flow in the dried domain are assumed to be constant and the chamber pressure is set at the top of the vial. The transient analysis with the deformed geometry interface is then used to track the ice surface inside the vial (Figure 4.5). Coupled mass and heat balances on the moving mesh are computed.

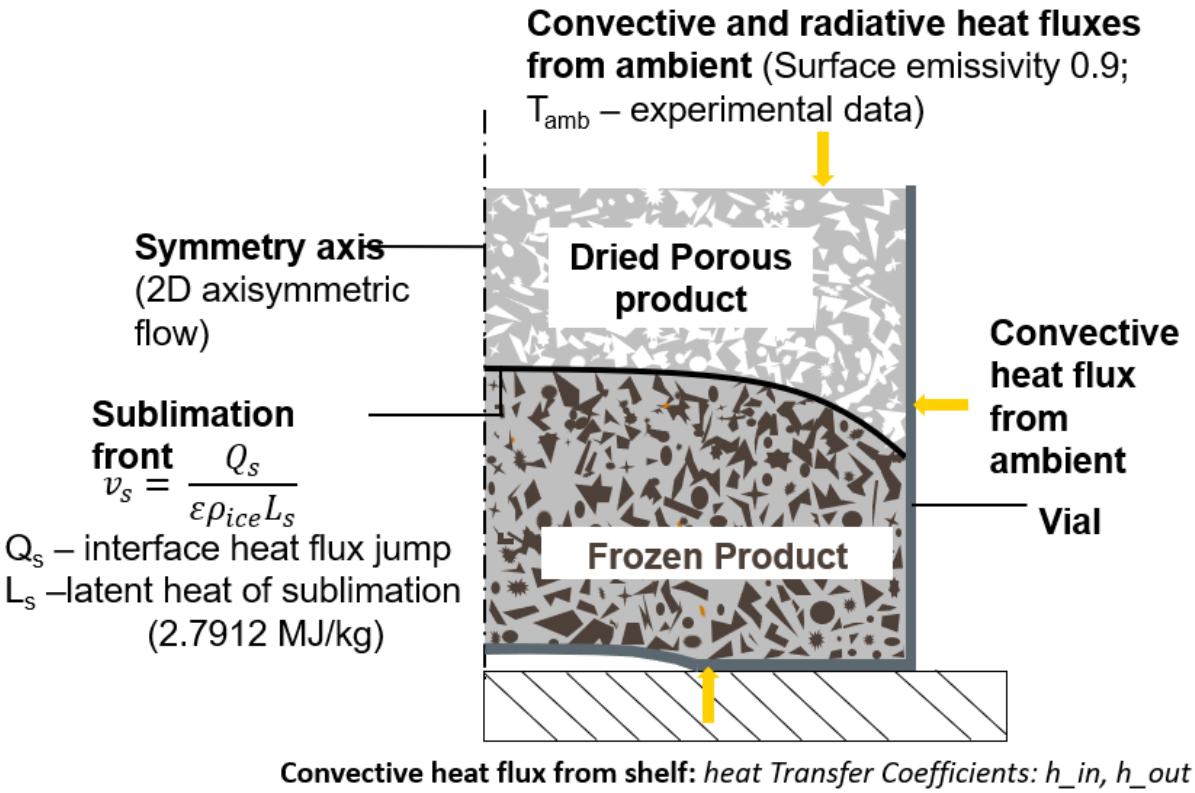

Figure 4.5. Heat transfer mechanisms in a vial.

4.2.5 Experiment Setup

Freeze-drying was performed in a laboratory-scale freeze-dryer (REVO, Millrock Technology, Kingston, NY [65]) equipped with a vacuum capacitance manometer and pirani gauge pressure sensor located at LyoHub center at Purdue University. A 915 MHz monopole antenna was mounted on the side of the chamber for wirelessly powering the sensor. In ad-

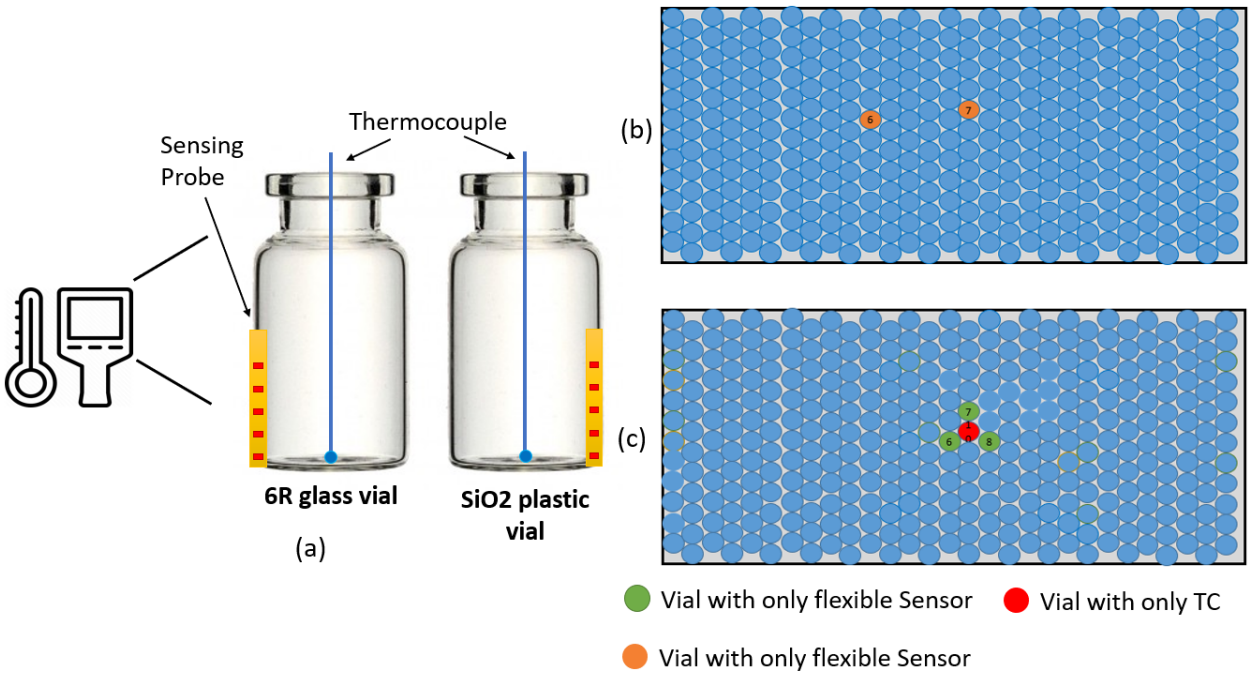

Figure 4.6. Experiment setups. (a) two isolated vial(glass and plastic) with a thermal camera (b) 2 center vial equipped with virtual thermocouple that were placed in the center of a full tray. (c) experimental set-up for testing the thermocouple heating.

dition, to prevent leaks and protect the coaxial cable from the vacuum during freeze drying, a custom vacuum feed-through SMA connector was used to pass the RF coaxial cable inside the chamber to power the antenna. The computer with 2.4 GHz ANT connectivity USB stick for sensor operation and data collection was placed next to the freeze dryer.

Three sets of freeze drying experiments with different vial placements were preformed to evaluate the flexible temperature sensor performance and repeated several times to provide reliable data. Pre-defined freeze drying recipes(table 4.1) were used in all of the three runs in 6R SCHOTT ® pharmaceutical vials with 4 ml fill with D-mannitol solution(Sigma Chemical Company, Germany). Type T thermocouples from Omega were used to measure the shelf temperature, air temperature, and product temperatures for all three experiments.

Figure 4.6(a) shows the setup for 1st sets of experiments with two individual vials made from different material(glass and plastic), in order to evaluate the performance of the multi-point flexible temperature sensing probe and the ability to monitoring of the freeze-drying

process.Two vials with different materials(6R glass vial and plastic vial (SiO2)) were used. Thermocouples were inserted into both vials at the bottom-center location to measure the product temperature. A Thermal IR camera(FLIR Lepton® 3.5) was used to monitor the freezing behavior of the product.

Figure 4.6(b) and (c) show the vial placements for the 2nd and 3rd set of experiments, where a full shelf(400 vials) loads of vials were used. For the 2nd experiments, two vial that were equipped with the virtual thermocouples were evenly placed in the center of the tray. TCs were inserted into the vial and touching the bottom center to measure product temperature. The purpose of the 2nd experiment was to evaluate the performance of the proposed virtual thermocouple. For the 3rd experiment, four vials equipped with the virtual thermocouples were placed next to each other in the center of the tray. Unlike the previous experiments, only the center vial (red vial in Figure 4.6(c)) were inserted with TCs. The purpose of the 3rd experiment was to evaluate the TCs heating effects with the help of the proposed virtual thermocouple.

Table 4.1. Freeze drying recipe used for 5% w/v mannitol solution.

	1	2	3	4
Freezing step				
Shelf setpoint [^{o}C]	20	20	-45	-45
Time [min]	0	10	180	120
Primary drying				
Shelf setpoint [^{o}C]	-45	20	20	
Time [min]	5	60	1800	
Vaccum setpoint [mTorr]	60	60	60	

4.3 Results

4.3.1 Monitoring of Freezing Behavior

Figures 4.7, 4.8 show the temperature profile measured by the flexible temperature probe during the freezing stage as well as thermal camera images for the glass and the plastic vials during the 1st sets of experiments(figure 4.6(a)). A clear difference in the captured nucleation event between glass and plastic vials were observed. Thermal image #1 shows the moment

where the nucleation event about to happen, the bottom sensor reads the lowest temperature while the top sensor shows the highest. This is to be expected since the bottom sensor was placed right at the bottom of the vial and was closest to the shelf. As can be seen in figure 4.7 and 4.8, uncontrolled nucleation started right after #1 and resulted in a sharp rise in temperature (#2), which were captured by the thermal camera for both vials. However, due to the different thermal conductivity between glass and plastic, the temperature profile captured by the flexible sensor was different. All sensors quickly raised to -2^oC, just a little below the product temperature for the glass vial, where sensors on plastic vials read much lower temperature(up to -5^oC) in comparison. However, the temperature profile measured on the glass vial shows a big difference right after the peak caused by the nucleation. As you can see on point #4 of the glass vial, both sensors and TC show that the vial is cooled from the bottom, and gradually expands the top of the product. On the contrary, such a cooling profile was not observed on the plastic vial, as showed by both flexible sensors and TC, as the product freezes uniformly across the product. These results show that the proposed flexible sensors effectively measure the freezing dynamics even with vial made with different materials.

4.3.2 Monitoring of Primary Drying

Multi-physics Simulation

The primary drying stage was modeled and compared with actual experimental data (the flexible temperature sensing probes and thermocouples readings). A full shelf of 6R vials (403 units) are filled with 4ml 5% Mannitol solution is freeze-dried in REVO Millrock lyophilizer. The chamber pressure was set to 70 $mTorr$ and shelf temperature to 20^oC.

Figure 4.11 shows the mesh propagation with respect to time. The porous and solid domains are meshed with a structured mapped grid while the vial domain is meshed with an unstructured grid. The simulation starts with a uniform initial temperature of 228K for vial and product and then the front advances downwards. The automatic re-meshing of the whole geometry occurs when cells' distortion reaches a certain level. The sublimation stops when the front touches the bottom of the vial after 15.7hr. During the primary drying

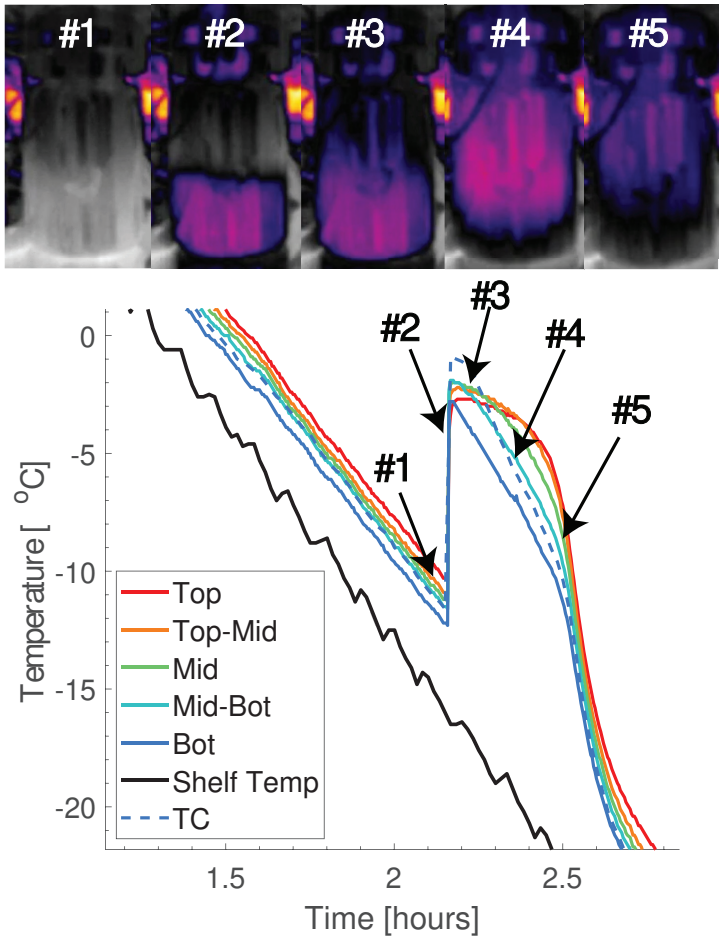

Figure 4.7. Temperature profile measured by the flexible temperature probe during freezing stage and thermal camera images for the glass vial during freezing.

process, the vial heats the product making the front convex. The product and the vial temperature increases as the simulation advances due to several heat transfer mechanisms including convective heat flux from ambient and shelf.

Non-invasive Multipoint Temperature Sensor

Figure 4.9 illustrates the temperature over time profiles of vial #7 during primary drying for a 5% w/v mannitol solution, monitored by two non-invasive multi-points temperature sensor and two 36 gauge thermocouple placed in the same vials respectively. Also, process data including shelf temperature, air temperature, Pirani/ capacitance manometer pressure

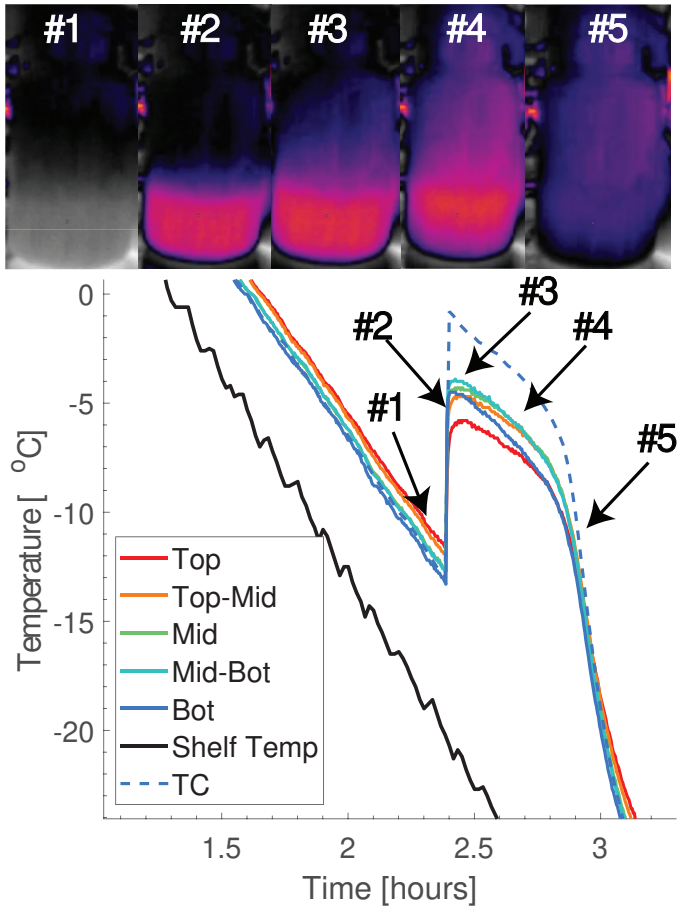

Figure 4.8. Temperature profile measured by the flexible temperature probe during freezing stage and thermal camera shots for the SiO2 vial during freezing.

measurement were recorded. As shown in figure 4.1(a) each flexible sensing probe employs 5 temperature sensors with the bottom sensor mounted at the bottom of the vial wall. During this run, pre-defined freeze drying recipes(table 3.4) were used with primary drying set at 20 ^oC and 70$mtorr$. At the beginning of the primary drying, shelf temperature rises from -45^oC to ^oC results in a sharp increase in vial temperature, as observed in both the sensor and thermocouple reading. At the beginning, of primary drying (after 8 hours in figure 4.9), as the product temperature raises, the bottom sensor shows the highest reading and the top sensor shows the lowest. As the primary drying continues and the sublimation front progresses, this trend starts the reverse and the top sensor starts to overpass the top-mid, mid, mid-bot, and bottom sensor. As shown in figure 4.9 is clearly captured by multi-points

temperature sensor. The endpoint of primary drying can be determined based on the Pirani pressure and capacitance manometer pressure measurements[84]. The primary drying ends as the Pirani measurements start to getting closes to capacitance manometer measurement. Both thermocouples and multi-Points temperature sensors identified the endpoint of primary drying at identical time marks. All temperature sensing points on the flexible probes showed very good agreement in the temperature over time profile with the data obtained from the thermocouples. It is interesting to note that both multi-points temperature sensors indicated an early increase in temperature at the end of primary drying relative to thermocouple data.

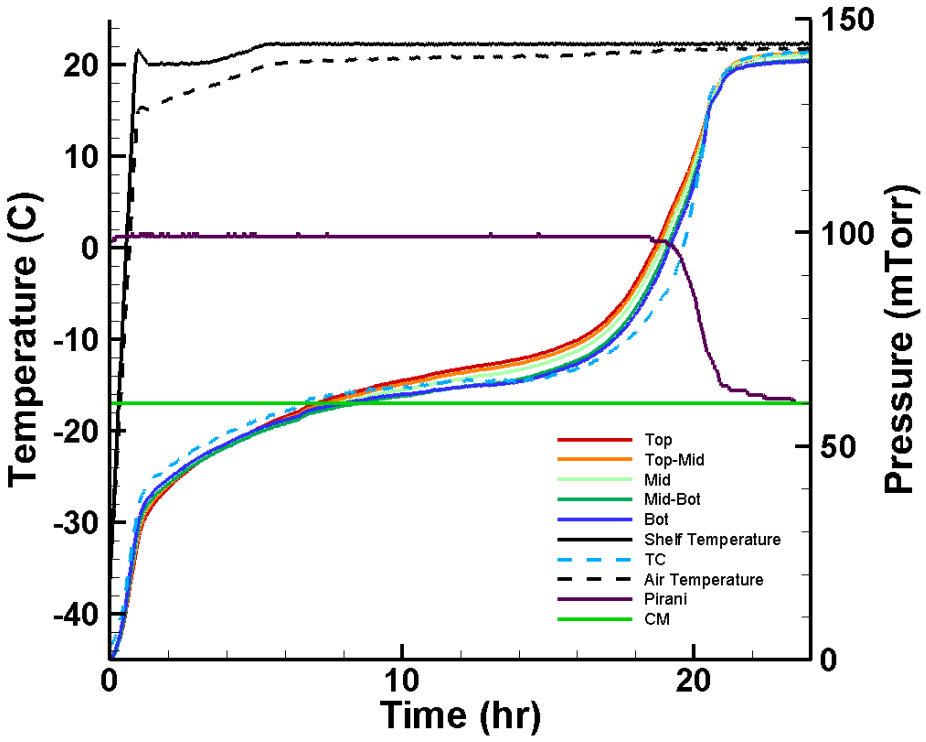

Figure 4.9. Temperature time history profiles for Vial # 7 as well as Pirani and CM pressure measurements.

Virtual Thermocouple and the Tuning Process.

The performance of the virtual thermocouples was validated using data from the performed freeze-drying experiments as mentioned in previous sections. In order to obtain the

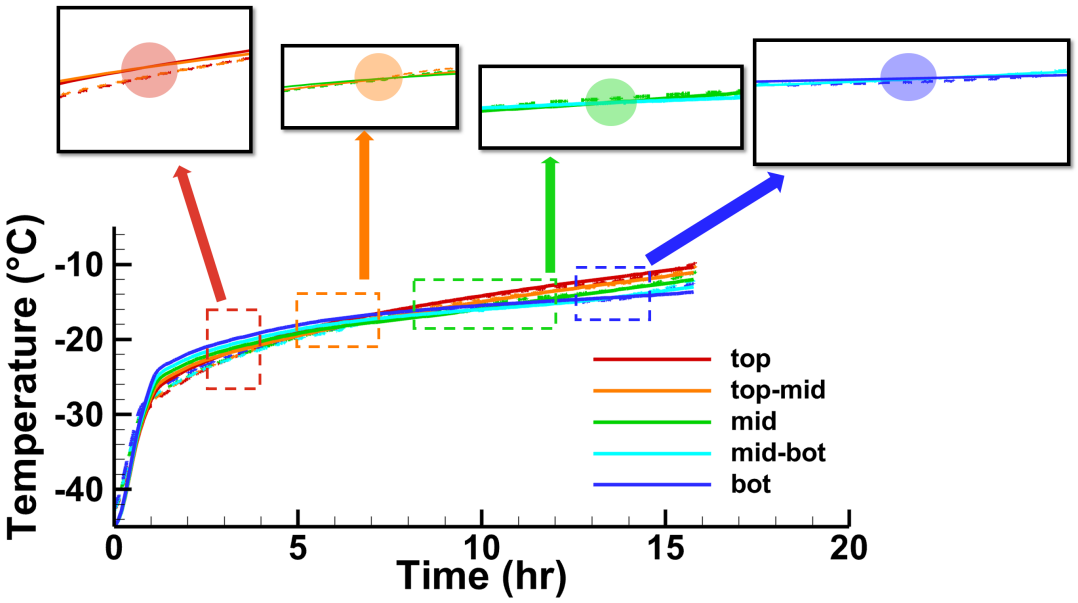

Figure 4.10. Temperature time history profiles measured by sensors (solid) vs simulation data (dashed) with separation points indicated.Vial # 7.

product temperature inside the vial, the simulation model (showcased in figure 4.11) was tuned to match the multi-point sensor data shown in figure 4.9. To simplify the tuning process, input parameters were divided into three groups: the first group is the fixed simulation parameters (table 4.2). These are parameters that are not subject to change from run to run for the same product (such as glass vial properties, material properties (i.e. vial glass) and ice/vapor characteristics). The 2nd group are the process simulation parameters (table 4.3), these parameters are the real process data including shelf/air temperatures(measured with build-in thermocouples) and chamber pressure(measured with capacitance manometer) which are directly imported into the model. The last group are the tuned process parameters(4.3), these are the parameters that are different from vial to vials, they are tuned to match the model output with the actual sensor data. The vapor viscosity was calculated according to Alexeenko et al. [85] where the experimentally measured [86]–[89] values as well as the data from International Association for the Properties of Water and Steam Formulation [90] for water vapor viscosity in the range of -23^oC to 227 ^oC. The power law curve fit is based on Variable Hard Sphere (VHS) molecular model with an effective diameter of 5.78 *angstrom*:

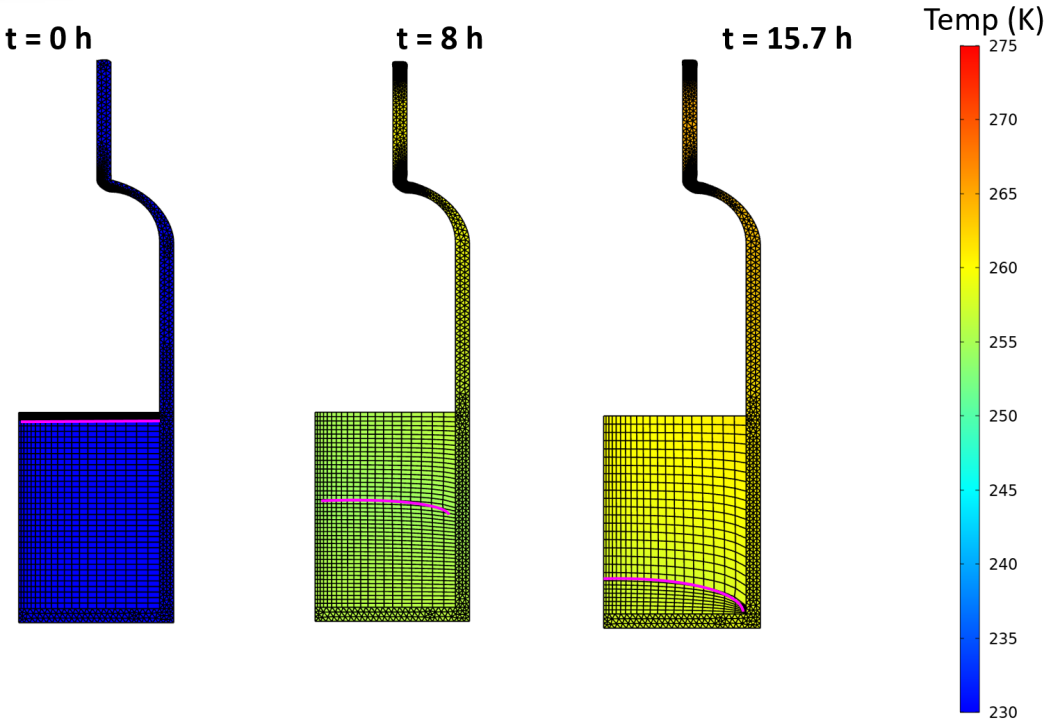

Figure 4.11. Mesh propagation in time.

$$\mu = 8.9007 \times 10^{-6} \left(\frac{T}{273.15} \right) [Pa \times s] \tag{4.4}$$

The solid lines in figure 4.10 show the temperature profile measured by the non-invasive temperature probe. The simulation is performed for two vials: vial # 7 and vial # 10 as indicated in figure 4.6(b). Both vials are surrounded by 6 other vials and can be considered as center vials. In both cases, the simulation is within 1^o of the experiment. The experimental readings of the air temperature in the vicinity of the vial as well as actual shelf temperature are used in the simulation. Figure 4.10 shows the sensors' measurements versus the simulation results for vial #10. Also, the separation points are indicated above the plot in black frames. Each separation point corresponds to the front position crossing the sensor at a particular moment of time. For example, the left picture in a frame shows the moment when the front passes the top-mid sensor. The intersection point of two plots is highlighted for the simulation curves and experimental curves. Similarly, other intersections are highlighted

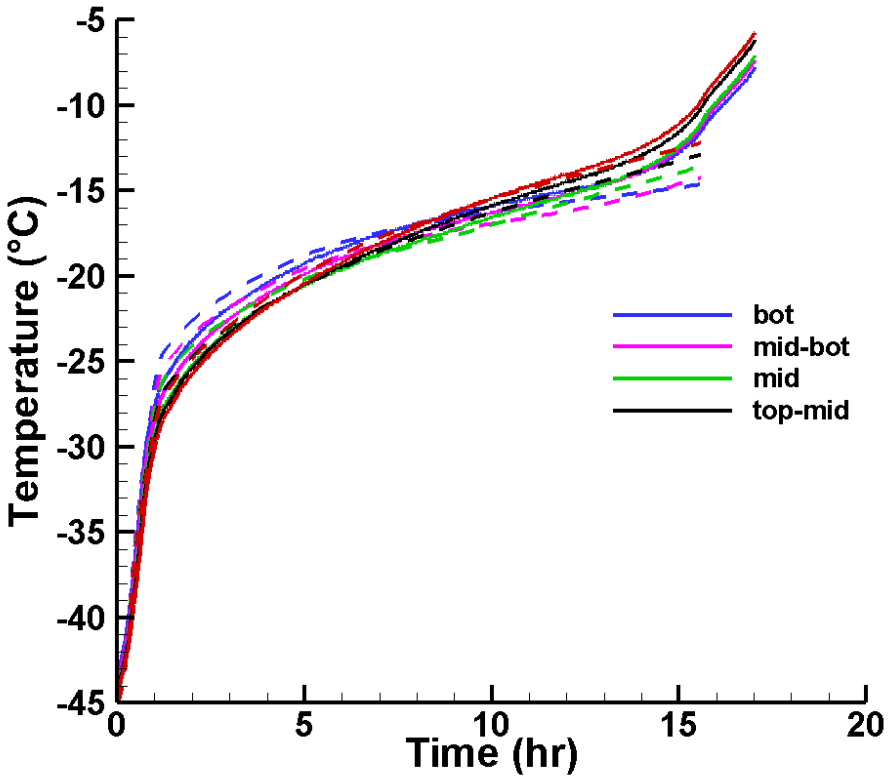

Figure 4.12. Temperature time history profiles measured by sensors (solid) vs simulation data (dashed) for vial # 10.

(top-mid/mid, mid/mid-bot, mid-bot/bot) and indicate the position of the sublimation front. The close agreement between the simulation and modeling is demonstrated.

Figure 4.13, demonstrate the temperature profile that the simulation outputs at the position of the thermocouple(in the center of the vial bottom) after the model is tuned to match the non-invasive multi-point sensor data of vial #10. With the heat transfer coefficients tuned to: 8 and 11 $W/m^2/K$ for the center and the edge of the vial bottom correspondingly. Also, 0.2 $W/m^2/K$ heat transfer was applied to the top part of the vial above the product to model the heat exchange with the ambient. The sensors experimental temperature readings and simulations results are shown for both vials in Figures 4.14,4.12. The simulation (dashed lines) are within 2 ^oC from the experimental data during the whole period of primary drying. The deviations close to the end of primary drying are due to

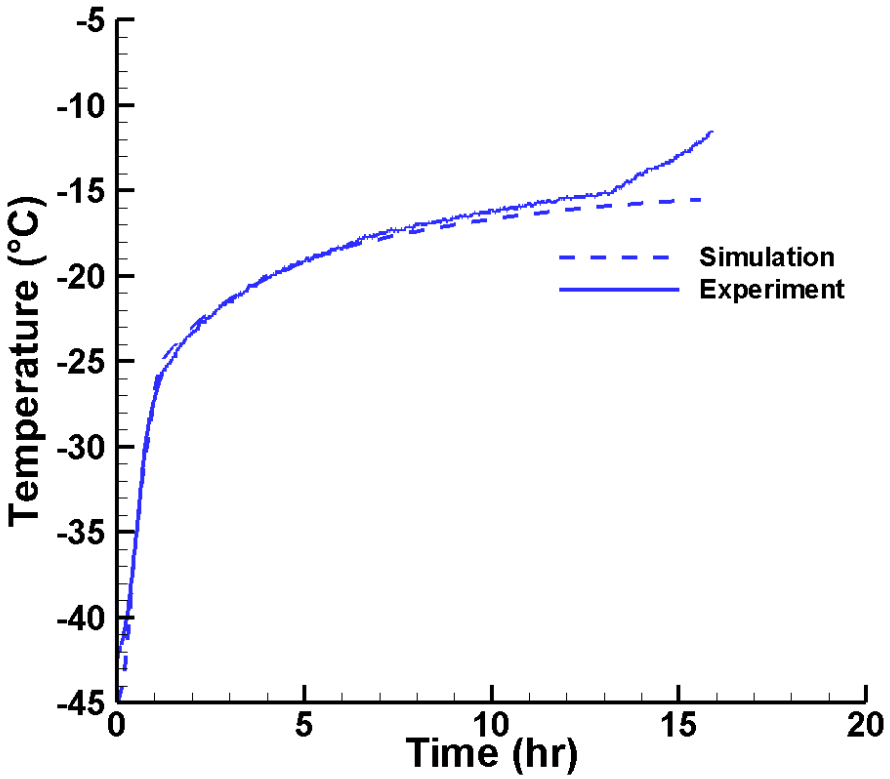

Figure 4.13. Temperature time history measured by thermocouple (solid) vs simulation data (dashed) for vial # 10.

the artificial criteria of the end of the process in simulation. The process is over when the minimum distance between the freezing front and the vial bottom is close to zero. Thus, when the edge of the front reaches the bottom the simulation stops. As shown in figure 4.13, the simulation generated product temperature data shows a great agreement with the actual thermocouple placed at the same location in the same vial. The same tuning process was done to vial #7 as well, figure 4.15 shows the simulation generated product temperature with thermocouple measurement. The heat transfer coefficients equal to 8 and 11 $W/m^2/K$ were set for the center and the edge of the vial's #7 bottom. These proves that virtual thermocouple can measure product temperature accurately and non-invasively.

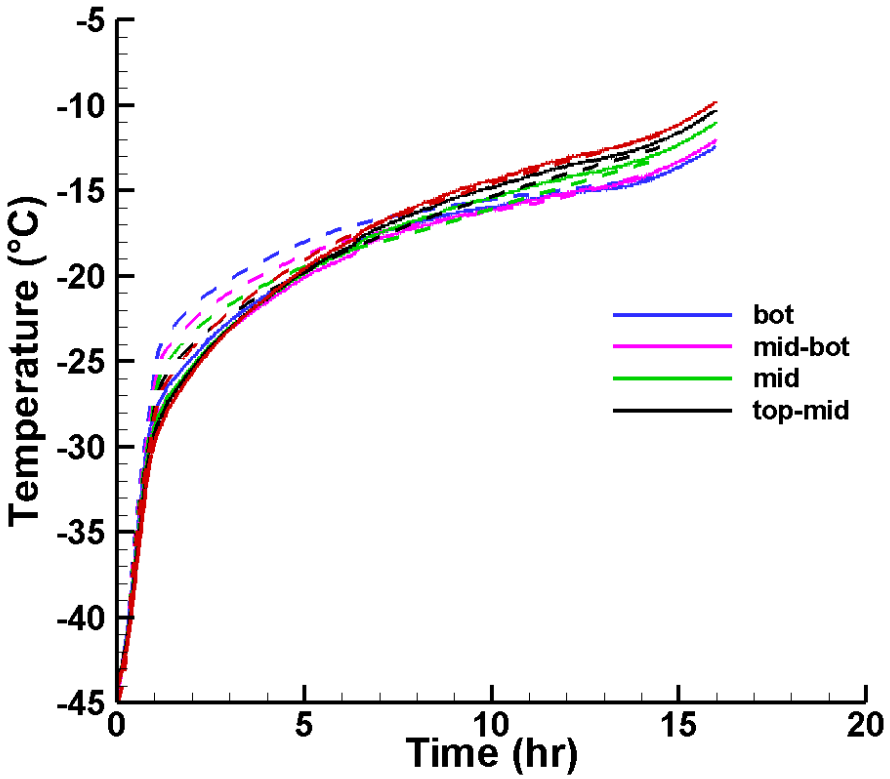

Figure 4.14. Temperature time history profiles measured by sensors (solid) vs simulation data (dashed) for vial #7.

Figure 4.16 shows the mass transfer resistance calculated from the current simulation vs obtained empirically by Pikal et al. [91] as a function of the dried thickness or cake thickness L_{ck} as:

$$R_p = A_0 + \frac{A_1 \times L_{ck}}{1 + A_2 \times L_{ck}} \tag{4.5}$$

where $A_0 = 1.4$, $A_1 = 16$, $A_2 = 0$.

The cake resistance from the current simulation is calculated according to [92]:

$$R_p = \frac{A_p \times (P_{sub} - P_{ch})}{\dot{m}_{\text{ice}}} \tag{4.6}$$

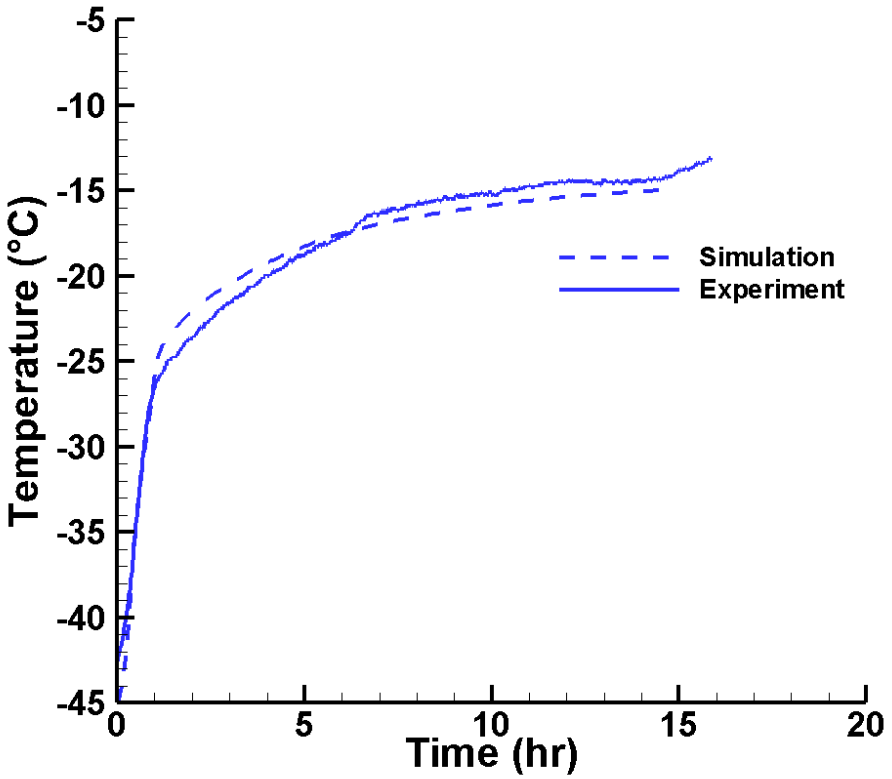

Figure 4.15. Temperature time history measured by thermocouple (solid) vs simulation data (dashed) for vial # 7

where A_p is a product area in , P_{sub} and P_{ch} are sublimation front and chamber pressures, $\dot{m}_{\text{ice}}$ is sublimation rate. R_p is a measure of vapor flow impedance resulting from dried layer structure. During the primary drying process, the dried layer thickness increases thus changing R_p. It is worth noting that in the current multiphysics simulation, the product permeability is the only parameter analogous to R_p which does not depend on cake length.

Given the ability to measure the product temperature of a center vial during primary drying, virtual thermocouple was utilized to investigate the effects of wire thermocouple heating. Figure 4.6(c) shows the experimental setup, 3 vials equipped with virtual thermocouple were placed at the center of a full tray (green dots in figure 4.6(c)), surrounding a vial equipped with both virtual temperature as well as wire TC (placed inside of the vial). This effect is demonstrated in Figure 4.17. The temperature at the walls of four vials in

Table 4.2. Fixed Simulation Parameters.

Parameter	**Dimension**	**Value**
Ice Heat Capacity	$J/Kg/K$	1967.8
Product Heat Capacity	$J/kg/K$	1715
Vapor Heat Capacity	$J/kg/K$	1674.7
Latent Heat of Sublimation	J/kg	2.7912e6
Ice Thermal Conductivity	$W/m/K$	2.1
Product Thermal Conductivity	$W/m/K$	0.028
Vapor Thermal Conductivity	$W/m/K$	0.025
Vapor Molar Mass	g/mol	18
Vapor Viscosity	$Pa \times s$	Equation 4.4
Ice density	kg/m^3	913
Product density	kg/m^3	75
Silica Glass Heat Capacity	$J/kg/K$	830
Silica Glass Density	kg/m^3	223
Silica Glass Thermal Conductivity	$W/m/K$	1.14

Table 4.3. Process Simulation Parameters.

Parameter	**Dimension**	**Value**
Air Temperature	K	Exp.
Initial Temperature	K	228
Shelf Temperature	K	Exp.
Chamber Pressure	$mTorr$	70

the center of the shelf was measured using the flexible sensors. For each of the vials, the simulation was performed and heat transfer coefficients were adjusted, so that the best agreement between sensor readings and experimental sensor data is achieved. From Figure 4.17, it can be seen that a good agreement between the vial 10 thermocouple measurement and simulation is obtained. For other vials, the heat transfer coefficient was reduced to get the experiment/simulation agreement. Thus, the plot shows that the difference between the actual product temperature and the one registered by thermocouple can be up to 2^o and is caused by the presence of the thermocouple in a vial. This result suggests in contrast of the wire thermocouple, the use of virtual thermocouple greatly reduced the risk of measure-

Table 4.4. Tuned Simulation Parameters.

Parameter	**Dimension**	**Value**
Product permeability	m^2	$1.4e-10$
Vial bottom heat transfer coefficient (in/out)	$W/m^2/K$	8/11
Porosity	–	95%

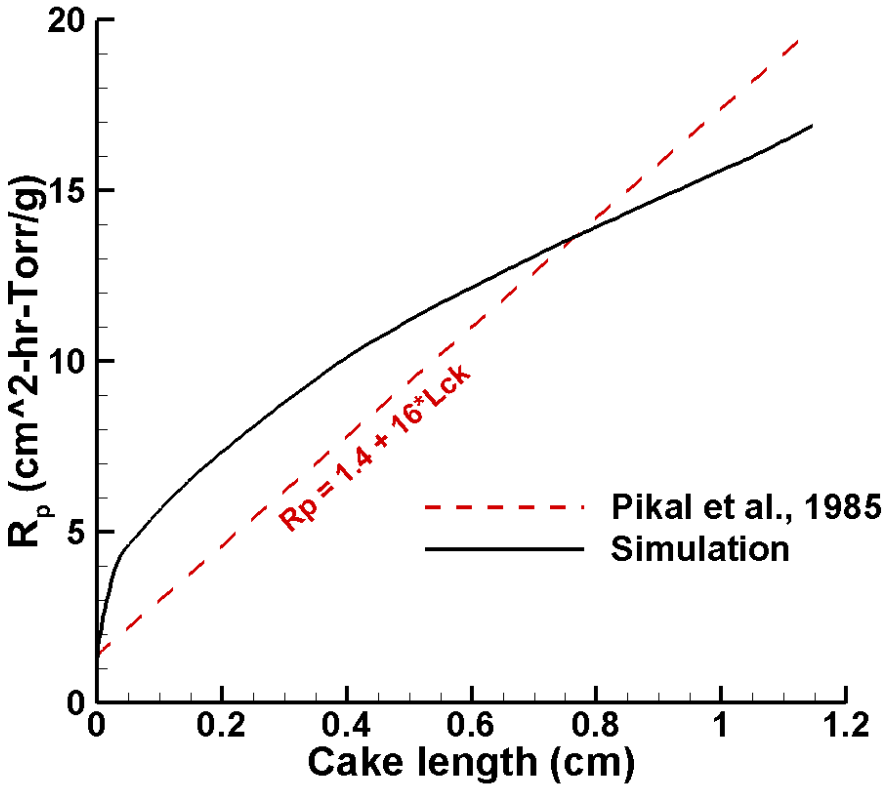

Figure 4.16. Product resistance of Mannitol 5%.

ment errors and able to measures product temperature more accurately during freeze drying process.

4.4 Conclusion

The development of optimal lyophilization procedures for different formulations in vials includes a combination of experimental tests and computational approaches for measuring

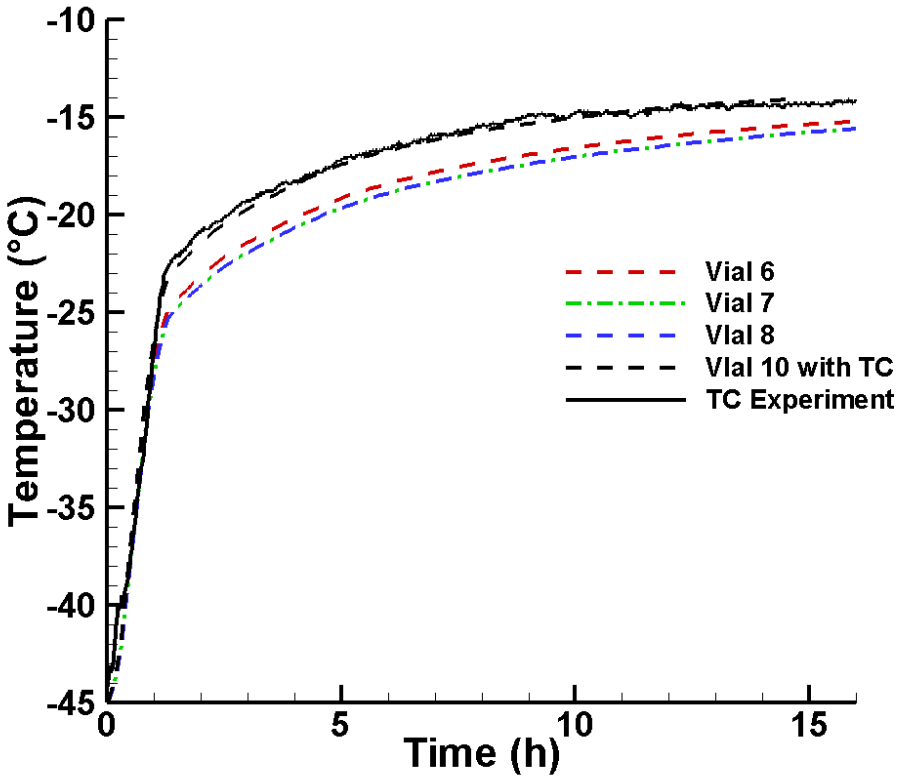

Figure 4.17. Product temperature simulation for vials without thermocouple (6,7,8), vial with thermocouple (10) and thermocouple experimental data.

product temperature. Tight temperature control is essential in both the freezing and primary drying stage because the structure of the dried product (cake) is highly determined by the freezing protocol. In particular, to obtain a good uniformity of the properties of the entire batch. Nucleation of ice and the freezing stage must be completed in a small temperature interval. It is also critical to control the temperature and the drying time during primary drying stage, when it is necessary to avoid the collapse of the product. Even though sometimes freeze-drying is considered a "mild" process, the collapse temperature of some typical pharmaceutical products can be relatively low. Also, as the residual moisture content typically affects the product negatively, the product temperature may be very low during primary drying because, even after the ice sublimation, significant amounts of bound water can be present in the product. Furthermore, heat is required during the process because the subli-

mation is endothermic, therefore the shelf temperature has to be optimized to maximize the drying speed and reduce the process time. Generally speaking, as a manipulated variable, the shelf temperature is selected based on industrial standards. The control systems are used to track the temperature of the heat transfer fluid, passing internally through the shelves, based on the pre-set recipe data. However, the heat transfer control obtained by control and manipulation of the shelf temperature is quite slow, partly because of the high thermal inertia of the system, and shelf cooling and heating may results a huge delay in terms of the response of the product temperature. Alternatively, the chamber pressure of the dryer can be controlled and manipulated. This is a very responsive way to control the drying process because the heat flux from shelf to product strongly depends on chamber pressure. However, this approach can be quite risky, because the product temperature practically follows the pressure variations, therefore a few pascals change in pressure could risk the product quality.

Since the critical part of any lyophilization procedure is the primary drying stage, special attention has to be devoted to critical modeling parameters of drying of a porous cake-solid ice system. In this work, a new technology, virtual thermocouple, based on the use of flexible multi-point temperature sensor and advanced multi-physics simulation was proposed and investigated as a means for the monitoring of freezing and drying behavior and product temperature during freeze-drying. The developed virtual thermocouple combining the one-dimensional model with surface sublimation sub-model can be used as a stand-alone, fast and accurate computational tool for the prediction of lyophilization dynamics, but can also be included into a general 3D CFD computational framework as a vital part of the final virtual lyophilizer model. The proposed virtual thermocouple was also found to give quantitative accurate results for drying behavior. In particular, the flexible multi-point sensing probe can give information about both the temperature profile and the position of the sublimating interface, this information then combined with the advanced multi-physics simulation provides the actual product temperature and shows a great matching with thermocouple measurement. For the first time, the ability to non-invasively monitoring product temperature of individual vials during primary drying was demonstrated. This proves that the proposed virtual thermocouple technology can effectively track the profile of temperature within the volume of the solution of an individual vial during the freeze-drying process.

5. SUMMARY

5.1 Dissertation Summary

This dissertation addresses the development of IoT WSNs for two challenging areas, namely smart agriculture and industrial lyophilization. For smart agriculture, a new LoRa-based hybrid low-power wide-area mesh network is proposed (Chapter 2). This hybrid network structure addresses the development of large-scale WSN that is suitable for distinct application areas with real-world deployments. To enable the data collection with varying sensors as well as to support wide-area coverage with low energy consumption, a novel IoT sensing platform was designed and manufactured integrating a micro-controller, wireless communication interfaces, and a hybrid network with short (2.4 GHz) and long-range (915 MHz) communication links. On the industrial lyophilization side, two novel low-power sensing systems were proposed for tracking the lyophilization process. A fully wireless, multi-point temperature sensor system as a Process Analytical Technology (PAT) for lyophilization is proposed (chapter 3). In addition, a new non-invasive approach, namely virtual thermocouple, that enables non-invasive measurement of the product temperature by combining flexible multi-point temperature sensing probe as well as the multi-physics simulation is proposed in chapter 4.

5.2 Contributions

The specific contributions of this dissertation are as follows.

Chapter 2: In this chapter, the design of a hybrid LPWAN mesh network for IoT application that delivers several-kilometers with only low-power nodes while provides excellent QoS was presented. This novel network structure addresses the development of large-scale WSN that is suitable for distinct application areas with real-world deployments. To enable the data collection with varying sensors as well as to support wide-area coverage with low energy consumption, a new sensing platform integrating a micro-controller, wireless communication interfaces, and a hybrid network with short (2.4 GHz) and long-range (915 MHz) communication links was designed and manufactured. With the proposed hybrid mesh network, significant improvements in both power consumption as well as communication range while

comparing with traditional single-hop networks like LoRaWAN were shown. In addition, full-scale real-world experiments on both Purdue campus and agricultural farms with more than 20 nodes further suggested that the proposed network significantly improves the quality of service while maintaining long-term stability. Several areas of future work motivated by the design and experiments on these large-scale IoT testbeds, including sophisticated anomaly detection, on-device computation, and network synchronization were provided.

Chapter 3: This chapter proposes a fully wireless, multi-point temperature sensing system for monitoring the lyophilization process. The measured profile of product temperatures using the new multi-point wireless sensor during freeze-drying of mannitol and sucrose solutions showed excellent agreement with thermocouple as well as the simulated data. The sublimation progress during primary drying was clearly tracked by the multipoint wireless sensor. The sublimation rate extracted from the wireless multi-point sensors' measurement also showed a good match with the actual gravimetric measurements. Furthermore, the vial heat transfer coefficient (Kv) calculated from the measured sublimation rate by the multi-point wireless sensor was in excellent agreement with the actual gravimetrically measured vial heat transfer coefficient. In addition, the ability of multi-point sensing endows the wireless sensor with a more elaborate characterization of the freeze-drying profile as demonstrated through the end−point detection and the sublimation front tracking. These results suggested the wireless multi-point temperature sensor system has a potential for real-time monitoring, process verification, and cycle optimization for pharmaceutical lyophilization in laboratory process development and GMP production.

Chapter 4: This chapter presents the design and implementation of virtual thermocouple, a non-invasive temperature measurement approach for controlled lyophilization. Three parts of this new technology were presented: 1)the flexible non-invasive multi-point sensing probe that is attached to the vials externally, the low-power wireless electronics that read and transmit the data wirelessly, and the numerical model that translate the temperature profile measured from the vial wall to the product temperature. In addition, experimental results are provided to show that the proposed methods can effectively be used for monitoring the drying dynamics and product temperature during the freeze-drying process in real-time and non-invasively. Due to the limitation on the computational cost, only a one-dimension model

(axisymmetrical) was used in this work. Although using 1-D axisymmetrical greatly reduces the computational cost of the multi-physics simulation and the complexity of the tuning process. It limits the use of virtual thermocouple to only center vials. Future works will focus on the 3-D simulation model that includes the non-uniform horizontal heat flow, which is necessary when expanding the use of virtual thermocouple to edge vials where the current 1-D model won't suffice due to high radiation heats on the edge vials.

REFERENCES

[1] K. Schwab, *The fourth industrial revolution*. Currency, 2017.

[2] (Feb. 2017). "M2m and iot redefined through cost effective and energy optimized connectivity.," SIGFOX One Network A Billion Dreams, [Online]. Available: https://www.sigfox.com/sites/default/files/1701-SIGFOX-White%5C_Paper%5C_Security.pdf.

[3] L. Alliance. (). "What is lorawan specification," [Online]. Available: https://lora-alliance.org/about-lorawan.

[4] *Lte evolution for iot connectivity*, White Paper, Nokia, Nov. 2016. [Online]. Available: https://www.open-ecosystem.org/assets/lte-evolution-iot-connectivity.

[5] X. Jiang, H. Zhang, E. A. B. Yi, N. Raghunathan, C. Mousoulis, S. Chaterji, D. Peroulis, A. Shakouri, and S. Bagchi, "Hybrid low-power wide-area mesh network for iot applications," *IEEE Internet of Things Journal*, 2020.

[6] S. Chaterji, N. DeLay, J. Evans, N. Mosier, B. Engel, D. Buckmaster, and R. Chandra, "Artificial intelligence for digital agriculture at scale: Techniques, policies, and challenges," *arXiv preprint arXiv:2001.09786*, 2020.

[7] G. Satyanarayana and S. Mazaruddin, "Wireless sensor based remote monitoring system for agriculture using zigbee and gps," 2013.

[8] C. Akshay, N. Karnwal, K. Abhfeeth, R. Khandelwal, T. Govindraju, D. Ezhilarasi, and Y. Sujan, "Wireless sensing and control for precision green house management," in *Sensing Technology (ICST), 2012 Sixth International Conference on*, IEEE, 2012, pp. 52–56.

[9] N. Kaewmard and S. Saiyod, "Sensor data collection and irrigation control on vegetable crop using smart phone and wireless sensor networks for smart farm," in *Wireless Sensors (ICWiSE), 2014 IEEE Conference on*, IEEE, 2014, pp. 106–112.

[10] X. Jiang and H. Zhang. (Apr. 2020). "Technical report," [Online]. Available: $https://lladzhang.github.io/heng.github.io/Technical_report.pdf$.

[11] K. Mikhaylov, J. Petaejaejaervi, and T. Haenninen, "Analysis of capacity and scalability of the lora low power wide area network technology," in *European Wireless 2016; 22th European Wireless Conference*, VDE, 2016, pp. 1–6.

[12] (Jul. 2007). "Ant message protocol and usage," Dynastream Innovations Inc., [Online]. Available: https://www.sparkfun.com/datasheets/Wireless/Nordic/ANT-UserGuide.pdf.

[13] S. Khssibi, H. Idoudi, A. Van den Bossche, T. Val, and L. A. Saidane, "Presentation and analysis of a new technology for low-power wireless sensor network," *International Journal of Digital Information and Wireless Communications*, vol. 3, no. 1, pp–75, 2013.

[14] (2018). "Zigbee," [Online]. Available: https://www.zigbee.org/.

[15] A. J. Wixted, P. Kinnaird, H. Larijani, A. Tait, A. Ahmadinia, and N. Strachan, "Evaluation of lora and lorawan for wireless sensor networks," in *2016 IEEE SENSORS*, IEEE, 2016, pp. 1–3.

[16] cooking hacks, "Extreme range links: Lora 868 / 900mhz sx1272 lora module for arduino waspmote and raspberry pi,"

[17] K. Ahmavaara, H. Haverinen, and R. Pichna, "Interworking architecture between 3gpp and wlan systems," *IEEE Communications Magazine*, vol. 41, no. 11, pp. 74–81, 2003.

[18] K. Mekki, E. Bajic, F. Chaxel, and F. Meyer, "A comparative study of lpwan technologies for large-scale iot deployment," *ICT express*, vol. 5, no. 1, pp. 1–7, 2019.

[19] O. Khutsoane, B. Isong, and A. M. Abu-Mahfouz, "Iot devices and applications based on lora/lorawan," in *IECON 2017-43rd Annual Conference of the IEEE Industrial Electronics Society*, IEEE, 2017, pp. 6107–6112.

[20] T. Bouguera, J.-F. Diouris, J.-J. Chaillout, R. Jaouadi, and G. Andrieux, "Energy consumption model for sensor nodes based on lora and lorawan," *Sensors*, vol. 18, no. 7, p. 2104, 2018.

[21] *SX1261/2 Long Range, Low Power, sub-GHz RF Transceiver data sheet*, Camarillo, CA, USA: Semtech.

[22] D. Zorbas, K. Abdelfadeel, P. Kotzanikolaou, and D. Pesch, "Ts-lora: Time-slotted lorawan for the industrial internet of things," *Computer Communications*, vol. 153, pp. 1–10, 2020.

[23] F. Adelantado, X. Vilajosana, P. Tuset-Peiro, B. Martinez, J. Melia-Segui, and T. Watteyne, "Understanding the limits of lorawan," *IEEE Communications magazine*, vol. 55, no. 9, pp. 34–40, 2017.

[24] N. Varsier and J. Schwoerer, "Capacity limits of lorawan technology for smart metering applications," in *2017 IEEE International Conference on Communications (ICC)*, IEEE, 2017, pp. 1–6.

[25] R. Piyare, A. L. Murphy, M. Magno, and L. Benini, "On-demand tdma for energy efficient data collection with lora and wake-up receiver," in *2018 14th International Conference on Wireless and Mobile Computing, Networking and Communications (WiMob)*, IEEE, 2018, pp. 1–4.

[26] B. Reynders, Q. Wang, P. Tuset-Peiro, X. Vilajosana, and S. Pollin, "Improving reliability and scalability of lorawans through lightweight scheduling," *IEEE Internet of Things Journal*, vol. 5, no. 3, pp. 1830–1842, 2018.

[27] C.-H. Liao, G. Zhu, D. Kuwabara, M. Suzuki, and H. Morikawa, "Multi-hop lora networks enabled by concurrent transmission," *IEEE Access*, vol. 5, pp. 21 430–21 446, 2017.

[28] C. Ebi, F. Schaltegger, A. Rüst, and F. Blumensaat, "Synchronous lora mesh network to monitor processes in underground infrastructure," *IEEE access*, 2019.

[29] N. A. Pantazis, D. J. Vergados, D. D. Vergados, and C. Douligeris, "Energy efficiency in wireless sensor networks using sleep mode tdma scheduling," *Ad Hoc Networks*, vol. 7, no. 2, pp. 322–343, 2009.

[30] C. L. Hedrick, "Routing information protocol," 1988.

[31] M. N. Ochoa, A. Guizar, M. Maman, and A. Duda, "Evaluating lora energy efficiency for adaptive networks: From star to mesh topologies," in *2017 IEEE 13th International Conference on Wireless and Mobile Computing, Networking and Communications (WiMob)*, IEEE, 2017, pp. 1–8.

[32] X. Jiang, J. F. Waimin, H. Jiang, C. Mousoulis, N. Raghunathan, R. Rahimi, and D. Peroulis, "Wireless sensor network utilizing flexible nitrate sensors for smart farming," in *2019 IEEE SENSORS*, IEEE, 2019, pp. 1–4.

[33] (2019). "Huwomoibilty," [Online]. Available: http://www.huwomo.com/.

[34] (2019). "Nrf52832," [Online]. Available: https://www.nordicsemi.com/Products/Low-power-short-range-wireless/nRF52832.

[35] (2018). "Semtech," [Online]. Available: https://www.semtech.com/products/wireless-rf/lora-transceivers.

[36] L. Alliance, "A technical overview of lora and lorawan," *White Paper*, 2015.

[37] (2019). "Nrf52832," [Online]. Available: https://www.keysight.com/en/pd-1842303-pn-N6705B/dc-power-analyzer-modular-600-w-4-slots.

[38] (2019). "Meter group ech2o 5te soil moisture sensor," [Online]. Available: https://metos.at/portfolio/decagon-5te-soil-moisture-sensor/.

[39] (2019). "Semtech sx1272dvk1cas development kit, sx1272, 915 mhz," [Online]. Available: https://www.semtech.com/products/wireless-rf/lora-transceivers/sx1272dvk1cas.

[40] N. S. Almakhdhub, A. A. Clements, M. Payer, and S. Bagchi, "Benchiot: A security benchmark for the internet of things," in *2019 49th Annual IEEE/IFIP International Conference on Dependable Systems and Networks (DSN)*, IEEE, 2019, pp. 234–246.

[41] A. A. Clements, N. S. Almakhdhub, S. Bagchi, and M. Payer, "ACES: Automatic compartments for embedded systems," in *27th {USENIX} Security Symposium (USENIX Security 18)*, 2018, pp. 65–82.

[42] J. Corver, P.-J. V. Bockstal, and T. D. Beer, "A continuous and controlled pharmaceutical freeze-drying technology for unit doses," in *AIChE Annual Meeting*, 2017.

[43] T. A. Jennings, *Lyophilization: introduction and basic principles*. CRC press, 1999.

[44] F. Franks and T. Auffret, *Freeze-drying of Pharmaceuticals and Biopharmaceuticals*. royal Society of Chemistry, 2008.

[45] D. Fissore, R. Pisano, and A. A. Barresi, "On the use of temperature measurement to monitor a freeze-drying process for pharmaceuticals," in *2017 IEEE International Instrumentation and Measurement Technology Conference (I2MTC)*, IEEE, 2017, pp. 1–6.

[46] R. J. Bellows and C. J. King, "Freeze-drying of aqueous solutions: Maximum allowable operating temperature," *Cryobiology*, vol. 9, no. 6, pp. 559–561, 1972.

[47] S. Tsourouflis, J. M. Flink, and M. Karel, "Loss of structure in freeze-dried carbohydrates solutions: Effect of temperature, moisture content and composition," *Journal of the Science of Food and Agriculture*, vol. 27, no. 6, pp. 509–519, 1976.

[48] S. Schneid and H. Gieseler, "Evaluation of a new wireless temperature remote interrogation system (tempris) to measure product temperature during freeze drying," *Aaps Pharmscitech*, vol. 9, no. 3, pp. 729–739, 2008.

[49] S. Schneid and H. Gieseler, "Evaluation of a new wireless temperature remote interrogation system (tempris) to measure product temperature during freeze drying," *Aaps Pharmscitech*, vol. 9, no. 3, pp. 729–739, 2008.

[50] *Tempris Sensor technology*, iQ-mobil Solutions. [Online]. Available: http://www.tempris.com/products/.

[51] *WTMplus Wireless Temperature Measurement*, Martin Christ. [Online]. Available: http://www.martinchrist.de/fileadmin/user$%5C_$upload/christ/%2002$%5C_$produkte/02$%5C_$pilot/%20optionen/%20wtm/%20Christ-WTMplus-Folder-Web.pdf.

[52] *ellab TrackSense Pro*, ellab Validation Solutions. [Online]. Available: http://www.ellab.com/products/find-the-right-data-logger/tracksense-pro.

[53] *Vaccine Temperature Monitoring System (VTMS) Data Logger*, MadgeTech. [Online]. Available: http://www.madgetech.com/data-loggers/applications/vaccine-monitoring-data-loggers/vtms.html.

[54] *Wireless Data Loggin System*, T and D Corporation. [Online]. Available: http://www.tandd.com/product/rtr500x/index.html.

[55] X. Jiang, T. Zhu, T. Kodama, N. Raghunathan, A. Alexeenko, and D. Peroulis, "Multi-point wireless temperature sensing system for monitoring pharmaceutical lyophilization," *Frontiers in chemistry*, vol. 6, p. 288, 2018.

[56] R. E. Johnson, C. F. Kirchhoff, and H. T. Gaud, "Mannitol–sucrose mixturesâ€"versatile formulations for protein lyophilization," *Journal of pharmaceutical sciences*, vol. 91, no. 4, pp. 914–922, 2002.

[57] N. Raghunathan, X. Jiang, D. Peroulis, and A. Ganguly, "Wireless low-power temperature probes for food/pharmaceutical process monitoring," in *SENSORS, 2015 IEEE*, Nov. 2015, pp. 1–4. DOI: 10.1109/ICSENS.2015.7370356.

[58] N. Raghunathan, X. Jiang, A. Ganguly, and D. Peroulis, "An ant-based low-power battery-free wireless cryogenic temperature probes for industrial process monitoring," in *2016 IEEE SENSORS*, Oct. 2016, pp. 1–3. DOI: 10.1109/ICSENS.2016.7808751.

[59] *GRM Series General Purpose Monolithic Ceramic Capacitors*, Murata, Inc. [Online]. Available: http://psearch.murata.com/capacitor/lineup/grm/$%5C#$a01.

[60] *PCap01 Capacitance-to-Digital Converter with integrated Signal Processor*, ACAM messelectronic, gmbh. [Online]. Available: http://www.acam.de/products/picocap/pcap01/.

[61] *SUPER SHIELDâ„¢ NICKEL CONDUCTIVE COATING*, MG Chemicals. [Online]. Available: http://www.mgchemicals.com/products/emi-and-rfi-shielding/other-coating-systems/super-shield-nickel-841.

[62] *nRF52832 ANT multiprotocol SoC*, Nordic Semiconductor, Inc. [Online]. Available: https://www.nordicsemi.com/eng/Products/Bluetooth-low-energy/nRF52832.

[63] Powercast®, "915 MHz RF Powerharvester® receiver," 2018. [Online]. Available: http://www.powercastco.com/wp-content/uploads/2016/12/P2110B-Datasheet-Rev-3.pdf.

[64] *GA209F Supercapacitor*, CAPXX Supercapacitor. [Online]. Available: https://www.tecategroup.com/store/index.php?main_page=product_info&products_id=1269.

[65] M. Technology. (). "Revo research and development freeze dryer," [Online]. Available: https://www.millrocktech.com/freeze-dryers-2/revo-research-development-freeze-dryer/. (accessed: 01.09.2019).

[66] G. Schelenz, J. Engel, and H. Rupprecht, "Sublimation during lyophilization detected by temperature profile and x-ray technique," *International Journal of Pharmaceutics*, vol. 113, no. 2, pp. 133–140, 1995.

[67] J. Barley, *Basic Principles of Freeze Drying*. SP Scientific, 2009.

[68] A. V. Wouwer, P. Saucez, C. Vilas, *et al.*, "Simulation of ode/pde models with matlab, octave and scilab," *Cham: Springer*, 2014.

[69] W. Mascarenhas, H. Akay, and M. Pikal, "A computational model for finite element analysis of the freeze-drying process," *Computer methods in applied mechanics and engineering*, vol. 148, no. 1-2, pp. 105–124, 1997.

[70] V. R. Koganti, E. Y. Shalaev, M. R. Berry, T. Osterberg, M. Youssef, D. N. Hiebert, F. A. Kanka, M. Nolan, R. Barrett, G. Scalzo, *et al.*, "Investigation of design space for freeze-drying: Use of modeling for primary drying segment of a freeze-drying cycle," *AAPS PharmSciTech*, vol. 12, no. 3, pp. 854–861, 2011.

[71] M. Pikal, M. Roy, and S. Shah, "Mass and heat transfer in vial freeze-drying of pharmaceuticals: Role of the vial," *Journal of pharmaceutical sciences*, vol. 73, no. 9, pp. 1224–1237, 1984.

[72] R. Pisano, D. Fissore, and A. A. Barresi, "Heat Transfer in Freeze-Drying Apparatus," en, 2011. DOI: 10.5772/23799. [Online]. Available: http://www.intechopen.com/books/developments-in-heat-transfer/heat-transfer-in-freeze-drying-apparatus (visited on 03/16/2017).

[73] H. Gieseler, W. J. Kessler, M. Finson, S. J. Davis, P. A. Mulhall, V. Bons, D. J. Debo, and M. J. Pikal, "Evaluation of tunable diode laser absorption spectroscopy for in-process water vapor mass flux measurements during freeze drying," *Journal*

of pharmaceutical sciences, vol. 96, no. 7, pp. 1776–1793, 2007. [Online]. Available: http://onlinelibrary.wiley.com/doi/10.1002/jps.20827/full (visited on 10/16/2016).

[74] M. Pikal, "Use of laboratory data in freeze drying process design: Heat and mass transfer coefficients and the computer simulation of freeze drying," *PDA Journal of Pharmaceutical Science and Technology*, vol. 39, no. 3, pp. 115–139, 1985.

[75] M. Pikal, S. Shah, D. Senior, and J. Lang, "Physical chemistry of freeze-drying: Measurement of sublimation rates for frozen aqueous solutions by a microbalance technique," *Journal of pharmaceutical sciences*, vol. 72, no. 6, pp. 635–650, 1983.

[76] S. Nail, S. Tchessalov, E. Shalaev, A. Ganguly, E. Renzi, F. Dimarco, L. Wegiel, S. Ferris, W. Kessler, M. Pikal, *et al.*, "Recommended best practices for process monitoring instrumentation in pharmaceutical freeze drying—2017," *Aaps Pharmscitech*, vol. 18, no. 7, pp. 2379–2393, 2017.

[77] I. Oddone, D. Fulginiti, A. A. Barresi, S. Grassini, and R. Pisano, "Non-invasive temperature monitoring in freeze drying: Control of freezing as a case study," *Drying Technology*, vol. 33, no. 13, pp. 1621–1630, 2015.

[78] J. Ravnik, I. Golobič, A. Sitar, M. Avanzo, Š. Irman, K. Kočevar, M. Cegnar, M. Zadravec, M. Ramšak, and M. Hriberšek, "Lyophilization model of mannitol water solution in a laboratory scale lyophilizer," *Journal of Drug Delivery Science and Technology*, vol. 45, pp. 28–38, 2018.

[79] M. Parvis, S. Grassini, D. Fulginiti, R. Pisano, and A. A. Barresi, "Sputtered thermocouple array for vial temperature mapping," in *2014 IEEE International Instrumentation and Measurement Technology Conference (I2MTC) Proceedings*, IEEE, 2014, pp. 1465–1470.

[80] N. Raghunathan, X. Jiang, D. Peroulis, and A. Ganguly, "Wireless low-power temperature probes for food/pharmaceutical process monitoring," in *2015 IEEE SENSORS*, IEEE, 2015, pp. 1–4.

[81] N. Raghunathan, X. Jiang, A. Ganguly, and D. Peroulis, "An ant-based low-power battery-free wireless cryogenic temperature probes for industrial process monitoring," in *2016 IEEE SENSORS*, IEEE, 2016, pp. 1–3.

[82] *P2110B 915 MHz RF Powerharvester Receiver*, Powercast Co. [Online]. Available: http://www.powercastco.com/test566alpha/wp-content/uploads/2009/03/p2110b-datasheet-v12.pdf.

[83] *Freeze Drying*, COMSOL Inc. [Online]. Available: https://www.comsol.com/model/download/704571/freeze_drying.pdf.

[84] H. Gieseler, T. Kramer, and M. J. Pikal, "Use of manometric temperature measurement (mtm) and smart™ freeze dryer technology for development of an optimized freeze-drying cycle," *Journal of Pharmaceutical Sciences*, vol. 96, no. 12, pp. 3402–3418, 2007.

[85] A. A. Alexeenko, A. Ganguly, and S. L. Nail, "Computational analysis of fluid dynamics in pharmaceutical freeze-drying," *Journal of pharmaceutical sciences*, vol. 98, no. 9, pp. 3483–3494, 2009.

[86] C. Smith, "An experimental study of the viscous properties of water vapour," *Proceedings of the Royal Society of London. Series A, Containing Papers of a Mathematical and Physical Character*, vol. 106, no. 735, pp. 83–96, 1924.

[87] V. Teske, E. Vogel, and E. Bich, "Viscosity measurements on water vapor and their evaluation," *Journal of Chemical & Engineering Data*, vol. 50, no. 6, pp. 2082–2087, 2005.

[88] I. Yasumoto, "Viccosity of water vapor in the temperature range from 6° c to 29° c," *Bulletin of the Chemical Society of Japan*, vol. 43, no. 12, pp. 3917–3919, 1970.

[89] H. Braune and R. Linke, "Uber die innere reibung einiger gase und dampfe," *Phys Chem*, vol. 148, p. 195, 1930.

[90] J. Cooper and R. Dooley, "International association for the properties of water and steam: Release on the iapws formulation 2008 for the viscosity of ordinary water substance," *IAPWS Release, IAPWS Secretariat*, 2008.

[91] M. Pikal, "Use of laboratory data in freeze drying process design: Heat and mass transfer coefficients and the computer simulation of freeze drying," *PDA Journal of Pharmaceutical Science and Technology*, vol. 39, no. 3, pp. 115–139, 1985.

[92] M. J. Pikal, M. Roy, and S. Shah, "Mass and heat transfer in vial freeze-drying of pharmaceuticals: Role of the vial," *Journal of pharmaceutical sciences*, vol. 73, no. 9, pp. 1224–1237, 1984.

VITA

Xiaofan Jiang was born in Qingdao, China. He received his Bachelor degree in Electrical and Computer Engineering (ECE) from Purdue University (West Lafayette, Indiana, USA) in 2015. Shortly afterward, he started his PhD degree at the school of Electrical and Computer Engineering, Purdue University and joined the Adaptive Radio Electronics and Sensors (ARES) group led by Prof. Dimitrios Peroulis. His research interests include design and implementation of various embedded systems, wireless sensor networks, and IoT devices for general and industrial applications.